

ABSTRACT

LOWMAN, NICHOLAS K. Viscous Fluid Conduits as a Prototypical Nonlinear Dispersive Wave Platform. (Under the direction of Mark Hoefer.)

This thesis is devoted to the comprehensive characterization of slowly modulated, nonlinear waves in dispersive media for physically-relevant systems using a threefold approach: analytical, long-time asymptotics, careful numerical simulations, and quantitative laboratory experiments. In particular, we use this interdisciplinary approach to establish a two-fluid, interfacial fluid flow setting known as viscous fluid conduits as an ideal platform for the experimental study of truly one dimensional, unidirectional solitary waves and dispersively regularized shock waves (DSWs). Starting from the full set of fluid equations for mass and linear momentum conservation, we use a multiple-scales, perturbation approach to derive a scalar, nonlinear, dispersive wave equation for the leading order interfacial dynamics of the system. Using a generalized form of the approximate model equation, we use numerical simulations and an analytical, nonlinear wave averaging technique, Whitham-El modulation theory, to derive the key physical features of interacting large amplitude solitary waves and DSWs. We then present the results of quantitative, experimental investigations into large amplitude solitary wave interactions and DSWs. Overtaking interactions of large amplitude solitary waves are shown to exhibit nearly elastic collisions and universal interaction geometries according to the Lax categories for KdV solitons, and to be in excellent agreement with the dynamics described by the approximate asymptotic model. The dispersive shock wave experiments presented here represent the most extensive comparison to date between theory and data of the key wavetrain parameters predicted by modulation theory. We observe strong agreement. Based on the work in this thesis, viscous fluid conduits provide a well-understood, controlled, table-top environment in which to study universal properties of dispersive hydrodynamics.

Motivated by the study of wave propagation in the conduit system, we identify four new admissibility criteria required for proper application of the Whitham-El DSW closure method for

a general class of scalar dispersive hydrodynamic equations. Further, we explore regularization distinguishing characteristics of dissipative versus dispersive smoothing in a bidirectional system, Fermi gas at unitarity, in which the appropriate physical mechanism is unclear. It is shown that key differences in the resolution of nonlinear wave breaking allow one to design regularization determining experiments.

© Copyright 2014 by Nicholas K. Lowman

All Rights Reserved

Viscous Fluid Conduits as a Prototypical
Nonlinear Dispersive Wave Platform

by
Nicholas K. Lowman

A dissertation submitted to the Graduate Faculty of
North Carolina State University
in partial fulfillment of the
requirements for the Degree of
Doctor of Philosophy

Applied Mathematics

Raleigh, North Carolina

2014

APPROVED BY:

Karen Daniels

Gennady El

Zhilin Li

Michael Shearer

Mark Hoefer
Chair of Advisory Committee

DEDICATION

To my wife and family for their love and unwavering support.

BIOGRAPHY

Nicholas Lowman was born September 14, 1987 in Winston-Salem, NC. He received a B.S. in Earth and Ocean Sciences and a B.A. in Mathematics from Duke University in 2009. In May 2011, Nicholas began his graduate studies at North Carolina State University in Applied Mathematics with his Ph.D. advisor Professor Mark Hoefer.

ACKNOWLEDGEMENTS

Mark Hoefer. I thank you for all of your encouragement and support from the first day I began my applied math career. You have been a mentor and a friend.

My dissertation committee: Karen Daniels, Gennady El, Zhilin Li, and Michael Shearer. Thank you all for your participation and guidance throughout this process, and for the many fruitful conversations I have had with each of you.

Department of Mathematics, North Carolina State University. I have thoroughly enjoyed my time in the department and the friends and colleagues I have acquired in my years here.

My family. You are always by my side, no matter the endeavor.

My wife, Lauren. I am grateful to you for your patience through the good times and bad. I cannot imagine taking on graduate school without you.

This work has been supported by the National Science Foundation through the NCSU Research Training Group: Mathematics of Materials, NCSU Research Experience for Early Graduate Students, and Graduate Research Fellowship Program (DGE-1252376).

TABLE OF CONTENTS

LIST OF TABLES	viii
LIST OF FIGURES	ix
Chapter 1 Introduction	1
1.1 Nonlinear Waves and Modulation Theory	3
1.2 Experimental Studies of Nonlinear Waves	5
1.3 Viscous Fluid Conduits as 1D Superfluids	10
Chapter 2 Derivation of an Approximate Interfacial Equation	13
2.1 Abstract	13
2.2 Introduction	14
2.3 Problem Description	17
2.3.1 Governing Equations	19
2.3.2 Uniform Pipe Flow and Nondimensionalization	21
2.4 Derivation of the Approximate Model	26
2.4.1 Asymptotic Expansions and Scaling Ansatz	26
2.4.2 Leading Order Solution	28
2.4.3 Reduction to the Conduit Equation	31
2.5 Robustness of the Conduit Equation	31
2.5.1 Viscous, Higher Order Corrections	32
2.5.2 Breakdown of Assumptions	32
2.5.3 Dependence on an Outer Wall	33
2.5.4 Symmetry Breaking – Inclined Conduit	35
2.5.5 Summary	36
2.6 Discussion and Conclusions	36
Chapter 3 Dispersive Shock Waves in Viscously Deformable Media: Whitham-El Modulation Theory and Numerical Simulations	41
3.1 Abstract	42
3.2 Introduction	43
3.3 Governing Equations	47
3.3.1 Magma Geophysics	47
3.3.2 Viscous Fluid Conduits	50
3.4 Properties of the Magma Equation	52
3.4.1 Linear Dispersion Relation and Scaling	52
3.4.2 Long Wavelength Regime	53
3.4.3 Nonlinear Periodic Traveling Wave Solutions	54
3.4.4 Conservation Laws	57
3.5 Resolution of an Initial Discontinuity	58
3.5.1 Application of El’s method	60
3.5.2 Determination of the Trailing Edge Speed	62

3.5.3	Determination of the Leading Edge Speed and Amplitude	66
3.5.4	Analysis of the Theoretical Predictions	69
3.6	Comparison with Numerical Simulations	73
3.6.1	Numerical Simulations	73
3.6.2	Breakdown of Analytical Method	75
3.7	Summary and Conclusions	84
3.8	Appendix – Numerical method	85
Chapter 4 Simple Wave DSW Admissibility for Scalar Equations		90
Chapter 5 Experiments on Large Amplitude Solitary Wave Interactions in Viscous Fluid Conduits		98
5.1	Abstract	99
5.2	Introduction	99
5.3	Theoretical foundations	102
5.3.1	Derivation of the conduit equation and solitary wave solutions	104
5.3.2	Numerical methods	106
5.3.3	Experimental set-up	107
5.4	Overtaking interactions between strongly nonlinear solitary waves	108
5.4.1	Classification of interactions: KdV	109
5.4.2	Classification of interactions: conduit equation	109
5.4.3	Radiation emitted due to interaction	112
5.4.4	Experimental observation of the three types of interaction	113
5.5	Summary and conclusions	116
Chapter 6 Experiments on Dispersive Shock Waves in Viscous Fluid Conduits		118
6.1	Abstract	118
6.2	Introduction	119
6.3	Theoretical Background	122
6.4	Experimental Procedures	123
6.4.1	Laboratory Set-Up and Fluid Properties	123
6.4.2	Image Processing and Measurement Extraction	125
6.4.3	Comments on the Experimental Data	127
6.4.4	Considerations for the Bottom Boundary	127
6.4.5	Validation of Area Conservation	135
6.5	Results of DSW Experiments	136
6.6	Discussion and Conclusions	141
Chapter 7 Dispersive Shock Waves in a Bidirectional System		143
7.1	Abstract	144
7.2	Introduction	144
7.3	Governing Equations	145
7.4	Effects of Regularization	149
7.4.1	Dissipation	149

7.4.2	Dispersion	150
7.5	Regularization Determining Experiments	151
7.6	Conclusions	153
7.7	Appendix – 1D Reduction	154
Chapter 8	Conclusion	159
REFERENCES	161

LIST OF TABLES

Table 2.1	Experimental parameters used to study solitary waves on viscous fluid conduits in previous literature. The parameters listed for [83] are reported for conduit fluid B only because the authors reported issues due to mass diffusion with conduit fluid A and for a single background flux value for which good agreement between theory and experiment was reported. All quantities are in cgs units with the same number of significant digits as in the original papers.	40
Table 5.1	Key experimental parameters.	108
Table 6.1	Characteristic fluid properties of the experimental system.	125
Table 6.2	Comparison of the relative difference in area of the conduit area, as measured by two high-resolution cameras separated by approximately one vertical meter.	136
Table 6.3	Nondimensional DSW speed and amplitude data for seven experimental trials.	138

LIST OF FIGURES

Figure 1.1	Dispersive shock wave.	2
Figure 2.1	Geometry of an axisymmetric, intrusive fluid conduit occupying a domain $V^{(i)}$ flowing within a dense, exterior fluid of higher viscosity in a domain $V^{(e)}$. The dashed line denotes an unperturbed conduit of radius R_0 , and the solid line is the conduit with some disturbance. Relevant physical quantities are noted, as well as the sign conventions for the conduit unit normal vector, $\hat{\mathbf{n}}_c$, conduit unit tangent vector, $\hat{\mathbf{t}}_c$, and cross-sectional disk unit normal vector, $\hat{\mathbf{n}}_d$	18
Figure 2.2	Figure 18 from the review article [123]. A vertically uniform, intrusive conduit is established with red fluid and then perturbed by a step-like increase in the injection with green fluid. One can see the formation of a DSW, with its characteristic periodic wavetrain slowly modulated over long space and time scales. An interesting observation is that the trailing fluid becomes trapped within individual waves of the DSW, surrounded by the leading fluid.	39
Figure 3.1	Example numerical solution of the dispersive Riemann problem for eq. (3.1). The solution to the initial step connects the external constant states ϕ_{\pm} to an inner oscillatory region with a solitary wave leading edge where the wavenumber $k \rightarrow 0$ and a packet of linear waves in the trailing edge where $a \rightarrow 0$. The salient physical properties of a magma DSW are the leading edge amplitude a_+ , trailing edge wavenumber k_- , the forward propagation speed of the solitary wave front s_+ , and the trailing edge speed s_-	47
Figure 3.2	Plot of $(\phi')^2 = g(\phi)$, $(n, m) = (2, 1)$. The bounded, periodic solution lies between the roots ϕ_2 and ϕ_3 . The roots correspond to a particular choice of the physical wave parameters $a = 0.6$, $k \approx 0.29$, and $\bar{\phi} = 1$	58
Figure 3.3	Analytical predictions for the normalized speeds and amplitude of magma DSWs. In (a) and (b) the thicker curves indicate the leading edge speeds, and the thinner curves show the trailing edge speeds. Note the existence of a zero and a universal global minimum in the normalized trailing edge speeds for all cases of (n, m) . For (c) and (d), the thinner dashed line is the KdV amplitude result.	72
Figure 3.4	Two different types of envelope structures observed in simulations of eq. (3.1). (a) The numerical solution at $t = 120$ for parameter values $\phi_+ = 0.6$, $(n, m) = (3, 0)$. (b) The magma equation at $t = 200$ for parameter values $\phi_+ = 0.5$, $(n, m) = (2, 1)$	74

Figure 3.5	Comparisons for $(n, m) = (3, 0)$ and $(n, m) = (2, 1)$ of the predicted (solid lines) versus computed values (dot points) of the leading edge speeds and amplitudes for varying ϕ_+ . The dashed lines indicate the predictions from KdV theory in the weakly nonlinear regime. The vertical dotted line is the critical jump height ϕ_c , beyond which the analytical theory is no longer valid.	76
Figure 3.6	Contour plots of numerical solutions for $\phi(z, t)$ plotted in the characteristic z - t plane for different parameter values with the overlying dashed lines indicating the predicted values for the leading and trailing edge speeds. The angles (speeds) line up excellently.	77
Figure 3.7	From top to bottom, magma DSWs in the forward propagating case, the backflow regime before gradient catastrophe, and after DSW implosion. The solutions shown correspond, from top to bottom, to (a) $t_f = \{200, 150, 150\}$, (b) $t_f = \{400, 200, 200\}$	82
Figure 3.8	DSW implosion. Evolution of the solution to eq. (3.1) with $(n, m) = (2, 1)$, $\phi_+ = .1 < \phi_c \approx 0.16$. The solution initially develops into a typical DSW with one-phase interior, but as it evolves, the trailing edge compresses and longer waves from the interior overtake shorter waves near the edge. Internal wave interactions (implosion) commence and the one-phase assumption is no longer valid.	83
Figure 3.9	Contour plot of numerically computed $\phi(z, t)$ from figure 3.8 in the characteristic z - t plane exhibiting modulated one-phase and two-phase behavior.	84
Figure 3.10	Convergence plots of the ∞ -norm of the difference of the numerically evolved solitary wave versus the true solution. In both cases, the time discretization Δt is fixed and we vary Δz . The dotted lines indicate the desired sixth order convergence.	89
Figure 5.1	Diagram of the fluid conduit experimental system.	103
Figure 5.2	Example numerical solutions of the conduit equation eq. (5.5) exhibiting the three types of overtaking interactions. The initial and final states, as well as the solution at the time of peak interaction t_i , are plotted on the spatial axis while the left and right insets correspond to the solution just before and just after the peak interaction. The trailing amplitude is varied, while the leading amplitude is fixed, $a_{\text{lead}} = 1$. (a) Bimodal interaction, $a_{\text{trail}} = 3.5$. (b) Mixed interaction, $a_{\text{trail}} = 5$. (c) Unimodal interaction, $a_{\text{trail}} = 8$	110

Figure 5.3	Phase diagram of the numerical and experimental classification of the overtaking interaction between two conduit solitary waves as a function of the leading and trailing wave amplitudes. The blue (darker) curve indicates the transition from bimodal interaction to the intermediate/mixed type. The red (lighter) curve marks the transition from the mixed type to unimodal. The inset represents the boxed portion in the weakly nonlinear regime showing convergence to the KdV predictions (dashed lines). Crosses along $a_{\text{lead}} = 1$ correspond to simulations in Fig. 5.2. The geometric shapes correspond to experimental classification.	114
Figure 5.4	Data from interaction experiments. (a) Unscaled data showing the solitary wave profiles from a typical interaction. (b) Examples of the three interaction types for scaled data used in classifications. From top to bottom, $(a_{\text{lead}}, a_{\text{trail}})$ are (1.27, 3.45), (1.53, 9.97), and (1.14, 10.01), respectively. See the online version of the paper for movies of these experiments.	115
Figure 6.1	Comparison of observed conduit diameter plotted against the log of the injection rate. The blue line is the result of a nonlinear least squares fit to the experimental data, assuming a nonlinear power law with exponent 1/4. The lighter dashed lines above and below the solid black prediction curve from theory represent error bars due to the uncertainty in measuring the fluid properties.	131
Figure 6.2	Comparison of the two methods (numerical simulations of the full equation and the zero dispersion limit) for deriving the boundary condition for a step size $A_- = 4$, with breaking occurring at $z_0 = 50$	135
Figure 6.3	Comparison of DSW data collected on leading edge speed and amplitude versus theoretical predictions.	138
Figure 6.4	Example of the typical evolution of a conduit DSW with $A_- \approx 4.3$ and leading edge amplitude $a_+ \approx 18$. Note that the individual images were downsampled in the vertical direction by a factor of 10 as described. This experiment was qualitative, so the front propagation speed was not measured.	139
Figure 6.5	Example of backflow in a DSW with $A_- \approx 7.4$ and leading edge amplitude $a_+ \approx 37$. Note that the individual images were downsampled in the vertical direction by a factor of 10 as described. This experiment was qualitative, so the front propagation speed was not measured.	140
Figure 7.1	Nondimensional shock speeds by type of regularization. v_L and v_S correspond to the leading and trailing edge speeds of a UFG DSW, respectively. V is the dissipative shock speed. The vertical dotted line at $\rho_0 = 2.7$ is for comparison with the particular discontinuity simulated in figure 7.2.	151
Figure 7.2	Numerical simulation of the gNLS equation (solid) (from eqs. (7.5), (7.6)) for a DSW with $\rho_0 = 2.7$ and corresponding VSW solution (dashed). The right panel depicts the filtered solutions.	152

Figure 7.3	Numerical simulation of the gNLS equation (solid) and dissipative hydrodynamic equations (dashed) for the collision problem. The right panel depicts the filtered solutions.	152
------------	--	-----

Chapter 1

Introduction

The study of nonlinear waves owes its origins to the earliest inquiries into fluid motion and has grown into an active, interdisciplinary research community in the present day due to the wide array of physical application areas and the lack of general solution methods for the equations which govern them. In particular, propagation of nonlinear waves in conservative or approximately conservative media has garnered significant interest in recent decades as it has grown from its origins in water waves to modern applications in optics and ultracold dilute gases. Two salient features of such systems, often referred to as being of dispersive hydrodynamic type, are born out of the interplay between the wave breaking effects of nonlinearity and the spreading effects of dispersion. They are admissibility of exponentially-localized solitary wave, or soliton, solutions and the resolution of gradient catastrophe into a rank-ordered, slowly modulated wave train, as in Fig. 1.1. A rich mathematical theory for solitons and dispersively regularized shock waves (DSWs) has been developed for a broad class of problems, but much of it relies heavily on properties due to the deep mathematical structure of integrability of the underlying partial differential equation (PDE), which are often not available in physically-based models for realistic parameter values. Moreover, while general wave averaging, asymptotic techniques exist for DSWs and solitary waves, their applicability as a tool for comparison with quantitative experiments is limited to long temporal and spatial scales, where the experimental realization of

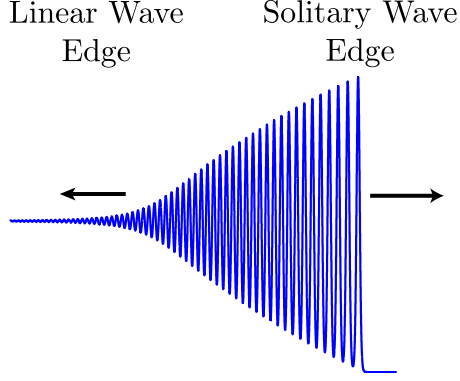


Figure 1.1: Dispersive shock wave.

dissipationless, strongly nonlinear dynamics is difficult.

The central contribution of this dissertation is the establishment of a physical setting, known as viscous fluid conduits, as an ideal platform for the study of unidirectional nonlinear dispersive waves which are truly one dimensional and dissipationless at the length and temporal scales of interest. To this end, we present the results of a threefold, interdisciplinary approach involving model derivation and analysis using analytical, asymptotic techniques, careful numerical simulations for comparison with analytical theory, and quantitative laboratory experiments for large amplitude, interacting solitary waves and DSWs. In this dissertation, we also present generalizations of the work on the conduit system which apply to the mathematical study of DSWs in general, and we explore the manifestation of dispersive hydrodynamics in another physical system, strongly interacting Fermi gas at unitarity, in which there is a question of the appropriate physical regularization of nonlinearity.

In the remainder of this chapter, we put the present work in the appropriate historical context. We begin by introducing the mathematical theory of dispersive hydrodynamics, review relevant previous experimental studies, and give an overview of previous work on the conduit system and its generalizations.

1.1 Nonlinear Waves and Modulation Theory

One dimensional dispersive hydrodynamic systems are typified by the existence of two nonlinear coherent structures: exponentially localized solitary waves and dispersively regularized shock waves (DSWs). Solitary waves arise when the competing effects of nonlinear steepening and dispersive spreading balance perfectly, forming a nonlinear analogue to the linear traveling wave, whereas DSWs occur when nonlinear wave breaking is resolved by the formation of a modulated train of solitary waves.

Nonlinear solitary waves differ from their linear counterparts in that they exhibit an amplitude-dependent phase speed, often with larger waves propagating faster than slower ones, e.g. [126]. This property gives rise to a distinguishing feature of solitary waves in one-dimension, namely the resulting nonlinear superposition which occurs when a larger, trailing solitary wave overtakes a smaller, leading solitary wave, a phenomenon previously referred to as strong interaction of solitary waves [78]. Whereas for linear waves the interaction of two localized waves is simply the sum of the two structures, the nonlinear solitary wave interaction considered here is characterized by the larger wave decreasing in height and experiencing a brief acceleration, while the smaller solitary wave increases in amplitude and experiences a shift backwards [128]. The two waves then emerge from the interaction with their initial profiles and speeds approximately restored.

Of particular interest to the present study is the physical implication of a lack of integrability and its effects on the geometry of interacting solitary waves, as integrability is typically reserved for weakly nonlinear models. The exact two soliton solution for integrable equations can be derived, e.g. [44], and in the special case of the Korteweg–de Vries (KdV) equation, a prototypical model of weakly nonlinear, dispersive waves, the soliton overtaking interaction has been classified by amplitude ratio into three distinct regimes according to the qualitative structure of the two-wave complex formed during the interaction [59]. This classification scheme for KdV is characterized solely in terms of the ratio of the initial soliton amplitudes, a manifestation of the high symmetry properties of the integrable equation. As part of this study, we extend the KdV classification scheme to the strongly nonlinear, nonintegrable regime for the viscous fluid conduit

system and find that the qualitative interaction structures are preserved, though the loss of a symmetry (Galilean invariance) outside the weakly nonlinear limit introduces an increase in the number of critical parameters required for its description.

The other dispersive hydrodynamic structure of interest here is the DSW and, again, the way in which a lack of integrability manifests in the physical realization of the DSW. While in classical, dissipative media, shocks arise when singularity formation due to nonlinearity is mediated by an irreversible transfer of energy from large to small scales resulting in the generation of heat due to viscous effects, DSWs represent the dispersive (dissipationless) analogue to the resolution of hydrodynamic singularities. In such systems, nonlinearity is regularized by the transfer of energy again from larger to smaller scales via the formation of a dynamically expanding, oscillatory wave train, but the process is conservative, i.e. reversible. This region can be characterized by nearly linear waves in one edge and a solitary wave on the other (see Fig. 1.1).

To obtain analytical information for DSWs, we use a multiscale, nonlinear wave modulation technique, generally referred to as Whitham averaging [125, 126]. In this framework, a DSW is described locally as a nonlinear, single phase, periodic wave solution to the underlying PDE. Over the scale of the wave train, however, the parameters are allowed to vary slowly, governed by a system of quasi-linear PDEs. The system is closed by matching the “inner” modulation solution to the “outer” solution, obtained by considering the dispersionless limit of the PDE, near the linear and soliton edges of the DSW. Hence the problem is converted to a free boundary problem [40]. This can be compared to the study of a classical viscous shock wave (VSW), in which one recovers a weak solution to the vanishing viscosity limit of the PDE and obtains an ordinary differential equation (ODE) for the shock speed, cf. [60]. The difference arises because a VSW is a localized phenomenon, while a DSW is continuously expanding and thus varies spatially and temporally.

The main difficulty in the study of nonintegrable, dispersive models arises in the system of modulation equations, which are generally not diagonalizable, making them difficult to solve without numerical methods. However, the work of El [24] subverts this obstacle in the case of

step initial data by assuming the existence of a simple wave solution to the modulation equations and using information available locally near the linear and soliton edges of the DSW to solve for the leading and trailing edge speeds and the soliton amplitude.

In this work, we present the application of this Whitham-El modulation theory for a generalized form of the approximate governing equation for the conduit setting. While a numerical study on the Riemann problem was conducted previously, its results were interpreted through the lens of classical shock theory, leaving several open questions which are resolved here [108, 109]. We also identify four new admissibility criteria for the modulation theory – applicable to general unidirectional, scalar, dispersive hydrodynamic models – one of which we observe for the first time in the conduit system that we term DSW implosion. Lastly, we demonstrate how the difference between VSWs and DSWs can be exploited to determine the appropriate regularization for nonlinear steepening in a system where the physical mechanism is unknown. Owing to the approximate nature of modulation theory and the nonintegrable nature of the physical settings considered, numerical methods play an integral role in each of the above studies.

1.2 Experimental Studies of Nonlinear Waves

A key component of any study in applied mathematics is that of physical relevance. However, even for integrable problems, for which Whitham modulation theory has been shown to be mathematically rigorous (e.g. the work by Lax, Levermore, and Venakides [61, 62, 63, 117]), quantitative experimental validation of the key analytical results for DSWs is largely lacking from the literature. One difficulty is the long length and time scales required to compare with the asymptotic theory. These slowly modulated wave trains are characterized by the presence of two scales. One is the $\mathcal{O}(1)$ scale of individual oscillations and the other is a long, slow scale of wave modulations $\mathcal{O}(t)$, $t \gg 1$. Large amplitude solitary waves also are generally inaccessible to experimental study due to the presence of physical dissipation, instabilities, and other physical effects neglected in deriving conservative approximate models. Here we review

notable previous experiments on DSWs and classification of interacting solitary waves in other dispersive hydrodynamic settings, noting their key results and also the limitations of the physical system and experimental set-up as a nonlinear waves platform.

Experimental validation of the Lax categories for strong interactions of solitary waves have been limited to shallow water settings and small amplitudes (necessarily less than the wave breaking amplitude ~ 0.78 in nondimensional units), due to dissipative effects and a capillary instability at larger amplitudes [114, 3]. The existence of the three distinct interaction geometries predicted for KdV, however, have been confirmed independently in [120, 21, 65]. The study of [21], while still small amplitude, was conducted just beyond the limits of validity of the KdV equation. Thus their experiments provided evidence that the existence of the three interaction types extend beyond the integrable regime.

DSW experiments have been conducted in a number of physical settings in recent decades, though quantitative comparisons with DSW theory have been limited. The first quantitative experiments were conducted in ion-acoustic plasma by [116], which examined the amplitude of the shock front generated by initial steps of varying height and compared with the weakly nonlinear KdV model. The experimental observations showed good agreement for small amplitude jumps, but the leading solitary wave amplitude quickly diverged from theory as the jump height grew. Other experiments on shock phenomena conducted in ion-acoustic plasma [115], provide only quantitative comparisons with theory for breaking time, a property of only the hydrodynamic core of the governing equations and independent of any regularization mechanism. In both studies, the DSWs created were limited to no more than ~ 10 oscillations. We note that the dissipationless assumption for ion-acoustic plasma is also an approximation, valid when the temperature of the electrons is much greater than the temperature of the ions and over sufficiently short time scales. Furthermore, comparisons with theory only involved nondimensional amplitudes, avoiding the inclusion of physical dimensional quantities necessary for comparison of, e.g., speeds.

The only other quantitative comparisons between DSW modulation theory and real physical data that we have identified were in the context of internal waves in large scale atmospheric flows.

In [89], shock properties of the Benjamin-Ono equation are compared with an observational data set for the Morning Glory phenomenon in the Gulf of Carpentaria. They report good agreement with the nondimensional amplitude of the DSW front, but not for the dimensional propagation speeds. There were also comparisons with KdV shock theory and nonlinear internal tides in Massachusetts Bay by [100] and across the Australian North West Shelf by [107]. In each of these cases, though, a weakly nonlinear model is employed, and by considering an observational data set, a number of parameter fitting assumptions were made due to lack of explicit knowledge of the physical parameters of the system. Observations of DSWs (undular bores) in water waves were also reported in channel flows by [19]. Two major limitations for DSW experiments in water waves are the presence of physical dissipation at the relevant length and time scales of the modulation theory, and the difficulty in creating a truly one-dimensional water wave without friction effects from a boundary.

Quantum superfluid settings, most notably Bose-Einstein condensates (BEC) and unitary Fermi gas (UFG), also provide experimental platforms for the study of dispersive hydrodynamics. In both systems, the idealized mean-field model is dissipationless, but this assumption applies only at absolute zero temperature, when in reality some effective dissipation is inevitably present due to experiments conducted at finite temperatures and coupling to normal fluid. There is also an issue of interpreting the results of these experiments using a one-dimensional model equation, as its applicability is restricted due to unstable transverse perturbations in the absence of sufficient confinement. Other experimental difficulties arise because the superfluid is destroyed upon imaging, making dynamic information harder to obtain. Long propagation times lead to deviation from the conservative, 1D model due to confinement effects and coupling to the uncondensed thermal cloud. Further, it is not experimentally feasible to create the idealized, step-like condition required for comparison with modulation theory. Despite these difficulties in conducting quantitative experiments, a number of notable qualitative shock experiments have appeared in the literature.

The first observation in BEC was reported in [23] where the authors observed the formation

of a small number of dispersive oscillations in response to nonlinear steepening followed by a multidimensional instability. Subsequent shock wave experiments were conducted in a rapidly rotating BEC by [106]. It was shown that the qualitative structure of shock waves observed in experiment were well-described by full 3D numerical simulations of the mean-field equation. The first qualitative comparisons with dispersive hydrodynamics are found in [46], in which two dimensional blast wave experiments were shown to exhibit similar structure to numerical simulations of the nonlinear Schrödinger (NLS) equation. Effectively one-dimensional BEC shock experiments in a cigar-shaped trap were performed by [77], and the dissipationless model was shown to exhibit good agreement with the experimental results. The results were not compared with DSW theory, however. One issue in this effectively 1D BEC case is that the experiments involve the collision of two initially separated clouds. This leads to shock formation after the interaction of two rarefaction waves, and then the resulting shocks propagate along a variable background, which is not captured by the theoretical approach. Dispersive shock waves in BEC were also created by merging initially separated clouds by [18], in which it was observed that without sufficient radial confinement, transverse instabilities lead to a distinct center bulge near the point of collision. Once again, comparisons with theory were limited to qualitative agreements with numerical simulations. The merging problem was interpreted explicitly for the first time in the context of dispersive hydrodynamics by [49], though the distinctions between pure DSWs and the BEC collision problem are identified.

Further observations of DSWs in quantum superfluids have appeared more recently in other physical settings. The merging problem for strongly interacting Fermi gas at unitarity (UFG) was presented by [52], though the resulting shock wave was interpreted by fitting the data to a hydrodynamic mean-field model with an effective viscosity. The collision problem for UFG will be considered in the dispersive hydrodynamic context by the present work in Chapter 7. In another superfluid system, liquid helium, shock formation was observed as a result of a jet hitting a surface below the superfluid transition temperature, although the results were interpreted with the introduction of an effective viscosity [92]. Nearly ten dispersive oscillations

were observed in the experiments conducted below the superfluid transition temperature, but the only quantitative characterizations made were for the radius of the shock pattern. In yet another superfluid system, the observation of hydrodynamic solitons and vortex streets in the flow of an interacting Bose gas of exciton-polaritons in the wake of a potential obstacle were reported [4], although the authors did not explore the possibility of creating a 1D shock. More recently, the formation of soliton wave trains in response to large amplitude density perturbations were observed in electron beams, and the results were compared with numerical simulations of KdV, though no comparisons with modulation theory were made [80]. While these superfluid settings allow the observation of characteristic dispersive hydrodynamic structures, the creation of step-like initial data required for the study of the fundamental shock problem has been difficult to achieve, and a complete characterization of all relevant experimental parameters is lacking.

The final notable experimental platform for DSWs is the so-called optical hydrodynamical setting, in which light waves propagate through a nonlinear Kerr-like medium. Like in ultracold atom systems, though, the optics setting does not lend the experimental fidelity needed to simulate the step problem in one propagation direction, allow long time/distance evolution, or easily capture dynamical information via imaging. Experimental observations in optics are also limited by noisy data, with no experiment described below exhibiting more than ~ 12 dispersive oscillations in response to gradient catastrophe. The first observations of wave breaking leading to dispersive oscillations were made by [93] in optical propagation along a single-mode fiber. The optical intensity data was quite noisy, with few easily discernible oscillations, but the authors showed qualitative agreement with numerical simulations of the NLS equation. Optical DSW experiments were conducted in nonlocal, nonlinear media using spatial beams in a thermal liquid cell by [8] via the formation of an initial, localized intensity perturbation. Quantitative measurements are made for the shock speed (assumed to be determined by the shock width) as a function of the size of the initial disturbance, although the data are fit to a scaling law and never compared to the theoretical speed predicted by modulation theory. Similar experiments were conducted in an all-optical experimental platform, where again the relevant measurements were

shock speeds as a function of initial disturbance amplitude, fit to an assumed relationship and not compared with DSW theory [119]. Novel, multidimensional interacting DSW observations were also made and described in detail. DSWs were also created and studied experimentally in nonlinear waveguide arrays in [50], though quantitative and dynamical information were not reported. Optical DSWs in the spatial propagation of Gaussian laser beams in nonlocal, nonlinear media were observed to exist [35]. In later investigations of optical intensity shocks in thermal nonlocal media, measurements of the breaking distance were compared with NLS theory [34], but this property is independent of dispersive/dissipative regularization. The breaking time was also measured in the propagation of large amplitude dark beams in a defocusing medium by [20]. Optical wave breaking was recently observed in pulse propagation in a nonlinear photonic crystal fiber and considered in the context of pulse compression [67]. The results were compared with numerical simulations of a generalized NLS equation, but shock features were not compared with modulation theory.

1.3 Viscous Fluid Conduits as 1D Superfluids

As demonstrated in the previous section, there is not a quantitative experimental platform for the controlled study of one-dimensional DSWs. Solitons have also been studied in many physical systems, but their detailed quantitative study and comparison with theory is often limited for similar reasons as DSWs. The main contribution of this thesis is in establishing a new fluid system, viscous fluid conduits, as a medium to study solitons and DSWs, and conducting quantitative experiments.

The viscous fluid conduit setting is realized by introducing a steady source of buoyant, viscous fluid to a quiescent medium of heavier, more viscous fluid. Following transient dynamics, a stable, fluid-filled pipe is formed if the Reynolds number of the system is sufficiently low [124]. The interest of this study is in the evolution of the interface separating the two fluids when slowly varying perturbations of the injection rate are introduced. To fully describe the behavior of this multi-fluid system, one must consider the full system of Navier-Stokes equations with

jumps in density, viscosity, and pressure along a free, moving interface, a difficult task even for direct numerical simulations.

An approximate model equation was previously proposed on the basis of physical arguments. In the limit of gently sloping conduit walls, buoyant disturbances propagating upward along the interface induced by unsteady injection are balanced by a viscous restoring force due to the exterior fluid [83, 99, 43]. Upon invoking mass conservation, one can describe the dynamics of the system in terms of only a nonlinear, dispersive PDE for the cross-sectional area of the conduit formed by the interior fluid. Though the approximate model was shown to be in excellent quantitative agreement when compared with solitary wave speeds and post-interaction solitary wave behavior in experiments, its limitations were in the lack of a precise determination of the parameter regimes of validity and a careful mathematical derivation. As part of this study, we present the details of a systematic, multiple scales approach to the derivation of the approximate model equation, which affords us knowledge of the breakdown of the model equation under higher order physical effects neglected in modeling.

One key result is that the model derivation requires only a long wavelength assumption and is valid for large amplitude disturbances, for long times and large spatial extents. This is in stark contrast with well-known models of small amplitude, weakly nonlinear, interfacial fluid dynamics such as the KdV [57] and Benjamin-Ono [10, 84] equations, making the resulting conduit equation a scalar analogue for the Green-Naghdi (or Serre, Su-Gardner) equations of large amplitude, shallow water waves [101, 112, 38]. Moreover, large amplitude conduit solitary waves are asymptotically stable [105], exhibit good agreement with experiments [99, 83, 43], and are robust, physical features of viscous fluid conduit interfacial dynamics.

With the limits of validity of the theoretical model established and the robustness of nonlinear wave phenomena observable using a relatively simple tabletop experimental set-up, viscous fluid conduits provide an optimal setting for the precise, quantitative, experimental study of DSWs and large amplitude solitary wave interactions. This work was inspired by images from previous experiments which demonstrated that the study of DSWs is accessible in viscous fluid

conduits, see, e.g., Figure 18 in the review article [123], though they were never interpreted as such. As part of this work, the NC State Dispersive Shock Wave Laboratory was established with the purpose to study nonlinear wave phenomena in viscous fluid conduits. In this thesis, we present the results of quantitative experiments on large amplitude interacting solitary waves and systematic investigations into dispersive shock waves.

Interpretation of wave propagation in viscous fluid conduits from the viewpoint of dispersive hydrodynamics offers enlightening parallels with the examples of dissipationless flows discussed in the previous section, in particular with quantum superfluids. Typically, superfluidity is a property of fluid-like flows in which internal friction (or viscosity) is negligible, with standard examples being BEC and UFG. While one test for superfluidity in two and three dimensions in such systems is the appearance of quantized vortices, solitons and DSWs are fundamental excitations characteristic of dissipationless, superfluid-like media and represent the 1D analogue of quantized vortices. So while it is counterintuitive that wave propagation in a medium dominated by viscosity could exhibit no physical dissipation, we find that viscous fluid conduits provide a well-understood, controlled, table-top platform in which to study universal properties of 1D superfluidity.

Chapter 2

Derivation of an Approximate Interfacial Equation

In this chapter, we present the asymptotic derivation of an approximate model for the viscous fluid conduit system. We describe the physical system of interest, identify the key assumptions required for the reduced model, and provide insight into the effects of higher order physical processes. The contents of this chapter are based on the following publication [68]:

Lowman, N. K. and Hofer, M. A. 2013 “Dispersive hydrodynamics in viscous fluid conduits,” *Journal of Fluid Mechanics* **88**, 023016.

2.1 Abstract

The evolution of the interface separating a conduit of light, viscous fluid rising buoyantly through a heavy, more viscous, exterior fluid at small Reynolds numbers is governed by the interplay between nonlinearity and dispersion. Previous authors have proposed an approximate model equation based on physical arguments, but a precise theoretical treatment for this two fluid system with a free boundary is lacking. Here, a derivation of the interfacial equation via a multiple scales, perturbation technique is presented. Perturbations about a state of vertically

uniform, laminar conduit flow are considered in the context of the Navier-Stokes equations with appropriate boundary conditions. The ratio of interior to exterior viscosities is the small parameter used in the asymptotic analysis, which leads systematically to a maximal balance between buoyancy driven, nonlinear self-steepening and viscous, interfacial stress induced, nonlinear dispersion. This results in a scalar, nonlinear partial differential equation describing large amplitude dynamics of the cross-sectional area of the intrusive fluid conduit, in agreement with previous derivations. The leading order behavior of the two fluid system is completely characterized in terms of the interfacial dynamics. The regime of model validity is characterized and shown to agree with previous experimental studies. Viscous fluid conduits provide a robust setting for the study of nonlinear, dispersive wave phenomena.

2.2 Introduction

Upon introduction of a steady source of light, viscous fluid into the base of a quiescent basin of dense, more viscous fluid, a diapir will form. Once the radius of the diapir exceeds a critical threshold, the diapir will rise buoyantly through the exterior fluid, trailed by a vertically uniform, axisymmetric conduit, if its Reynolds number (Re) is sufficiently low [124]. Unsteady perturbations of the injection rate have been shown in a laboratory setting to produce hallmark features of nonlinear, dispersive systems including solitary waves and nonlinear wavetrains (cf. the review in [123]). To fully describe the behavior of this miscible, two-fluid, interfacial flow, one must consider the full system of governing equations with boundary conditions along a moving, free interface, a difficult task even for numerical simulations. However, an approximate model equation has been proposed on the basis of physical arguments. In the limit of gently sloping conduit walls, disturbances propagating upward along the interface of the conduit induced by unsteady injection are balanced by viscous forces from the exterior, resulting in wave propagation [83, 99, 43]. Utilizing the conduit geometry, the leading order evolution of the system can be described in terms of the (dimensionless) cross-sectional area of the conduit, A , by the nonlinear,

dispersive, scalar partial differential equation (PDE)

$$\frac{\partial A}{\partial t} + \frac{\partial}{\partial z} \left\{ A^2 \left[1 - \frac{\partial}{\partial z} \left(A^{-1} \frac{\partial A}{\partial t} \right) \right] \right\} = 0 , \quad (2.1)$$

we term the conduit equation. The relative ease of realizing this viscous conduit setting in experiment and the analytical tractability of the model equation (2.1) make this an ideal platform for the study of nonlinear, dispersive waves.

Interest in viscous fluid conduits began in the geophysics community nearly three decades ago and has continued to the present day due to the prominence of fundamental nonlinear wave phenomena. This simplified system is thought to capture the essential physics of magma rising buoyantly along thermal plumes in the convecting mantle [83, 99] and is closely related to interpenetrating magma flow in a viscously deformable, porous matrix where the cross-sectional area of the conduit is comparable to the matrix porosity [75, 97, 98, 104]. Like in the conduit setting, the primitive equations for interpenetrating magma flow can be reduced to eq. (2.1) in the proper physical setting, thus it is commonly referred to as the magma equation. While counterintuitive at first, that in both settings, viscosity-dominated dynamics lead to a conservative (dissipationless) equation, this is natural in the conduit setting because (2.1) is simply an expression for mass conservation of the conduit fluid.

In the context of viscous fluid conduits, time evolution of the conduit area is driven by a nonlinear self-steepening term due to buoyancy and a dispersive term due to viscous stress imparted by slow deformation of the exterior fluid. Solitary waves supported by the conduit equation have been studied in detail analytically and shown to be asymptotically stable (e.g. [97, 82, 105]). These solitary waves are readily observable in experiment by the generation of a localized pulse in the rate of injection, and careful comparisons between the theoretical amplitude-speed relation of eq. (2.1) and experimental data yield good agreement for small to moderate amplitude solitary waves [83, 99, 43], though a precise explanation of the deviation between theory and experiment has not been identified. The conduit equation has also been shown

theoretically and numerically to produce slowly modulated, dynamically expanding, periodic wavetrains in response to nonlinear steepening, whose speeds and amplitudes can be analytically predicted using a nonlinear wave averaging technique [108, 109, 69]. These wavetrains correspond to dispersively regularized shock waves (DSWs)—analogous to classical, viscous shocks—which have garnered significant attention in the past decade due to their realization in optics and superfluids [45]. DSWs in viscous fluid conduits have been observed experimentally [99, 123], but their properties have never been studied.

A major hindrance to a more robust, quantitative study of nonlinear, dispersive waves in this system is the lack of a systematic derivation of the conduit equation from the full Navier-Stokes equations. In this work, we present a derivation of eq. (2.1) utilizing a multiple scales, perturbation approach, providing confirmation of existing intuitive arguments. This derivation results in a complete characterization of the leading order behavior of the system (intrusive/exterior fluid velocities and pressures) in terms of $A(z, t)$. It is found that the vertical flow in the conduit imposes a shear stress on the interface, driving a weak vertical velocity in the exterior fluid which persists far from the conduit walls, presently neglected in existing derivations. Scaling relations between the fluid quantities are made explicit. Model validity is characterized in terms of two independent parameters, the ratio of internal to external fluid viscosities

$$\epsilon = \mu^{(i)} / \mu^{(e)} , \quad (2.2)$$

and the internal fluid's Reynolds number $\text{Re}^{(i)}$. When $\epsilon \ll 1$ and $\text{Re}^{(i)} = \mathcal{O}(1)$, eq. (2.1) is valid for times $t \ll 1/\epsilon$ and amplitudes $A \ll 1/\epsilon$. This translates to dimensional time units $T/\epsilon^{3/2}$, where the characteristic time scale T is typically on the order of seconds or tenths of seconds. In contrast to well-known models of *weakly* nonlinear, interfacial fluid dynamics such as the Korteweg-deVries [57] and Benjamin-Ono equations [10, 84], the conduit equation is valid for *arbitrarily large* amplitudes assuming ϵ is sufficiently small. This more closely resembles the one-dimensional, nonlinear, dispersive Serre (or Green-Naghdi) equations, which are an approximate model of large amplitude, interfacial dynamics in inviscid, irrotational shallow

water [101, 112, 38]. Finally, we determine the regime of model validity when inertial, external boundary, surface tension, higher order viscous, and symmetry-breaking effects are present.

The remainder of the article will be organized in the following manner. Section 2.3 describes the governing equations and their nondimensionalization, as well as the normalization of the fluid properties to the appropriate scales of interest. In § 2.4, we present the implementation of the perturbation method to derive the conduit equation. Information about its higher order corrections from the full set of nondimensional equations is provided in § 2.5. The manuscript is concluded with discussion of physical implications and future directions in § 2.6.

2.3 Problem Description

The purpose of this section is to describe the mathematical formulation of wave propagation along an established, vertically uniform conduit, illustrated schematically in Fig. 2.1. We consider an intrusive conduit fluid of density $\rho^{(i)}$ and viscosity $\mu^{(i)}$ in an extended domain denoted $V^{(i)}$, propagating within an exterior fluid with density $\rho^{(e)}$, viscosity $\mu^{(e)}$, and domain $V^{(e)}$. The present analysis is primarily concerned with capturing the interactions in an axially symmetric conduit between buoyant forcing of the intrusive fluid due to unsteady injection and viscous stress at the conduit boundary due to the exterior fluid. This requires the basic assumption that the intrusive fluid is less dense, $\rho^{(i)} < \rho^{(e)}$, and that the viscosity of the intrusive fluid is much smaller than for the exterior fluid, i.e. $\epsilon \ll 1$. We will adopt the convention that $\hat{\mathbf{n}}_c$ represents the inward pointing unit normal to the conduit surface. The unit tangent to the conduit $\hat{\mathbf{t}}_c$ is oriented so that it always has a positive vertical component. It is also necessary to define the unit normal of cross-sectional disks along the conduit, denoted $\hat{\mathbf{n}}_d$, oriented upward (see Fig. 2.1).

Before proceeding, we present a brief word on the notation used in this work. We use the cylindrical coordinate system, assuming azimuthal symmetry (r, z) (see Fig. 2.1). Bold symbols correspond to vectors or tensors while non-bold symbols indicate scalar quantities. The only superscripts we use $(\cdot^{(i)}, \cdot^{(e)})$ denote quantities associated with the intrusive or exterior fluid,

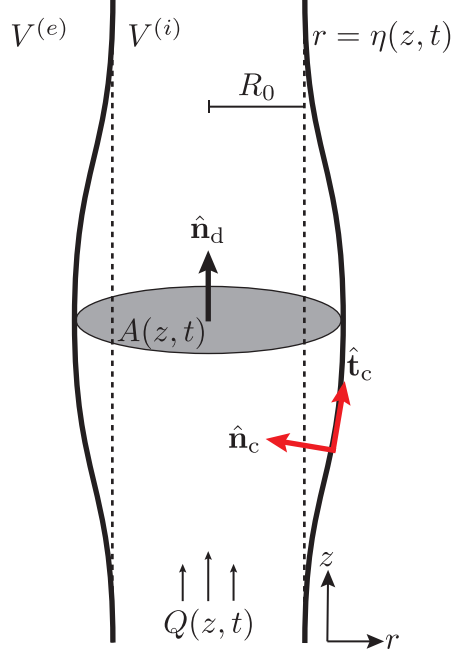


Figure 2.1: Geometry of an axisymmetric, intrusive fluid conduit occupying a domain $V^{(i)}$ flowing within a dense, exterior fluid of higher viscosity in a domain $V^{(e)}$. The dashed line denotes an unperturbed conduit of radius R_0 , and the solid line is the conduit with some disturbance. Relevant physical quantities are noted, as well as the sign conventions for the conduit unit normal vector, \hat{n}_c , conduit unit tangent vector, \hat{t}_c , and cross-sectional disk unit normal vector, \hat{n}_d .

respectively. Subscripts of non-bold symbols correspond either to the coefficients of the velocity basis in cylindrical coordinates, e.g.

$$\mathbf{u}^{(i,e)} = \begin{bmatrix} u_r^{(i,e)} \\ u_z^{(i,e)} \end{bmatrix}, \quad (2.3)$$

or numerical ordering in an asymptotic sequence. Note that due to axisymmetry, we only consider two vector components. A jump in the fluid quantity β is denoted

$$[\beta]_j = \beta^{(e)} - \beta^{(i)}, \quad (2.4)$$

evaluated at the fluid-fluid interface.

2.3.1 Governing Equations

The complete description of the interaction between two incompressible fluids of constant densities is given by the continuity equation for mass conservation, coupled with the Navier-Stokes equation for linear momentum conservation, which can be written compactly as

$$\nabla \cdot \mathbf{u}^{(i,e)} = 0 , \quad (2.5a)$$

$$\rho^{(i,e)} \frac{d\mathbf{u}^{(i,e)}}{dt} = -\nabla p^{(i,e)} + \nabla \cdot \boldsymbol{\sigma}^{(i,e)} . \quad (2.5b)$$

We will utilize cylindrical coordinates assuming azimuthal symmetry and that the force due to gravity is the only external force. Then $\mathbf{u}^{(i,e)} = \left(u_r^{(i,e)}, u_z^{(i,e)} \right)$ represents the velocity vectors for the two fluids, d/dt is the material derivative operator, and $\boldsymbol{\sigma}^{(i,e)} = \mu^{(i,e)} \left[\nabla \mathbf{u} + (\nabla \mathbf{u})^T \right]$ is the deviatoric stress tensor. The modified pressure $p^{(i,e)}$, or the pressure deviation from hydrostatic, can be written as the sum $p^{(i,e)} = \rho^{(i,e)} g z + P^{(i,e)}$, where $P^{(i,e)}$ is the absolute pressure. We initially assume that the conduit has infinite vertical extent and the external fluid extends infinitely in the radial direction.

Along the center axis $r = 0$, symmetry and perturbation of a vertically uniform conduit lead us to require that the intrusive fluid satisfy

$$\frac{\partial u_z^{(i)}}{\partial r} = u_r^{(i)} = \frac{\partial p^{(i)}}{\partial r} = 0 , \quad r = 0 . \quad (2.6)$$

In the far-field limit $r \rightarrow \infty$, we require the exterior fluid velocity field $\mathbf{u}^{(e)}$ and (modified) pressure $p^{(e)}$ decay to zero. The boundary between the two fluids is represented by the level curves $r = \eta(z, t)$. The conduit area is therefore

$$A(z, t) = \pi \eta^2(z, t) . \quad (2.7)$$

The boundary is treated as a material surface, which requires the kinematic condition

$$u_r^{(i)} = \frac{\partial \eta}{\partial t} + u_z^{(i)} \frac{\partial \eta}{\partial z}, \quad r = \eta(z, t), \quad (2.8)$$

in addition to continuity of normal and tangential components of the velocity

$$[\mathbf{u} \cdot \hat{\mathbf{n}}_c]_j = [\mathbf{u} \cdot \hat{\mathbf{t}}_c]_j = 0, \quad r = \eta(z, t). \quad (2.9)$$

The last conditions along the fluid-fluid interface which must be satisfied are the balance of normal and tangential stresses, which for general settings are written

$$[\hat{\mathbf{n}}_c \cdot \mathbf{T} \cdot \hat{\mathbf{n}}_c]_j = -(\nabla \cdot \hat{\mathbf{n}}_c) \gamma, \quad r = \eta(z, t), \quad (2.10a)$$

$$[\hat{\mathbf{t}}_c \cdot \mathbf{T} \cdot \hat{\mathbf{n}}_c]_j = \nabla_s \gamma \cdot \hat{\mathbf{t}}_c, \quad r = \eta(z, t), \quad (2.10b)$$

where $\mathbf{T}^{(i,e)} = -P^{(i,e)}\mathbf{I} + \boldsymbol{\sigma}^{(i,e)}$ is the stress tensor, \mathbf{I} is the identity operator, γ is the surface tension, and $\nabla_s = (\mathbf{I} - \hat{\mathbf{n}}_c \otimes \hat{\mathbf{n}}_c) \cdot \nabla$ is the surface gradient operator for the interface. For a more detailed description of the fluid equations and boundary conditions, see e.g. [9].

Since the conduit equation (2.1) is a PDE for the cross-sectional area, it is also convenient to derive an expression which relates the fluid properties to $A(z, t)$ [99, 83]. First, the volumetric flow rate Q through vertical cross-sections of the conduit (see Fig. 2.1) is defined to be

$$Q(z, t) = 2\pi \int_0^{\eta(z, t)} \mathbf{u}^{(i)} \cdot \hat{\mathbf{n}}_d r \, dr. \quad (2.11)$$

Utilizing the conduit geometry, one can write the integral form of the continuity equation for cross-sectional disks as a limit of vertical cylinders of vanishing height δz as

$$\frac{\partial A}{\partial t} + \lim_{\delta z \rightarrow 0} \frac{2\pi}{\delta z} \left(\int_0^{\eta(z+\delta z, t)} \mathbf{u}^{(i)} \cdot \hat{\mathbf{n}}_d r \, dr - \int_0^{\eta(z, t)} \mathbf{u}^{(i)} \cdot \hat{\mathbf{n}}_d r \, dr \right) = 0. \quad (2.12)$$

This can be compactly written as

$$\frac{\partial A}{\partial t} + \frac{\partial Q}{\partial z} = 0 . \quad (2.13)$$

Thus the cross-sectional area of the conduit is related to the fluid properties through the intrusive fluid velocity, in particular the vertical velocity $u_z^{(i)}$ for an axisymmetric conduit.

2.3.2 Uniform Pipe Flow and Nondimensionalization

The equations of motion will now be nondimensionalized about a state of steady, vertically uniform, conduit flow, which takes the form of a generalized Pouseuille (pipe) flow in the limit of small Re and negligible surface tension [124]. In this setting, the intrusive equations are reduced to $u_r^{(i)} = 0$, and the vertical velocity is driven by a vertical pressure gradient according to eq. (2.5b)

$$\frac{1}{\mu^{(i)}} \frac{\partial p^{(i)}}{\partial z} = \frac{1}{r} \frac{\partial}{\partial r} \left(r \frac{\partial u_z^{(i)}}{\partial r} \right) , \quad (2.14)$$

where $p^{(i)}$ is a function of z alone and the interface is fixed at $r = R_0$. On the exterior, the velocities are small relative to the pressure, which leaves only hydrostatic pressure balance, i.e. $P^{(e)} = -\rho^{(e)}gz + p_0$, where p_0 is a constant reference pressure. Note that these relative scaling arguments will be made more precise in § 2.4, as here we seek only a background scale about which to perturb. Imposing the boundary condition (2.10a) and neglecting surface tension effects yields an expression for the intrusive pressure

$$p^{(i)} = \left(\rho^{(i)} - \rho^{(e)} \right) gz + p_0 . \quad (2.15)$$

Substituting the pressure (2.15) into the velocity equation (2.14), performing two integrations, and imposing the boundary conditions (2.6) and (2.9), leads to the generalized pipe flow velocity for the intrusive fluid

$$u_z^{(i)} = \frac{g}{4\mu^{(i)}} \left(\rho^{(e)} - \rho^{(i)} \right) (R_0^2 - r^2) . \quad (2.16)$$

Upon substitution into the tangential stress balance condition (2.10b) and neglecting surface tension, we find that the exterior fluid must have a vertical velocity which satisfies

$$\frac{\partial u_z^{(e)}}{\partial r} = \frac{\mu^{(i)}}{\mu^{(e)}} \frac{\partial u_z^{(i)}}{\partial r} \Big|_{r=R_0}, \quad (2.17)$$

and thus is proportional to the small parameter ϵ .

In section 2.4, we will perturb the interface of the steadily flowing conduit, so eq. (2.16) provides natural length and velocity scales of interest. Previous studies have invoked a small slope assumption on conduit perturbations [99, 83, 43] but have not explicitly identified the appropriate vertical length scale. We now provide the precise scaling and nondimensionalization for the governing equations that will lead to a maximal balance between buoyant and viscous stress effects. The radial length scale L is proportional to the uniform conduit radius while vertical variations are assumed to be weak according to

$$\tilde{r} = r/L, \quad \tilde{z} = \epsilon^{1/2} z/L, \quad L = R_0/\sqrt{8}. \quad (2.18)$$

The proportionality constant in the characteristic length L is chosen for convenience in working with the governing equations but will be rescaled to arrive at the standard form of the conduit equation (2.1). The boundary is now denoted by $r = \eta(z, t) = R_0 + R'(z, t)$, or $\tilde{r} = (R_0 + R'(z, t))/L \equiv \tilde{R}(\tilde{z}, \tilde{t})$. Hence the unit normal and tangent vectors for the conduit are given by

$$\hat{\tilde{\mathbf{n}}}_c = \frac{1}{\|\tilde{\mathbf{n}}_c\|} \begin{bmatrix} -1 \\ \epsilon^{1/2} \frac{\partial \tilde{R}}{\partial \tilde{z}} \end{bmatrix}, \quad \hat{\tilde{\mathbf{t}}}_c = \frac{1}{\|\tilde{\mathbf{t}}_c\|} \begin{bmatrix} \epsilon^{1/2} \frac{\partial \tilde{R}}{\partial \tilde{z}} \\ 1 \end{bmatrix}, \quad (2.19a)$$

where

$$\|\tilde{\mathbf{n}}_c\| = \|\tilde{\mathbf{t}}_c\| = \left[1 + \epsilon \left(\frac{\partial \tilde{R}}{\partial \tilde{z}} \right)^2 \right]^{-1/2}. \quad (2.20)$$

Velocities are normalized to the radially-averaged vertical velocity of the uniform conduit

$$\tilde{\mathbf{u}}^{(i,e)} = \mathbf{u}^{(i,e)}/U \ , \quad U = \frac{gR_0^2 (\rho^{(e)} - \rho^{(i)})}{8\mu^{(i)}} \ , \quad (2.21)$$

leading to the long time scale $\epsilon^{-1/2}T$ for vertical dynamics where

$$\tilde{t} = \epsilon^{1/2}t/T \ , \quad T = L/U \ . \quad (2.22)$$

To nondimensionalize the pressure, the characteristic scale Π is chosen so that the vertical pressure gradient within the conduit balances the viscous force due to radial variation in the vertical velocity,

$$\tilde{p}^{(i,e)} = \epsilon^{1/2} \frac{p^{(i,e)} - p_0}{\Pi} \ , \quad \Pi = \mu^{(i)}U/L \ . \quad (2.23)$$

Like in dimensional variables, the nondimensional, modified pressure can be decomposed as $\tilde{p}^{(i,e)} = \tilde{P}^{(i,e)} - \tilde{p}_h^{(i,e)}$, where $\tilde{P}^{(i,e)} = \epsilon^{1/2}P^{(i,e)}/\Pi$ is the scaled, absolute pressure and $\tilde{p}_h^{(i,e)}$ is the normalized hydrostatic pressure which takes the form

$$\tilde{p}_h^{(i,e)} = -\epsilon^{1/2} \frac{\rho^{(i,e)}gz}{\Pi} = \frac{-\rho^{(i,e)}\tilde{z}}{\rho^{(e)} - \rho^{(i)}} \ . \quad (2.24)$$

Surface tension was neglected in the discussion of the uniform conduit, but it will be included in the full system of equations for completeness, so it is normalized about a characteristic scale Γ :

$$\tilde{\gamma} = \gamma/\Gamma \ . \quad (2.25)$$

The Reynolds numbers for the viscous fluid conduit system are therefore defined for the two fluids according to

$$\text{Re}^{(i,e)} = \frac{\rho^{(i,e)} (\epsilon^{-1/2}L) U}{\mu^{(i,e)}} \ . \quad (2.26)$$

Note that $\text{Re}^{(e)} = \epsilon (\rho^{(e)}/\rho^{(i)}) \text{Re}^{(i)}$. While $\rho^{(i)} < \rho^{(e)}$, we typically consider fluids where $\text{Re}^{(e)} \ll \text{Re}^{(i)}$.

The governing equations in nondimensional form are obtained by direct substitution of the above scalings into the set of dimensional equations and boundary conditions. For the intrusive fluid, the nondimensional continuity equation (2.5a) is

$$\frac{1}{\tilde{r}} \frac{\partial}{\partial \tilde{r}} \left(\tilde{r} \tilde{u}_{\tilde{r}}^{(i)} \right) + \epsilon^{1/2} \frac{\partial \tilde{u}_{\tilde{z}}^{(i)}}{\partial \tilde{z}} = 0 , \quad (2.27)$$

and linear momentum balance (2.5b) requires

$$\text{Re}^{(i)} \frac{d^{(i)} \tilde{u}_{\tilde{r}}^{(i)}}{d\tilde{t}} = -\epsilon^{-3/2} \frac{\partial \tilde{p}^{(i)}}{\partial \tilde{r}} + \tilde{\nabla}^2 \tilde{u}_{\tilde{r}}^{(i)} - \epsilon^{-1} \frac{\tilde{u}_{\tilde{r}}^{(i)}}{\tilde{r}^2} , \quad (2.28a)$$

$$\text{Re}^{(i)} \frac{d^{(i)} \tilde{u}_{\tilde{z}}^{(i)}}{d\tilde{t}} = -\epsilon^{-1} \frac{\partial \tilde{p}^{(i)}}{\partial \tilde{z}} + \tilde{\nabla}^2 \tilde{u}_{\tilde{z}}^{(i)} , \quad (2.28b)$$

where

$$\frac{d^{(i,e)}}{d\tilde{t}} = \frac{\partial}{\partial \tilde{t}} + \left(\tilde{\mathbf{u}}^{(i,e)} \cdot \tilde{\nabla} \right) , \quad (2.29)$$

and

$$\tilde{\nabla} = \epsilon^{-1/2} \frac{\partial}{\partial \tilde{r}} + \frac{\partial}{\partial \tilde{z}} , \quad \tilde{\nabla}^2 = \epsilon^{-1} \frac{1}{\tilde{r}} \frac{\partial}{\partial \tilde{r}} \left(\tilde{r} \frac{\partial}{\partial \tilde{r}} \right) + \frac{\partial^2}{\partial \tilde{z}^2} . \quad (2.30)$$

For the exterior fluid, mass conservation (2.5a) is similarly

$$\frac{1}{\tilde{r}} \frac{\partial}{\partial \tilde{r}} \left(\tilde{r} \tilde{u}_{\tilde{r}}^{(e)} \right) + \epsilon^{1/2} \frac{\partial \tilde{u}_{\tilde{z}}^{(e)}}{\partial \tilde{z}} = 0 , \quad (2.31)$$

and momentum balance (2.5b) requires

$$\text{Re}^{(e)} \frac{d^{(e)} \tilde{u}_{\tilde{r}}^{(e)}}{d\tilde{t}} = -\epsilon^{-1/2} \frac{\partial \tilde{p}^{(e)}}{\partial \tilde{r}} + \tilde{\nabla}^2 \tilde{u}_{\tilde{r}}^{(e)} - \epsilon^{-1} \frac{\tilde{u}_{\tilde{r}}^{(e)}}{\tilde{r}^2} , \quad (2.32a)$$

$$\text{Re}^{(e)} \frac{d^{(e)} \tilde{u}_{\tilde{z}}^{(e)}}{d\tilde{t}} = -\frac{\partial \tilde{p}^{(e)}}{\partial \tilde{z}} + \tilde{\nabla}^2 \tilde{u}_{\tilde{z}}^{(e)} . \quad (2.32b)$$

The boundary conditions along the axis of symmetry $\tilde{r} = 0$, given by eq. (2.6), are now

$$\frac{\partial \tilde{u}_{\tilde{z}}^{(i)}}{\partial \tilde{r}} = 0, \quad \tilde{u}_{\tilde{r}}^{(i)} = 0, \quad \frac{\partial \tilde{p}^{(i)}}{\partial \tilde{r}} = 0, \quad \tilde{r} = 0, \quad (2.33)$$

and the far-field boundary condition still requires that the exterior fluid velocities and (modified) pressure decay as $\tilde{r} \rightarrow \infty$. The kinematic boundary condition (2.8) becomes

$$\tilde{u}_{\tilde{r}}^{(i)} = \epsilon^{1/2} \left(\frac{\partial \tilde{R}}{\partial \tilde{t}} + \tilde{u}_{\tilde{z}}^{(i)} \frac{\partial \tilde{R}}{\partial \tilde{z}} \right), \quad \tilde{r} = \tilde{R}(\tilde{z}, \tilde{t}), \quad (2.34)$$

and couples to the equations for continuity of the velocity components (2.9), which are now

$$\left(\tilde{u}_{\tilde{r}}^{(i)} - \tilde{u}_{\tilde{r}}^{(e)} \right) = \epsilon^{1/2} \frac{\partial \tilde{R}}{\partial \tilde{z}} \left(\tilde{u}_{\tilde{z}}^{(i)} - \tilde{u}_{\tilde{z}}^{(e)} \right), \quad (2.35a)$$

$$\left(\tilde{u}_{\tilde{z}}^{(e)} - \tilde{u}_{\tilde{z}}^{(i)} \right) = \epsilon^{1/2} \frac{\partial \tilde{R}}{\partial \tilde{z}} \left(\tilde{u}_{\tilde{r}}^{(i)} - \tilde{u}_{\tilde{r}}^{(e)} \right). \quad (2.35b)$$

To nondimensionalize the stress balance conditions (2.10), the normalized deviatoric stress tensor $\tilde{\boldsymbol{\sigma}}^{(i,e)} = \epsilon^{1/2} (L/\mu^{(i,e)} U) \boldsymbol{\sigma}^{(i,e)}$ can be written

$$\tilde{\boldsymbol{\sigma}}^{(i,e)} = \begin{bmatrix} \tilde{\sigma}_{\tilde{r}\tilde{r}}^{(i,e)} & \tilde{\sigma}_{\tilde{r}\tilde{z}}^{(i,e)} \\ \tilde{\sigma}_{\tilde{z}\tilde{r}}^{(i,e)} & \tilde{\sigma}_{\tilde{z}\tilde{z}}^{(i,e)} \end{bmatrix} = \epsilon^{1/2} \begin{bmatrix} 2 \frac{\partial \tilde{u}_{\tilde{r}}^{(i,e)}}{\partial \tilde{r}} & \frac{\partial \tilde{u}_{\tilde{z}}^{(i,e)}}{\partial \tilde{r}} + \epsilon^{1/2} \frac{\partial \tilde{u}_{\tilde{r}}^{(i,e)}}{\partial \tilde{z}} \\ \frac{\partial \tilde{u}_{\tilde{z}}^{(i,e)}}{\partial \tilde{r}} + \epsilon^{1/2} \frac{\partial \tilde{u}_{\tilde{r}}^{(i,e)}}{\partial \tilde{z}} & 2 \epsilon^{1/2} \frac{\partial \tilde{u}_{\tilde{z}}^{(i,e)}}{\partial \tilde{z}} \end{bmatrix}. \quad (2.36)$$

Then the nondimensional stress balance conditions in the normal and tangential directions become, respectively,

$$\begin{aligned} & \left[-\|\tilde{\mathbf{n}}_c\|^2 \tilde{P} + \kappa \left(\tilde{\sigma}_{\tilde{r}\tilde{r}} - 2 \epsilon^{1/2} \frac{\partial \tilde{R}}{\partial \tilde{z}} \tilde{\sigma}_{\tilde{r}\tilde{z}} + \epsilon \left(\frac{\partial \tilde{R}}{\partial \tilde{z}} \right)^2 \tilde{\sigma}_{\tilde{z}\tilde{z}} \right) \right]_{\text{j}} \\ &= \frac{\epsilon^{1/2} \|\tilde{\mathbf{n}}_c\|}{\text{Ca}} \left(\frac{1}{\tilde{R}} - \epsilon \frac{\partial^2 \tilde{R}}{\partial \tilde{z}^2} \right) \tilde{\gamma} \bigg|_{\tilde{r}=\tilde{R}(\tilde{z}, \tilde{t})}, \end{aligned} \quad (2.37a)$$

$$\begin{aligned}
& \left[\kappa \left\{ - \left(1 - \epsilon \left(\frac{\partial \tilde{R}}{\partial \tilde{z}} \right)^2 \right) \tilde{\sigma}_{\tilde{r}\tilde{z}} + \epsilon^{1/2} \frac{\partial \tilde{R}}{\partial \tilde{z}} (\tilde{\sigma}_{\tilde{z}\tilde{z}} - \tilde{\sigma}_{\tilde{r}\tilde{r}}) \right\} \right]_{\text{j}} \\
& = \frac{\epsilon \|\tilde{\mathbf{n}}_{\text{c}}\|}{\text{Ca}} \left(\frac{\partial}{\partial \tilde{z}} + \frac{\partial \tilde{R}}{\partial \tilde{z}} \frac{\partial}{\partial \tilde{r}} \right) \tilde{\gamma} \Big|_{\tilde{r}=\tilde{R}(z,t)},
\end{aligned} \tag{2.37b}$$

where κ is a fluid-specific coefficient such that $\kappa^{(e)} = \epsilon^{-1}$, $\kappa^{(i)} = 1$ and the capillary number is defined to be $\text{Ca} = \mu^{(i)} U / \Gamma$.

This is now a complete system of nondimensional equations with boundary conditions. It is important to note that the system of equations to this point is general, with no approximations.

2.4 Derivation of the Approximate Model

Using the normalizations in the previous section and now treating the dimensionless parameters ϵ , $\epsilon \text{Re}^{(i)}$, and $1/\text{Ca}$ as small in comparison to unity, the leading order behavior of the nondimensional model equations will be derived. We determine the appropriate scalings of the fluid quantities resulting in the long-time validity of a maximal balance between buoyancy and viscous stress and, ultimately, the conduit equation (2.1). By our choice of scaling, the radial dynamics of the conduit fluid are captured, as well as the near interface dynamics in the exterior. It is important to consider that because the radial extent is large, the expressions derived below are valid only near the boundary and do not represent a uniform asymptotic expansion across large radial distances.

Note that the tilde notation for nondimensional variables will be dropped for the remainder of the manuscript, but all quantities are understood to be nondimensional.

2.4.1 Asymptotic Expansions and Scaling Ansatz

The velocities and pressures of the two fluids, as well as the dimensionless parameters, will now be scaled and expanded in powers of ϵ .

The dimensional equations were normalized so that vertical pressure gradients in the intrusive fluid balance with viscous forces due to the vertical flow, which implies $p^{(i)}, u_z^{(i)} = \mathcal{O}(1)$ and can

be expanded

$$p^{(i)} = p_0^{(i)} + \epsilon p_1^{(i)} + \cdots , \quad (2.38)$$

$$u_z^{(i)} = u_{z,0}^{(i)} + \epsilon u_{z,1}^{(i)} + \cdots . \quad (2.39)$$

This also requires that the inertial terms in the interior be neglected. From (2.28b), this means $\text{Re}^{(i)} \ll \epsilon^{-1}$. Note that this implies $\text{Re}^{(e)} \ll \rho^{(e)}/\rho^{(i)}$ so typically $\text{Re}^{(e)} \ll 1$. The length scales (2.18) were then chosen so that the uniform conduit radius R_0 is $\mathcal{O}(1)$ and the vertical dynamics occur on a longer spatial scale proportional to $\epsilon^{-1/2}$. The small slope condition therefore requires $R \ll \epsilon^{-1/2}$. We emphasize that the deviation of the conduit wall from uniformity can be very large.

In the uniform conduit, the intrusive modified pressure was balanced with the hydrostatic pressure of the exterior fluid, but the exterior modified pressure was negligible. In the present scaling, the extrusive pressure can be represented by

$$p^{(e)} = \epsilon \left(p_1^{(e)} + \epsilon p_2^{(e)} + \cdots \right) , \quad (2.40)$$

so that leading order hydrostatic balance, $p_h^{(e)} = P_0^{(e)}$, is preserved. Tangential shear stress due to the intrusive vertical velocity was balanced by an exterior vertical velocity with scale set by eq. (2.17) so that according to (2.39),

$$u_z^{(e)} = \epsilon \left(u_{z,0}^{(e)} + \epsilon u_{z,1}^{(e)} + \cdots \right) . \quad (2.41)$$

The use of miscible fluids renders the surface tension negligible, which by (2.37) means $1/\text{Ca} \ll 1$. Lastly, the amplitudes of the radial velocities are identified from (2.34) and expanded asymptotically as

$$u_r^{(i)} = \epsilon^{1/2} \left(u_{r,0}^{(i)} + \epsilon u_{r,1}^{(i)} + \cdots \right) , \quad (2.42)$$

$$u_r^{(e)} = \epsilon^{1/2} \left(u_{r,0}^{(e)} + \epsilon u_{r,1}^{(e)} + \cdots \right) . \quad (2.43)$$

The fluid quantities have now been scaled so that disturbances along the uniform conduit are captured by appealing only to the leading order, approximate governing equations. In previous derivations, the key physical assumption made was that the vertical wavelength of conduit perturbations was long in comparison with the radial amplitude. In our framework, this is captured by normalizing to the radial, conduit scale and then allowing slow variations in the vertical direction. The magnitude of the slope is proportional to the ratio of the intrusive radial velocity to vertical velocity, which is $\mathcal{O}(\epsilon^{1/2})$ and thus indeed small in our analysis.

2.4.2 Leading Order Solution

In the physical regime of validity of the rescaled fluid properties, the leading order nondimensional equations for the intrusive fluid are

$$\frac{1}{r} \frac{\partial}{\partial r} \left(r u_{r,0}^{(i)} \right) + \frac{\partial u_{z,0}^{(i)}}{\partial z} = 0 , \quad (2.44a)$$

$$\frac{\partial p_0^{(i)}}{\partial r} = 0 , \quad (2.44b)$$

$$\frac{\partial p_0^{(i)}}{\partial z} = \frac{1}{r} \frac{\partial}{\partial r} \left(r \frac{\partial u_{z,0}^{(i)}}{\partial r} \right) , \quad (2.44c)$$

and for the extrusive fluid

$$\frac{1}{r} \frac{\partial}{\partial r} \left(r u_{r,0}^{(e)} \right) = 0 , \quad (2.45a)$$

$$\frac{1}{r} \frac{\partial}{\partial r} \left(r \frac{\partial u_{r,0}^{(e)}}{\partial r} \right) - \frac{u_{r,0}^{(e)}}{r^2} = 0 , \quad (2.45b)$$

$$\frac{1}{r} \frac{\partial}{\partial r} \left(r \frac{\partial u_{z,0}^{(e)}}{\partial r} \right) = 0 . \quad (2.45c)$$

The axial boundary conditions at $r = 0$ (2.33) and the far-field conditions remain unchanged. Along the interface, the velocity continuity conditions (2.35) and kinematic condition (2.34) at

leading order are

$$u_{z,0}^{(i)} = 0 , \quad u_{r,0}^{(i)} = u_{r,0}^{(e)} = \frac{\partial R(z,t)}{\partial t} , \quad r = R(z,t) . \quad (2.46)$$

The interfacial force balance equations (2.37) simplify to

$$P_0^{(e)} - P_0^{(i)} = 2 \frac{\partial u_{r,0}^{(e)}}{\partial r} , \quad r = R(z,t) , \quad (2.47a)$$

$$\frac{\partial u_{z,0}^{(i)}}{\partial r} = \frac{\partial u_{z,0}^{(e)}}{\partial r} - \frac{\partial u_{r,0}^{(e)}}{\partial z} + 2 \frac{\partial R}{\partial z} \frac{\partial u_{r,0}^{(e)}}{\partial r} , \quad r = R(z,t) . \quad (2.47b)$$

In this form, analytical expressions for the fluid properties can be found. From (2.45a) and (2.45b), along with the boundary condition (2.46), the extrusive radial velocity is

$$u_{r,0}^{(e)} = \frac{\partial R(z,t)}{\partial t} \frac{R(z,t)}{r} , \quad (2.48)$$

hence exhibits algebraic decay. From our scaling of the modified pressure (2.40), the exterior absolute pressure is

$$P_0^{(e)} = - \frac{\rho^{(e)} z}{\rho^{(e)} - \rho^{(i)}} , \quad (2.49)$$

and because the interior pressure is independent of r (2.44b), the boundary condition (2.47) gives the form of the intrusive pressure to be

$$p_0^{(i)} = P_0^{(i)} + \frac{\rho^{(i)} z}{\rho^{(e)} - \rho^{(i)}} = \frac{2}{R(z,t)} \frac{\partial R(z,t)}{\partial t} - z . \quad (2.50)$$

Substituting (2.50) into (2.44c) and imposing the boundary conditions (2.33) and (2.46) yields

$$u_{z,0}^{(i)} = \frac{1}{4} \left[1 - \frac{\partial}{\partial z} \left(\frac{2}{R(z,t)} \frac{\partial R(z,t)}{\partial t} \right) \right] (R^2(z,t) - r^2) . \quad (2.51)$$

The dependence of $u_{r,0}^{(i)}$ on the interface can be derived from (2.44a), which can be rewritten

$$u_{r,0}^{(i)} = - \frac{1}{r} \frac{\partial}{\partial z} \int_0^r r' u_{z,0}^{(i)} dr' . \quad (2.52)$$

From this form, it is readily observed that by imposing the kinematic boundary condition (2.46), the resulting equation (2.52) is identical to the area conservation law (2.13). While this is not surprising because the conservation law was derived by the integral form of the continuity equation within the intrusive conduit, it shows that the multiple scales approach leads directly to the appropriate relationship between the dynamic interface and the fluid velocity field, without appealing to physical intuition. Solving (2.52) gives the explicit form of the intrusive, radial velocity to be

$$u_{r,0}^{(i)} = -\frac{1}{8r} \frac{\partial}{\partial z} \left\{ \left[1 - \frac{\partial}{\partial z} \left(\frac{2}{R(z,t)} \frac{\partial R(z,t)}{\partial t} \right) \right] \left(R^2(z,t) - \frac{r^2}{2} \right) r^2 \right\} . \quad (2.53)$$

The exterior vertical velocity can be solved according to (2.45c) along with the tangential shear stress balance condition (2.47b) to obtain

$$u_{z,0}^{(e)} = f(z,t) \ln r + g(z,t) , \quad (2.54)$$

where $f(z,t)$ satisfies

$$f(z,t) = 2 \frac{\partial}{\partial t} \left(R(z,t) \frac{\partial R(z,t)}{\partial z} \right) - \frac{1}{2} R^2(z,t) . \quad (2.55)$$

We note here that while $u_{r,0}^{(e)}$ decays as $r \rightarrow \infty$ and the pressure at leading order is hydrostatic as required by the far-field boundary condition, the vertical velocity $u_{z,0}^{(e)}$ does not decay. As discussed earlier, the leading order equations for the exterior fluid are valid only near the interface. It is a known phenomenon that there is no solution to the Stokes' flow equations, as considered here, in cylindrical coordinates which vanish at ∞ (cf. [9]). To satisfy this boundary condition, and to solve for the undetermined function $g(z,t)$, one must appeal to higher order terms, where inertial effects are incorporated. We do not consider this calculation here but will discuss the solution for $u_{z,0}^{(e)}$ when a radial boundary is present in §2.5.

Hence the perturbed problem has subtle differences from the uniform conduit problem. There

is now a pressure jump across the interface resulting from the unsteady injection rate. This is balanced by a viscous, normal stress from the exterior fluid. All leading order fluid quantities have been determined in terms of the radial profile of the conduit interface $R(z, t)$.

2.4.3 Reduction to the Conduit Equation

The fluid properties are now known at leading order, but it remains to find the leading order governing equation for the interfacial dynamics. This is done by appealing to the area conservation law (2.13) or, equivalently, by imposing the kinematic boundary condition (2.46) on the intrusive radial velocity expression (2.52). Integrating the vertical velocity expression (2.51) and relating the conduit radius to the area via $A(z, t) = \pi R^2(z, t)$, yields an expression for the volumetric flow rate $Q(z, t)$ within the conduit in terms of its area,

$$Q(z, t) = \frac{A^2}{8\pi} \left\{ 1 - \frac{\partial}{\partial z} \left(A^{-1} \frac{\partial A}{\partial t} \right) \right\} . \quad (2.56)$$

Rescaling the area so that $A' = A/8\pi$ and inserting (6.7) into the area conservation law, we are left with

$$\frac{\partial A'}{\partial t} + \frac{\partial}{\partial z} \left\{ A'^2 \left[1 - \frac{\partial}{\partial z} \left(A'^{-1} \frac{\partial A'}{\partial t} \right) \right] \right\} = 0 , \quad (2.57)$$

which is precisely the conduit equation (2.1) in standard form.

2.5 Robustness of the Conduit Equation

The benefit of the multiple scales approach to the derivation of eq. (2.1) is that the order of magnitude of higher order corrections and the relation between dimensionless parameters are elucidated. In particular, we are interested in criteria which indicate when previously neglected terms become important to the leading order interfacial dynamics. This section is devoted to exploring the effects of several assumptions made in § 2.4 and identifying approximate points of breakdown for the conduit equation. We also demonstrate the ability to derive information

about higher order corrections in special cases. In what follows, we determine the scalings such that all corrections to the conduit equation (2.1) are $\mathcal{O}(\epsilon)$.

2.5.1 Viscous, Higher Order Corrections

The equations solved in deriving the conduit equation (2.1) in § 2.4.2 were a special case of the Stokes' flow equations, in which the vertical dynamics occurred over a much longer length scale than the radial dynamics. A convenient analytical property of the axisymmetric Stokes' flow equations, is that one can rewrite the nondimensional equations in the form [86]

$$\epsilon \tilde{\nabla}^2 p^{(i,e)} = \frac{1}{r} \frac{\partial}{\partial r} \left(r \frac{\partial p^{(i,e)}}{\partial r} \right) + \epsilon \frac{\partial^2 p^{(i,e)}}{\partial z^2} = 0 \quad (2.58)$$

$$\tilde{\mathcal{L}}^2 \psi^{(i,e)} = 0, \quad \tilde{\mathcal{L}} = \epsilon \frac{\partial^2}{\partial z^2} + \frac{\partial^2}{\partial r^2} - \frac{1}{r} \frac{\partial}{\partial r} \quad (2.59)$$

where $\psi^{(i,e)}$ is the Stokes' stream function, which is related to the velocity components by

$$u_r^{(i,e)} = -\epsilon^{1/2} \frac{1}{r} \frac{\partial \psi^{(i,e)}}{\partial z}, \quad u_z^{(i,e)} = \frac{1}{r} \frac{\partial \psi^{(i,e)}}{\partial r}. \quad (2.60)$$

In the asymptotic formulation, the fluid pressures and velocities were expanded in asymptotic series and expressions for the leading order term in the expansion were found. It was unclear from the form of the equations, what would be the order of magnitude of the second term in the series, but expanding (2.58), (2.59), one can see that $p_1^{(i,e)} = \mathcal{O}(\epsilon p_0^{(i,e)})$ and $\mathbf{u}_1^{(i,e)} = \mathcal{O}(\epsilon \mathbf{u}_0^{(i,e)})$, provided the Stokes' regime is still valid. Otherwise, inertial effects require an alternative scaling. Because the conduit equation (2.1) was derived from the intrusive vertical velocity, this implies that viscous corrections to the conduit equation (2.1) will be of magnitude $\mathcal{O}(\epsilon)$.

2.5.2 Breakdown of Assumptions

A key physical assumption in deriving this model equation is the choice of characteristic scales about which the full governing equations were normalized. In choosing the length scales

(2.18) and imposing $\epsilon \ll 1$, we implicitly assumed, by dropping higher order effects, that the (dimensionless) radial dynamics occur such that $r \ll \epsilon^{-1/2}$. Specifically, if the perturbed conduit radius satisfies $\epsilon^{1/2}R(z, t) \ll 1$, then our assumptions of dominant balance along the interface are preserved, as well as the characteristic scalings chosen. However, when this condition is violated, our asymptotic construction fails.

A similar condition can be derived for the breakdown of the assumption to neglect inertial effects. From eq. (2.28b), if the interior Reynolds number satisfies $\text{Re}^{(i)} = \mathcal{O}(1)$, then inertial corrections to the conduit equation (2.1) will have magnitude ϵ . This condition is equivalent to the small slope condition, which can be seen by direct evaluation of (2.26). Hence violation of the small slope assumption coincides with the introduction of inertial effects to the viscous conduit.

Another key assumption made in deriving the conduit equation was to neglect surface tension effects. In the case of miscible fluids, this is reasonable, but the conduit equation is valid more generally, with surface tension effects entering the approximate model (2.1) at $\mathcal{O}(\epsilon)$, provided the capillary number satisfies $\text{Ca} = \mathcal{O}(\epsilon^{-1/2})$.

2.5.3 Dependence on an Outer Wall

Suppose that instead of considering the exterior dynamics on the infinite half-line, $r > 0$, with far-field boundary conditions, we confined the exterior fluid with an outer wall, say at $r = L_w \gg R_0$, and imposed a no-slip, no-penetration boundary condition, i.e. both components of the exterior velocity field are zero. The goal is to understand how the value of L_w couples into the approximate model. Assuming the same scalings as in § 2.4, the change comes in the solution to the exterior velocities. To prevent confusion with earlier work, we will use $\mathbf{v}^{(i,e)}$ to indicate velocities in this section. Using eq. (2.45b), and imposing the boundary conditions at the outer wall, the particular form of the radial velocity is now

$$v_{r,0}^{(e)} = \frac{R(z, t)}{R^2(z, t) - L_w^2} \frac{\partial R(z, t)}{\partial t} (r - L_w^2 r^{-1}) . \quad (2.61)$$

By eq. (2.54) and imposing the no-slip condition at L_w , the exterior vertical velocity is

$$v_{z,0}^{(e)} = f(z, t) \ln(r/L_w) , \quad (2.62)$$

where $f(z, t)$ is defined by eq. (2.55). Note that the inclusion of an exterior wall allows for the complete characterization of the leading order velocity field, while in the case of infinite radius, one would have to appeal to higher order to determine the free function $g(z, t)$. The exterior mass conservation equation (2.45a) is satisfied to leading order only if $L_w \gg 1$. To see how L_w incorporates into the approximate model for the interface, the normal stress match condition is modified to include the new form of the velocity, so that upon substitution, it becomes

$$v_{z,0}^{(i)} = \frac{1}{4} \left[1 + \frac{\partial}{\partial z} \left(\frac{2(R^2 + L_w^2)}{R(R^2 - L_w^2)} \frac{\partial R}{\partial t} \right) \right] (R^2 - r^2) . \quad (2.63)$$

Hence the flux in the presence of an outer wall, denoted $q(z, t)$, satisfies

$$q(z, t) = \frac{A^2}{8\pi} \left\{ 1 + \frac{\partial}{\partial z} \left[A^{-1} \frac{\partial A}{\partial t} \left(\frac{A + \pi L_w^2}{A - \pi L_w^2} \right) \right] \right\} , \quad (2.64)$$

which in the limit $L_w \rightarrow \infty$, is exactly (6.7). However, if $1 \ll L_w < \infty$, then a correction to (2.1) can be derived. Expanding about $1/L_w = 0$ yields a first-order correction of the form

$$q(z, t) \sim \frac{A^2}{8\pi} \left\{ 1 + \frac{\partial}{\partial z} \left[A^{-1} \frac{\partial A}{\partial t} \left(-1 - 2 \frac{A}{\pi L_w^2} \right) \right] \right\} , \quad (2.65)$$

which is an additional higher order dispersive term. Hence, the modified conduit equation becomes

$$\frac{\partial A'}{\partial t} + \frac{\partial}{\partial z} \left\{ A'^2 \left[1 - \frac{\partial}{\partial z} \left(A'^{-1} \frac{\partial A'}{\partial t} \right) - \frac{16}{L_w^2} \frac{\partial^2 A'}{\partial t \partial z} \right] \right\} = 0 . \quad (2.66)$$

Thus, so long as $L_w = \mathcal{O}(\epsilon^{-1/2})$, the conduit equation (2.1) is valid to $\mathcal{O}(\epsilon)$.

2.5.4 Symmetry Breaking – Inclined Conduit

Due to the small but nonnegligible velocities of the exterior fluid, it is unlikely that the axisymmetric assumption is entirely accurate for an experimentally generated conduit. Here we consider the point of breakdown due to an intrusive conduit fluid flowing at an angle ϕ relative to the vertical axis, with the biggest difference now being angular effects. The coordinate system is now rotated by the vertical angle ϕ so that z' is the longitudinal axis of the conduit while r' is the radial direction and θ' is the angular. The aim is to understand how the vertical angle introduces higher order corrections in the physical setting in which exterior, radial, viscous effects balance buoyant forcing within the conduit. Therefore, we will neglect the angular momentum equation in seeking an approximate criterion, but understand that this introduces an additional possibility for breakdown. In fact, via linear stability analysis, a critical tilt angle for gravitational instability of the intrusive fluid has been derived [121], but that study did not address the validity of the approximate model (2.1).

The nondimensional pressure in the new coordinates can be written $\hat{p}^{(i,e)} = \hat{P}^{(i,e)} - \hat{p}_h^{(i,e)}$, where the hydrostatic pressure is now

$$\hat{p}_h^{(i,e)} = \frac{\rho^{(i,e)}}{\rho^{(e)} - \rho^{(i)}} \left[-z' \cos \phi + \epsilon^{1/2} r' \sin \phi (\sin \theta' + \cos \theta') \right] . \quad (2.67)$$

By continuing to assume a leading order, hydrostatic balance on the exterior, the extrusive radial velocity is unchanged, but normal stress balance (2.47a) and the radial momentum equation (2.45b) yield the intrusive pressure to be

$$\hat{p}_0^{(i)} = -z' \cos \phi + 2 \left(R^{-1} \frac{\partial R}{\partial t} \right) + \epsilon^{1/2} R \sin \phi (\sin \theta' + \cos \theta') . \quad (2.68)$$

Then from (2.46), it is seen that the $\mathcal{O}(1 - \cos \phi)$ and $\mathcal{O}(\epsilon^{1/2} \sin \phi)$ corrections to the pressure will enter at the same magnitude into the intrusive, vertical velocity, and hence into the area conservation law in the same manner. We note, however, that for $\phi \ll 1$, we indeed recover the conduit equation. Then provided the angular momentum balance equation holds as well, the

conduit equation (2.1) is valid to $\mathcal{O}(\epsilon)$, as long as $\phi = \mathcal{O}(\epsilon^{1/2})$.

2.5.5 Summary

When higher order corrections are of size $\mathcal{O}(\epsilon)$, the conduit equation (2.1) is valid for times $t \ll 1/\epsilon$ and amplitudes $A \ll 1/\epsilon$, in the limit $\epsilon \rightarrow 0$. The required parameter constraints discussed in this section take the form:

- Weak inertial effects: $\text{Re}^{(i)} = \mathcal{O}(1)$,
- Weak surface tension: $\text{Ca} = \mathcal{O}(\epsilon^{-1/2})$,
- Weak boundary effects: $L_w = \mathcal{O}(\epsilon^{-1/2})$,
- Weak symmetry breaking: $\phi = \mathcal{O}(\epsilon^{1/2})$.

Since the normalized time scale of (2.1) is long, $T/\epsilon^{1/2}$, the *physical* time of validity for the conduit equation is for times much less than $T/\epsilon^{3/2}$.

2.6 Discussion and Conclusions

The key result of this perturbative approach to describing the dynamics of unsteady viscous conduits is that the conduit equation (2.1) is shown to be a robust model of truly dissipationless/dispersive hydrodynamics in the fully nonlinear regime, akin to a superfluid. While nonlinear, dispersive waves are prominent in the description of free fluid interfaces, for instance in shallow water [57] or in deep, stratified fluids [10, 84], one often has to restrict to the case of weak nonlinearity to derive an analytically tractable, dissipationless, approximate model. As we have demonstrated, the conduit equation (2.1) is valid in the long time, large amplitude regime, and additional physical effects must be considered for dissipation to be present in the model. Possible sources include the use of a visco-elastic, exterior fluid [39] or the presence of mass diffusion across the free interface.

In addition to presenting a careful derivation of the approximate model, this article provides the theoretical basis for the experimental study of nonlinear, dispersive waves in viscous fluid conduits. To consider the validity of our modeling assumptions and the ability of the approximate model to describe wave propagation in the system of interest, we compare with the data and scalings reported from laboratory simulations of solitary waves [83, 43]. The key experimental parameters are given in Table 2.1. In both sets of experiments, it is seen that the dimensionless parameter ϵ is indeed small relative to unity and that the Reynolds numbers satisfy the condition for weak inertial effects. Regarding the magnitude of the capillary number, all experiments were conducted with miscible fluids, so it is also safe to neglect the effects due to surface tension, but solubility introduces the possibility of mass diffusion. It was reported, however, that by using an intrusive fluid that is a water-diluted version of the exterior fluid, this effect is minimal.

We can also compare our discussion from § 2.5 with the point at which the authors reported deviation between theoretically predicted solitary wave speeds and the observations. The advantage of the multiple scales approach is that the magnitude of the small slope condition is now related directly to measurable quantities of the fluids, so it can be determined when this assumption fails. [83] reported underestimation of the wave amplitude by the approximate model at an amplitude $A \approx 13$, while [43] observed a similar underestimation when the amplitude of conduit waves exceeded $A \approx 10$. Checking the small slope condition $\epsilon^{1/2}R \ll 1$ in both cases (direct evaluation gives $\epsilon^{1/2}R \approx 4.5$ and 2, respectively) reveals that indeed the perturbed conduit radius exceeded the critical threshold and inertial effects would need to be incorporated to model the conduit dynamics accurately for larger amplitude. Hence our criteria accurately predict the point of breakdown of the conduit equation as an approximate description of the interface.

With the limits of validity of the theoretical model established, viscous fluid conduits provide an optimal setting for the precise, quantitative, experimental study of DSWs. Dispersively regularized shock waves have attracted a great deal of interest in recent years due to their observation in a range of physical systems, to include ultracold, dilute gas [23, 46], ion-acoustic

plasma [115], nonlinear optics [119, 20], and shallow water [19], but careful comparisons of theory and data are lacking. One difficulty is the long length and time scales required for the study of DSWs. These slowly modulated wavetrains are characterized by the presence of two scales. One is the $\mathcal{O}(1)$ scale of individual oscillations and the other is a long, slow scale of wave modulations $\mathcal{O}(1/\tilde{\epsilon})$, $\tilde{\epsilon} \ll 1$ (generally, $\tilde{\epsilon}$ is different from ϵ). However, images from previous experiments demonstrate that the experimental study of DSWs is accessible in viscous fluid conduits, e.g. Fig. 2.2. In this setting, a DSW is created by a step-like increase in the injection rate. This results in a larger trailing, vertically uniform conduit connected to a smaller, leading vertically uniform conduit, connected by a region of rapidly oscillating conduit waves, as depicted in Fig. 2.2. By use of an automated syringe pump, high resolution imaging and accurate measurement of the fluid densities and viscosities, precise quantitative experiments are possible. With the long-time validity of the conduit equation (2.1), measurements of characteristic DSW features – leading and trailing edge speeds and leading edge amplitude – can be compared with the analytical results of asymptotic modulation theory [125, 24], as developed for the conduit equation (2.1) by the present authors in [69].

The conduit equation is asymptotically equivalent to KdV in the small amplitude, long wavelength regime [122], but novel DSW regimes, e.g. backflow and DSW implosion, have been observed in large amplitude numerical simulations of (2.1). This work shows that these fully nonlinear, dispersive hydrodynamic features of the reduced model are experimentally accessible in viscous fluid conduits.

We thank Edward Shaughnessy and Karl Helfrich for many fruitful discussions. This work was supported by NSF Grant Nos. DGE-1252376 and DMS-1008973.

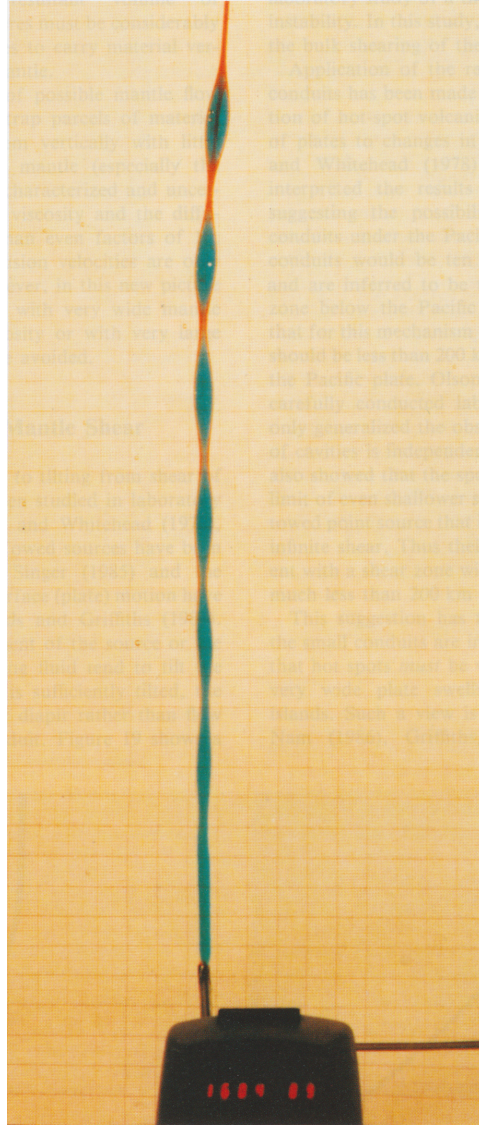


Figure 2.2: Figure 18 from the review article [123]. A vertically uniform, intrusive conduit is established with red fluid and then perturbed by a step-like increase in the injection with green fluid. One can see the formation of a DSW, with its characteristic periodic wavetrain slowly modulated over long space and time scales. An interesting observation is that the trailing fluid becomes trapped within individual waves of the DSW, surrounded by the leading fluid.

Table 2.1: Experimental parameters used to study solitary waves on viscous fluid conduits in previous literature. The parameters listed for [83] are reported for conduit fluid B only because the authors reported issues due to mass diffusion with conduit fluid A and for a single background flux value for which good agreement between theory and experiment was reported. All quantities are in cgs units with the same number of significant digits as in the original papers.

	Ref. [83]	Ref. [43]
$\rho^{(e)}$ (g/cm ³)	1.395	1.424
$\rho^{(i)}$ (g/cm ³)	1.075	1.257
$\mu^{(e)}$ (P)	110	45.0
$\mu^{(i)}$ (P)	0.074	0.40
L (cm)	0.012	0.021
U (cm/s)	0.58	0.187
T (s)	0.02	0.11
ϵ	6.7×10^{-4}	8.9×10^{-3}
$Re^{(i)}$	3.8	0.13
$Re^{(e)}$	3.3×10^{-3}	1.3×10^{-3}

Chapter 3

Dispersive Shock Waves in Viscously Deformable Media: Whitham-El Modulation Theory and Numerical Simulations

With the approximate model established in the previous chapter and an understanding of the physical system, we now wish to derive the key properties of solitary wave and DSW solutions for the conduit equation. It turns out that a generalization of the conduit equation, known as the magma equation, arises in the study of viscously deformable porous media. We choose to analyze the more general magma equation in this chapter, as this theoretical study was originally motivated by numerical simulations of the magma equation for step-like initial conditions and the open questions that resulted [108, 109]. In addition to identifying the key physical properties of conduit DSWs and solitary waves for comparison with experiments, we identify three distinct shock structures originating from single step initial data. One of these structures we term DSW implosion, which corresponds to the opening of a multiphase region within the single phase DSW

interior. This was the first observation of this behavior from a single step, and we provide a simple criterion for identifying its onset. We also identify four new admissibility criteria for applying DSW modulation theory to the magma equation. In the following chapter, we generalize these criteria to apply to any scalar, nonlinear dispersive PDE with hydrodynamic-type dispersionless limit. The contents of this chapter are based on the following publication [69]:

Lowman, N. K. and Hoefer, M. A. 2013 “Dispersive Shock Waves in Viscously Deformable Media,” *Journal of Fluid Mechanics* **718** 524–557.

3.1 Abstract

The viscously dominated, low Reynolds’ number dynamics of multi-phase, compacting media can lead to nonlinear, dissipationless/dispersive behavior when viewed appropriately. In these systems, nonlinear self-steepening competes with wave dispersion, giving rise to dispersive shock waves (DSWs). Example systems considered here include magma migration through the mantle as well as the buoyant ascent of a low density fluid through a viscously deformable conduit. These flows are modeled by a third-order, degenerate, dispersive, nonlinear wave equation for the porosity (magma volume fraction) or cross-sectional area, respectively. Whitham averaging theory for step initial conditions is used to compute analytical, closed form predictions for the DSW speeds and the leading edge amplitude in terms of the constitutive parameters and initial jump height. Novel physical behaviors are identified including backflow and DSW implosion for initial jumps sufficient to cause gradient catastrophe in the Whitham modulation equations. Theoretical predictions are shown to be in excellent agreement with long-time numerical simulations for the case of small to moderate amplitude DSWs. Verifiable criteria identifying the breakdown of this modulation theory in the large jump regime, applicable to a wide class of DSW problems, are presented.

3.2 Introduction

Shock waves in fluids typically arise as a balance between nonlinearity and dissipatively dominated processes, mediated by the second law of thermodynamics. An alternative balancing mechanism exists in approximately conservative media over time scales where dissipation is negligible. Nonlinearity and wave dispersion have been observed to lead to dynamically expanding, oscillatory dispersive shock waves (DSWs) in, for example, shallow water waves (known as undular bores) [19], ion-acoustic plasma (known as collisionless shock waves) [115, 116], superfluids [23, 46], and “optical fluids” [119, 20]. It is therefore counterintuitive that a fluid driven by viscous forces could lead to shock waves regularized by dispersion. In this work, precisely this scenario is investigated in viscously deformable media realized in magma transport and viscous fluid conduits.

The description of a low viscosity fluid flowing through a viscously deformable, compacting medium is a fundamental problem in Earth processes. Such systems include flow of oil through compacting sediment, subterranean percolation of groundwater through a fluidized bed, or the transport of magma through the partially molten upper mantle [75]. This type of flow also has implications for the buoyant ascent of a low density fluid through a deformable vertical conduit. Great interest by the broader scientific community has been taken in these systems since the derivation of a set of governing equations [75, 97, 98, 33]. The primitive equations treat the magma transport as flow of a low Reynolds’ number, incompressible fluid through a more viscous, permeable matrix that is allowed to compact and distend, modeled as a compressible fluid. This model, thought to be a reasonable representation of melt transport in the upper mantle, contrasts with standard porous media flow where the matrix is assumed fixed and the fluid is compressible.

Upon reduction to one-dimension (1D) and under a number of reasonable simplifications, the model equations reduce to the dimensionless, scalar magma equation

$$\phi_t + (\phi^n)_z - (\phi^n (\phi^{-m} \phi_t)_z)_z = 0, \quad (3.1)$$

where ϕ is the porosity, or volume fraction of the solid matrix occupied by the magma or melt, and (n, m) result from constitutive power laws relating the porosity to the matrix permeability and viscosity, respectively. [97, 98] concluded that the parameter space for realistic magma systems is $n \in [2, 5]$ and $m \in [0, 1]$, a claim which was later supported by re-derivation of the conservation equations via homogenization theory for different geometric configurations of the flow [104]. The flow through a deformable vertical conduit, magma migration via thermal plumes through the convecting mantle being one example, can also be written in the form (3.1) upon taking $(n, m) = (2, 1)$ with the interpretation of ϕ as the conduit's cross-sectional area [83].

The magma equation (3.1) is a conservation law for the porosity with nonlinear self-steepening due to buoyant advection through the surrounding matrix via the flux term ϕ^n and nonlocal dispersion due to compaction and distention of the matrix. Solitary traveling waves are special solutions to eq. (3.1) that have been studied in detail both theoretically [97, 98, 91, 7, 82, 105] and experimentally [99, 83, 43]. A natural generalization of single solitary waves to the case of a train of such structures can be realized as a DSW when the porosity exhibits a transition between two distinct states. The canonical dynamical problem of this type is the determination of the long time behavior of the dispersive Riemann problem, consisting of eq. (3.1) and the step initial data

$$\phi(z, 0) = \begin{cases} \phi_-, & z \in (-\infty, 0] \\ \phi_+, & z \in (0, \infty) \end{cases}. \quad (3.2)$$

Note that there is currently no rigorous proof of well-posedness for this particular initial value problem [103].

The dispersive Riemann problem was first studied in numerical simulations of eq. (3.1) in the $(n, m) = (3, 0)$ case by [108, 109]. Rather than smoothing the discontinuity and developing a classical shock front as in a dissipatively regularized system, the magma system responds to a jump by the generation of an expanding region of nonlinear oscillations with a solitary wave front and small amplitude tail, characteristic of DSWs (see figure 3.1). With the inclination to assume that steep gradients should be regularized by dissipative processes in this viscous system,

[109] used classical shock theory [126] to attempt to describe the behavior. In this work, we use a nonlinear wave averaging technique [24], referred to as Whitham averaging [125], in order to describe the dispersive regularization of step initial data of arbitrary height with $0 < \phi_+ < \phi_-$ for a range of constitutive parameters (n, m) . The resulting DSW's leading and trailing edge speeds are determined and the solitary wave front amplitude is resolved.

Traditional analysis of DSWs, first studied in the context of the Korteweg-de Vries (KdV) equation, asymptotically describes the expanding oscillatory region via the slow modulation of a rapidly oscillating, periodic traveling wave solution. These modulations are connected to the constant states of the exterior region by assuming the presence of linear dispersive waves at one edge of the DSW (amplitude $a \rightarrow 0$) and a solitary wave at the other (wavenumber $k \rightarrow 0$), as shown in figure 3.1 [125, 40]. In the case of KdV, the resulting system of three hyperbolic modulation equations can be solved due to the availability of Riemann invariants, which are, in general, not available for non-integrable systems such as the one considered here. An extension of simple wave led DSW Whitham modulation theory to non-integrable systems has been developed by [24], which has been successfully applied, for example, to fully nonlinear, shallow water undular bores [25, 26] and internal, two-fluid undular bores [29]. The modulation equations reduce exactly to a system of two hyperbolic equations at the leading and trailing edges where Riemann invariants are always available. Assuming the existence of an integral curve connecting trailing and leading edge states in the full system of modulation equations, one can calculate important physical DSW properties, namely the edge speeds, the solitary wave edge amplitude, and the trailing edge wavepacket wavenumber (see s_{\pm} , a_+ , and k_- in figure 3.1), with knowledge of only the reduced system at the leading and trailing edges. We implement this Whitham-El simple wave DSW theory for the magma dispersive Riemann problem, finding excellent agreement with full numerical simulations in the small to moderate jump regime. In the large jump regime, we identify novel DSW behavior including backflow (negative trailing edge speed, $s_- < 0$) and DSW implosion. The oscillatory region of the implosion is characterized by slowly modulated periodic waves bookending an interior region of wave interactions. This behavior

is associated with a change in sign of dispersion and gradient catastrophe in the Whitham modulation equations. To the best of our knowledge, this is the first example of breaking of the Whitham modulation equations for initial data of single step type, previous studies having focused on breaking for multistep initial data [37, 48, 2] or an initial jump in a modulated periodic wave’s parameters [51], resulting in quasi-periodic or multi-phase behavior. Including gradient catastrophe, we identify four verifiable criteria that can lead to the breakdown of the simple wave DSW theory, applicable to DSW construction in other dispersive media.

Application of DSW theory to solutions of the magma equation has been largely neglected in the previous literature. [28] considered the weakly nonlinear KdV reduction of the magma equation and generic properties of the small amplitude DSWs produced. [73] numerically integrated the full Whitham modulation equations for the “piston” problem with $(n, m) = (3, 0)$ incorporating a Dirichlet boundary condition rather than considering the general Riemann problem. Furthermore, key DSW physical parameters were not discussed in detail and neither backflow nor DSW implosion were observed. This work implements a general classification of weak to large amplitude DSW behavior in terms of the initial jump height and the constitutive parameters.

The presentation proceeds as follows. Section 3.3 describes the derivation of the magma equation from the full set of governing equations for both magma transport and viscous fluid conduits. Section 3.4 presents properties of the magma equation important to the application of Whitham theory. Section 3.5 implements Whitham theory to the problem at hand and its comparison with numerical simulations is undertaken in Section 3.6. Key physical consequences of solution structures are elucidated and influences of parameter variation are considered. Causes of breakdown in the analytical construction in the case of large jumps are identified. We conclude the manuscript with some discussion and future directions in Section 3.7.

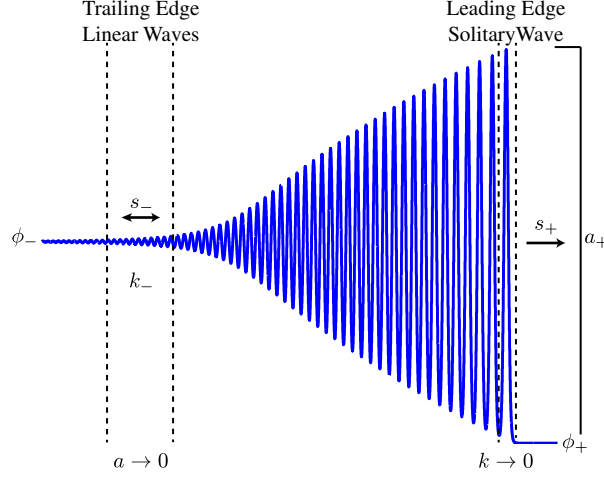


Figure 3.1: Example numerical solution of the dispersive Riemann problem for eq. (3.1). The solution to the initial step connects the external constant states ϕ_{\pm} to an inner oscillatory region with a solitary wave leading edge where the wavenumber $k \rightarrow 0$ and a packet of linear waves in the trailing edge where $a \rightarrow 0$. The salient physical properties of a magma DSW are the leading edge amplitude a_+ , trailing edge wavenumber k_- , the forward propagation speed of the solitary wave front s_+ , and the trailing edge speed s_- .

3.3 Governing Equations

In this section, we briefly summarize the origin of the magma equation (3.1) in the context of magma migration [75, 97, 98] and fluid conduit flow [83]. Our purpose is to put the dispersive equation in its physical context in terms of assumptions, parameters, and scalings.

3.3.1 Magma Geophysics

The equations governing flow of a viscous interpenetrating fluid through a viscously deformable medium were derived independently in the context of magma by [75, 97, 98, 33]. The system is a generalization of standard rigid body porous media flow but exhibits novel behavior. In the absence of phase transitions, buoyancy drives the predominant vertical advection of magma, the fluid melt, but the inclusion of dilation and compaction of the solid matrix introduces variability in the volume fraction occupied by the melt, which we will see transmits melt fluxes through the system as dispersive porosity waves. In the interest of providing physical intuition

for understanding the 1D magma equation, we now recall the formulation of McKenzie and describe the derivation of conservation equations for mass and momentum of the fluid melt and the solid matrix, and then reduce systematically to eq. (3.1). In what follows, variable, primed quantities are unscaled, often dimensional. Unprimed variable quantities are all scaled and nondimensional. Material parameters and scales are unprimed as well.

The governing equations are a coupled set of conservation laws for mass and momentum which describe the melt as an inviscid, incompressible fluid and the solid matrix as a viscously deformable fluid, written in terms of the porosity ϕ' (or volume fraction of melt). Interphase mass transfers are taken to be negligible so the coupling comes from McKenzie’s introduction of the interphase force \mathbf{I}' , a generalization of the standard D’Arcy’s law [96], which describes the rate of separation of the melt and matrix as proportional to the gradients of the lithostatic and fluid pressures. The leading proportionality term is chosen so that in the limit of a rigid matrix, D’Arcy’s Law is recovered. Upon substitution of the coupling term into the governing equations, the system reduces to the Stokes’ flow equations for the matrix in the “dry” limit, $\phi' \rightarrow 0$.

To simplify clearly to the 1D magma equation, it is convenient to write the governing equations as in [54], where the original McKenzie system is presented in a computationally amenable form. This follows from taking the solid and fluid densities to be distinct constants and then introducing a decomposition of the melt pressure $P' = P'_1 + \mathcal{P}' + P^{*'}'$ where $P'_1 = \rho_s g z'$ is the background lithostatic pressure, \mathcal{P}' is the pressure due to dilation and compaction of the matrix given by $\mathcal{P}' = (\zeta' - \frac{2}{3}\eta')\nabla \cdot \mathbf{v}'_s$, and $P^{*'}'$ encompasses the remaining pressure contributions primarily stemming from viscous shear stresses in the matrix. Note the introduction of the solid matrix velocity \mathbf{v}'_s , as well as the matrix shear and bulk viscosities η', ζ' , which arise due to matrix compressibility and depend on the porosity as described below. For nondimensionalization, we follow the scalings described in [108] (a similar reduction was performed in [97, 98, 7, 6]). This requires the introduction of the natural length scale of matrix compaction δ and the natural velocity scale of melt percolation w_0 proposed by [75], which for a background porosity ϕ_0 are

defined as

$$\delta = \sqrt{\frac{K'_0(\zeta'_0 + \frac{4}{3}\eta'_0)}{\mu'}}, \quad w_0 = K'_0 \frac{\Delta\rho g}{\phi_0 \mu} \quad (3.3)$$

where μ is the melt viscosity, $\Delta\rho = \rho_s - \rho_f$ is the difference between the solid and fluid densities, and K'_0 and $(\zeta'_0 + \frac{4}{3}\eta'_0)$ are the permeability and combined matrix viscosity at the background porosity ϕ_0 , respectively. [110] remarks that for practical geological problems, δ is on the order of $10^2 - 10^4$ m while w_0 takes on values of 1 - 100 m yr⁻¹, and the background porosity ϕ_0 of standard media is between $10^{-3} - 10^{-2}$. Using these as standard scales and after algebraic manipulation, the McKenzie system reduces to the non-dimensional form (unprimed variables) of the system presented in [54],

$$\frac{D\phi}{Dt} = (1 - \phi_0\phi) \frac{\mathcal{P}}{\xi}, \quad (3.4)$$

$$-\nabla \cdot K \nabla \mathcal{P} + \frac{\mathcal{P}}{\xi} = \nabla \cdot K [\nabla P^* + \hat{\mathbf{g}}], \quad (3.5)$$

$$\nabla \cdot \mathbf{v}_s = \phi_0 \frac{\mathcal{P}}{\xi}, \quad (3.6)$$

$$\nabla P^* = \nabla \cdot \eta (\nabla \mathbf{v}_s + \nabla \mathbf{v}_s^T) - \phi_0 \phi \hat{\mathbf{g}}, \quad (3.7)$$

where $\xi = \zeta - \frac{2}{3}\eta$ and $\hat{\mathbf{g}}$ is a unit vector in the direction of gravity. Neglecting terms $O(\phi_0)$, moving in the reference frame of the matrix, and introducing constitutive laws $K = \phi^n$ and $\xi = \phi^{-m}$ for the permeability and a combined matrix viscosity, the system (3.4)-(3.7) reduces to the dimensionless, 1D form for the vertical ascent of the fluid magma

$$\phi_t = \phi^m \mathcal{P}, \quad (3.8)$$

$$-(\phi^n \mathcal{P}_z)_z + \phi^m \mathcal{P} = -(\phi^n)_z. \quad (3.9)$$

After normalizing by the natural length and time scales (3.3), this system of equations conveniently has no coefficient dependence on adjustable parameters, which gives rise to a scaling symmetry discussed in Section 3.4.1. The constitutive power laws represent the expected effects

of changes in the matrix porosity on its permeability and combined viscosity, when the porosity is small. Both physical arguments, cf. [97, 98] and homogenization theory [104] have been used to argue that physically relevant values for the constitutive parameters (n, m) lie in the range $n \in [2, 5]$ and $m \in [0, 1]$ or at least in some subset of that range. Eliminating the compaction pressure from the above formulation, leads to the scalar magma equation (3.1) considered in this paper.

From the derivation, we observe that the time evolution of porosity in an interpenetrating magma flow system is controlled by a nonlinear advection term $(\phi^n)_z$ and a dispersive term $(\phi^n(\phi^{-m}\phi_t)_z)_z$. The nonlinearity enters the system via buoyant forcing of the melt, driven by the matrix permeability. Compaction and dilation of the matrix generate dispersive effects on the melt which for step-like initial data, result in porosity propagation in the form of an expanding region of porosity waves.

3.3.2 Viscous Fluid Conduits

An independent formulation of eq. (3.1) arises in the context of a conduit of buoyant fluid ascending through a viscously deformable pipe. For magma, this represents an alternative transport regime to the interpenetrating flow described above, most closely related to flow up the neck of a thermal plume in the mantle.

Following [83], the buoyant fluid rises along a vertical conduit of infinite length with circular cross-sections, embedded in a more viscous matrix fluid. The matrix with density ρ_M , viscosity η_M and the fluid conduit with density ρ_f , viscosity η_f , must satisfy

$$\rho_M > \rho_f \quad \eta_M \gg \eta_f . \quad (3.10)$$

The circular cross-sectional area is $A' = \pi R'^2$, where the conduit radius R' is allowed to vary. The Reynolds' number and slope of the conduit wall (i.e. the ratio of conduit deformation to wavelength) are assumed to be small and mass and heat diffusion are negligible.

With this set-up, the conduit flux Q' can be related to the cross-sectional area A' via Poiseuille's Law for pipe flow of a Newtonian fluid (recall that primed variables are dimensional)

$$Q' = -\frac{A'^2}{8\pi\eta_f} \frac{\partial P'}{\partial z'} \quad (3.11)$$

where P is the nonhydrostatic pressure of the fluid. Conservation of mass manifests as

$$\frac{\partial A'}{\partial t} + \frac{\partial Q'}{\partial z} = 0. \quad (3.12)$$

To derive an expression for P' , we balance radial forces at the conduit wall. Using the small-slope approximation, we assume radial pressure forces in the conduit dominate viscous effects. In the matrix, the radial components of the normal force dominate viscous stresses. Setting the radial forces of the matrix and conduit equal at the boundary and making the appropriate small-slope approximations, yields an expression for the nonhydrostatic pressure

$$P' = -\Delta\rho g z' + \frac{\eta_M}{A'} \frac{\partial A'}{\partial t'}, \quad (3.13)$$

for $\Delta\rho = \rho_M - \rho_f$. Substitution of (3.13) back into (3.11), utilizing (3.12) for simplification and nondimensionalizing about a background, steady state, vertically uniform Poiseuille flow

$$Q_0 = \frac{\Delta\rho g}{8\pi\eta_f} A_0^2,$$

with length and time scales L and T

$$L = \left(\frac{\eta_M A_0}{8\pi\eta_f} \right)^{\frac{1}{2}}, \quad T = \frac{1}{\Delta\rho g} \left(\frac{8\pi\eta_f\eta_M}{A_0} \right)^{\frac{1}{2}},$$

gives the non-dimensional equations

$$Q = A^2 \left[1 + \frac{\partial}{\partial z} \left(\frac{1}{A} \frac{\partial Q}{\partial z} \right) \right],$$

$$-\frac{\partial A}{\partial t} = \frac{\partial Q}{\partial z}.$$

which are eqs. (3.8) and (3.9) for the case $(n, m) = (2, 1)$.

3.4 Properties of the Magma Equation

In this section we recall several results that will be important for our studies of magma DSWs. It is interesting to note that for the pairs $(n, m) = (-1, 0)$ and $(n, m) = (\frac{1}{2}, \frac{1}{2})$ the magma equation has been shown to be completely integrable, but for other rational values of (n, m) it is believed to be non-integrable by the Painleve ODE test [42]. We will primarily be concerned with the physically relevant non-integrable range $m \in [0, 1], n \in [2, 5]$, but many of the results are generalized to a much wider range of values.

3.4.1 Linear Dispersion Relation and Scaling

Linearizing eq. (3.1) about a uniform background porosity Φ and seeking a harmonic solution with real-valued wavenumber k , and frequency ω_0 , we write ϕ as

$$\phi(z, t) \approx \Phi + \nu \left(e^{i(kz - \omega_0 t)} + \text{c.c.} \right), \quad |\nu| \ll 1, \quad (3.14)$$

where c.c. denotes the complex conjugate. Substitution into eq. (3.1) yields the linear dispersion relation

$$\omega_0(k, \Phi) = \frac{n\Phi^{n-1}k}{1 + \Phi^{n-m}k^2}. \quad (3.15)$$

Taking a partial derivative in k gives the group velocity

$$(\omega_0(k, \Phi))_k = \frac{n\Phi^{n-1}(1 - \Phi^{n-m}k^2)}{(1 + \Phi^{n-m}k^2)^2}. \quad (3.16)$$

Note that although the phase velocity $\frac{\omega_0}{k}$ is strictly positive, the group velocity (3.16) can take on either sign, with a change in sign occurring when $k^2 = \Phi^{m-n}$. Taking a second partial

derivative of eq. (3.15) with respect to k gives

$$(\omega_0(k, \Phi))_{kk} = \frac{-2nk\Phi^{2n-1-m}(3 - \Phi^{n-m}k^2)}{(1 + \Phi^{n-m}k^2)^3} . \quad (3.17)$$

Introducing the sign of dispersion, we say the system has positive dispersion if $(\omega_0(k, \Phi))_{kk} > 0$ so that the group velocity is larger for shorter waves. Similarly, negative dispersion is defined as $(\omega_0(k, \Phi))_{kk} < 0$. From eq. (3.17), the sign of dispersion is negative for long waves but switches to positive when $k^2 = 3\Phi^{m-n}$. These distinguished wavenumbers, the zeros of the group velocity and sign of dispersion, have physical ramifications on magma DSWs that will be elucidated later.

The magma equation also possesses a scaling symmetry. It is invariant under the change of variables

$$\phi' = \Phi\phi, \quad z' = \Phi^{\frac{n-m}{2}}z, \quad t' = \Phi^{\frac{1}{2}(2-n-m)}t, \quad \Phi > 0 . \quad (3.18)$$

This allows us to normalize the background porosity to one without loss of generality, which we will do in Section 3.5.

3.4.2 Long Wavelength Regime

In the weakly nonlinear, long wavelength regime, the magma equation reduces to the integrable KdV equation [?, 113, 28] . To obtain KdV we enter a moving coordinate system with the linear wave speed n and introduce the “slow” scaled variables $\zeta = \epsilon^{1/2}(z - nt)$, $\tau = \epsilon^{3/2}t$, and $\phi(z, t) = 1 + \epsilon u(z, t)$ to the magma equation. Assuming $|\epsilon| \ll 1$, a standard asymptotic calculation results in

$$u_\tau + n(n-1)uu_\zeta + nu_{\zeta\zeta} = 0, \quad (3.19)$$

which has no dependence on the parameter m . What this implies physically is that dispersion in the small amplitude, weakly nonlinear regime is dominated by matrix compaction and dilation. Nonlinear dispersive effects resulting from matrix viscosity are negligible. The original construction of a DSW was undertaken for KdV by [40]. In Section 3.5, we will compare the

results of KdV DSW theory with our results for magma DSWs.

3.4.3 Nonlinear Periodic Traveling Wave Solutions

The well-studied solitary waves of eq. (3.1) are a limiting case of more general periodic traveling wave solutions. To apply Whitham theory to the magma equation, it is necessary to derive the periodic traveling wave solution to eq. (3.1), which forms the basis for nonlinear wave modulation. In the special case $(n, m) = (3, 0)$, [73] obtained an implicit relation for ϕ in terms of elliptic functions, and for $(n, m) = (2, 1)$, the equation was derived in integral form by [83]. Here we consider the full physical range of the constitutive parameters.

We seek a solution of the form $\phi(z, t) = \phi(\theta)$, where $\theta = z - ct$ for wave velocity c (c is related to the wave frequency ω and the wavenumber k by the relation $\omega = ck$), such that $\phi(\theta) = \phi(\theta + L)$ with wavelength L . Inserting this ansatz into eq. (3.1) and integrating once yields

$$c(\phi^{-m}\phi')' = A\phi^{-n} + c\phi^{1-n} - 1, \quad (3.20)$$

for integration constant A and $'$ indicating a derivative with respect to θ . Observing

$$c(\phi^{-m}\phi')' = c \left(\frac{1}{2}\phi^m \right) \left[\frac{d}{d\phi} (\phi^{-2m}(\phi')^2) \right],$$

enables us to integrate with respect to ϕ and find for $m \neq 1$ and $n + m \neq 2$

$$(\phi')^2 = \frac{2}{2-m-n}\phi^{m-n+2} - \frac{2}{c(1-m)}\phi^{m+1} - \frac{2A}{c(1-m-n)}\phi^{m-n+1} - \frac{2B}{c}\phi^{2m}, \quad (3.21)$$

with a second integration constant B .

For $n + m = 2$, which for our purposes necessarily implies $n = 2$ and $m = 0$, we integrate eq. (3.20) to

$$(\phi')^2 = 2 \ln \phi - \frac{2A}{c}\phi^{-1} - \frac{2}{c}\phi + \frac{2B}{c}. \quad (3.22)$$

For the case $m = 1$, $n \in [2, 5]$, eq. (3.20) integrates to

$$(\phi')^2 = -\frac{2}{c}\phi^2 \ln \phi + \frac{2A}{cn}\phi^{2-n} + \frac{2}{1-n}\phi^{3-n} + \frac{2B}{c}\phi^2. \quad (3.23)$$

Equations (3.21), (3.22), and (3.23) can be written in the general form $(\phi')^2 = g(\phi)$, where $g(\phi)$ is the potential function. Periodic solutions exist when $g(\phi)$ has three real, positive roots such that $0 < \phi_1 < \phi_2 < \phi_3$. In this case, the potential function can be rewritten

$$(\phi')^2 = g(\phi) = (\phi_1 - \phi)(\phi_2 - \phi)(\phi_3 - \phi)r^2(\phi) \quad (3.24)$$

where $r(\phi)$ is some smooth function and $r(\phi) \neq 0$ for $\phi \in (0, \phi_3)$. The sign is chosen so that $(\phi')^2 \xrightarrow{\phi \rightarrow \infty} -\infty$ for $c > 0$ as in each of the equations (3.21), (3.22), and (3.23). We verify that $c > 0$ because in the linear wave limit when $\phi_2 \rightarrow \phi_3$, $c = \frac{\omega_0}{k}$ which is positive from eq. (3.15). Similarly from solitary wave derivations (3.28), noting that $A > 1$, the speed is positive. From eqs. (3.21), (3.22), (3.23) and the fact that c depends continuously on the roots ϕ_1, ϕ_2, ϕ_3 , the only way for c to pass from positive to negative would be for $\phi \equiv 0$, else the potential function is singular, and in neither case does this yield a non-trivial periodic traveling wave solution. Thus the wave speed c must be strictly positive.

We also confirm that the potential functions in equations (3.21), (3.22), and (3.23) have no more than three positive roots in the physically relevant range of the constitutive parameters. First consider the case of integer n, m so that all exponents are integers. From Descartes' Rule of Signs, polynomials with real coefficients and terms ordered by increasing degree have a number of roots at most the number of sign changes in the coefficients. Hence, the four-term polynomial expression (3.21) has at most three positive roots as we assumed. For eq. (3.22), taking a derivative of $g(\phi)$ yields a three-term polynomial, which thus has at most two positive roots. From the Mean Value Theorem, this means (3.22) has no more than three positive roots. Eq. (3.23) follows in a similar manner, upon noting that one can factor out ϕ^2 so that the positive real roots are unchanged. Now relax the assumption that the constitutive parameters

take on integer values and suppose they can take on any rational value so that eq. (3.21) has rational exponents $\{y_1, y_2, y_3, y_4\}$ with least common multiple y . Then let $\phi = \psi^y$. It follows that $g(\phi)$ has the same number roots as $g(\psi^y)$, the latter now a four-term polynomial in ψ with integer exponents. As above, this may have at most three positive roots. A similar argument follows for eqs. (3.22), (3.23). The case of irrational n, m follows from continuity and density of the rationals in the real line. This gives an upper bound on the number of positive roots, which must be either one or three. We will consider only the cases where the particular parameters give exactly three positive roots.

One can see from eq. (3.24) that there is a map between the parameters A, B, c and the roots ϕ_1, ϕ_2, ϕ_3 so the periodic traveling wave solution can be determined by use of either set of variables. There is further an additional set of “physical” variables which we will use here. They are the periodic wave amplitude a

$$a = \phi_3 - \phi_2, \quad (3.25)$$

the wavenumber $k = \frac{2\pi}{L}$, which we express

$$k = \frac{2\pi}{L} = \pi \left(\int_{\phi_2}^{\phi_3} \frac{1}{\sqrt{g(\phi)}} d\phi \right)^{-1}, \quad (3.26)$$

and the wavelength-averaged porosity $\bar{\phi}$,

$$\bar{\phi} = \frac{2}{L} \int_{\phi_2}^{\phi_3} \frac{\phi}{\sqrt{g(\phi)}} d\phi. \quad (3.27)$$

The three parameter family of periodic waves will be parameterized by either (ϕ_1, ϕ_2, ϕ_3) or $(a, k, \bar{\phi})$. Invertibility of the map between these two parameter families is difficult to verify in general. However, in the limiting case $\phi_2 \rightarrow \phi_3$, we can express the physical variables in the following form at leading order:

$$a = 0, \quad \bar{\phi} = \phi_2, \quad k = \frac{r(\phi_2)\pi}{2} (\phi_2 - \phi_1)^{\frac{1}{2}}, \quad \phi_1 < \phi_2.$$

Hence, the determinant of the Jacobian of the transformation is $\partial k / \partial \phi_1 \neq 0$. A similar argument holds for the solitary wave limiting case using conjugate variables which will be introduced in Section 3.5.3. Since invertibility holds in the limiting cases, we make the additional assumption that it holds in general. Figure 3.2 shows a plot of $g(\phi)$ for $(n, m) = (2, 1)$, with the particular wave parameters $a = 0.6$, $\bar{\phi} = 1$, $k \approx 0.29$. From the example in figure 3.2, we observe that the periodic wave takes its values on the bounded, positive portion of $g(\phi)$ with $\phi_2 \leq \phi \leq \phi_3$.

The solitary wave solution of the magma equation occurs in the limit $\phi_2 \rightarrow \phi_1$. To derive the magma solitary wave, we impose the conditions on the potential function $g(\Phi) = 0$, $g(A) = 0$, $g'(\Phi) = 0$ for a solitary wave of height A which propagates on a positive background value Φ . Utilizing these conditions on the background state $\Phi = 1$ yields a solitary wave amplitude-speed relation $c(A)$ derived in [82] for n, m in the physical range

$$\begin{cases} c(A) = \frac{A^2 - 2A + 1}{A \ln A - A + 1}, & \text{if } m = 0, n = 2, \\ c(A) = \frac{(n-1)(nA^n \ln A - A^n + 1)}{A^n - nA + n - 1}, & \text{if } m = 1, \\ c(A) = \frac{(n+m-2)[nA^{n+m-1} - (n+m-1)A^n + m-1]}{(m-1)[A^{n+m-1} - (n+m-1)A + n+m-2]}, & \text{otherwise} \end{cases} \quad (3.28)$$

3.4.4 Conservation Laws

Another feature of the magma equation necessary for the application of DSW modulation theory is the existence of at least two conservation laws. [41] found two independent conservation laws for the magma equation given arbitrary values for the parameters (n, m) . While there are additional conservation laws for particular values of (n, m) , these lie outside the physically relevant range and will not be addressed. The first conservation law is the magma equation itself written in conservative form. The second conservation law does not have a clear physical meaning as it does not correspond to a momentum or an energy. It also possesses singular terms in the dry limit $\phi \rightarrow 0$, but this is not a problem in the positive porosity regime considered here.

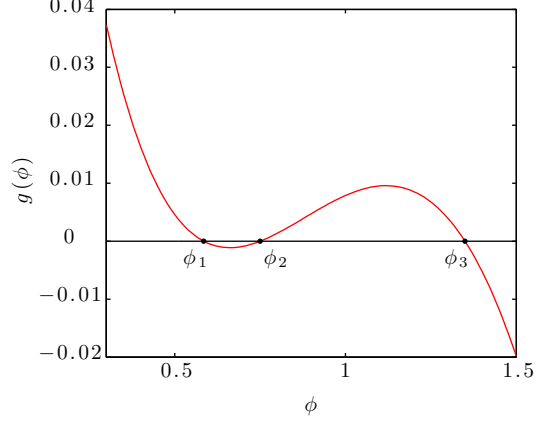


Figure 3.2: Plot of $(\phi')^2 = g(\phi)$, $(n, m) = (2, 1)$. The bounded, periodic solution lies between the roots ϕ_2 and ϕ_3 . The roots correspond to a particular choice of the physical wave parameters $a = 0.6$, $k \approx 0.29$, and $\bar{\phi} = 1$.

In conservative form, the conservation laws for the physically relevant parameter values are

$$\phi_t + (\phi^n(1 - \phi^{-m}\phi_t)_z)_z = 0 \quad (3.29)$$

and

$$\left\{ \begin{array}{ll} \left(-\frac{1}{2}\phi_z^2 + \ln \phi \right)_t + (-\phi\phi_{tz} + 2\phi)_z = 0, & \text{if } (n, m) = (0, 2) \\ \left(-\frac{n}{2}\phi^{-2}\phi_z^2 + \frac{\phi^{1-n} - 1}{1-n} \right)_t + (\phi^{-2}\phi_z\phi_t - \phi^{-1}\phi_{tz} + n \ln \phi)_z = 0, & \text{if } m = 1 \\ \left(\frac{1-m-n}{2}\phi^{-2m}\phi_z^2 + \frac{1}{2-n-m}(\phi^{2-n-m} - 1) \right)_t + \\ \left(m\phi^{-2m}\phi_z\phi_t - \phi^{1-2m}\phi_{tz} + \frac{n}{1-m}\phi^{1-m} \right)_z = 0, & \text{otherwise.} \end{array} \right. \quad (3.30)$$

3.5 Resolution of an Initial Discontinuity

A canonical problem of fundamental physical interest in nonlinear media is the evolution of an initial discontinuity. In the case of an interpenetrating magma flow, one can imagine magma

flowing from a chamber of uniform porosity into an overlying region of lower porosity. We study DSWs arising from this general set-up.

Consider the magma equation (3.1) given initial data (3.2) with the requirement $0 < \phi_+ < \phi_-$, which ensures singularity formation in the dispersionless limit $\phi_t + (\phi^n)_z = 0$ (gradient catastrophe). This is a dispersive Riemann problem. From DSW theory, a discontinuity in a dissipationless, dispersively regularized hyperbolic system will result in smooth upstream and downstream states connected by an expanding, rapidly oscillating region of rank-ordered, nonlinear waves. In the negative dispersion regime, this region is characterized by the formation of a solitary wave at the right edge and a linear wave packet at the left. Our goal in this section is to derive analytical predictions for the speeds at which the edges propagate and the height of the leading edge solitary wave.

Following the general construction of [24], which extends the work of [125] and then [40] to non-integrable systems, we will assume that the spatial domain can be split into three characteristic subdomains, $(-\infty, z_1(t))$, $[z_1(t), z_2(t)]$, and $(z_2(t), \infty)$, where $z_1(t) \leq z_2(t)$, for all $t > 0$. We formally introduce the slow variables $Z = \epsilon z$ and $T = \epsilon t$, where $0 < \epsilon \ll 1$, which is equivalent to considering $t \gg 1$ when $T = O(1)$. For the analysis, we use the slow variables Z, T to describe the modulations of the traveling wave. For the numerics, we consider $t \gg 1$ and do not rescale. Inside the dispersive shock region $z \in [z_1(t), z_2(t)]$, the solution is assumed to be described by slow modulations of the nonlinear, single phase, periodic traveling wave solution, i.e. a modulated one-phase region (the use of phase here describes the phase of the wave, not to be confused with the physical phase of the flow, e.g. melt or matrix). The modulation equations are a system of quasi-linear, first-order PDE formed by averaging over the two conservation laws augmented with the conservation of waves equation. This allows for the description of the DSW in terms of the three slowly varying, physical wave variables: the wavenumber k (3.26), the average porosity $\bar{\phi}$ (3.27), and the periodic wave amplitude a (3.25). Outside the dispersive shock, the dynamics are slowly varying so the solution is assumed to be governed by the dispersionless limit of the full equation which we call the zero-phase equation.

The dynamic boundaries between the zero- and one-phase regions are determined by employing the Gurevich-Pitaevskii matching conditions [40]. The behavior of the modulation system near the boundaries allows for a reduction of the modulation system of three quasilinear PDE to only two, thus locally reducing the complexity of the problem. For a simple wave solution, the limiting modulation systems can be integrated uniquely along an associated characteristic with initial data coming from the behavior at the opposite edge.

This construction relies on several assumptions about the mathematical structure of the magma equation and its modulation equations. From our discussion in Section 3.4, it is immediate that we have a real linear dispersion relation with hyperbolic dispersionless limit (seen formally by substituting the slow variables defined above and taking only the leading order equation). The two conservation laws given in equations (3.29) and (3.30) and the existence of a nonlinear periodic traveling wave with harmonic and solitary wave limits round out the basic requirements. Beyond these, we must satisfy additional constraints on the modulation system. Its three characteristics are assumed real and distinct so that the modulation equations are strictly hyperbolic and modulationally stable. The final requirement is the ability to connect the edge states by a simple wave. For this, the two states are connected by an integral curve associated with only one characteristic family. More will be said about this condition in the following discussion. We now supply the details of the application of El's method to the dispersive Riemann problem for the magma equation.

3.5.1 Application of El's method

To “fit” a modulated dispersive shock solution, we consider first the solution within the DSW, $z \in [z_1(t), z_2(t)]$. In this region, the solution is described locally by its nonlinear periodic traveling wave solution, parameterized by its three roots ϕ_1, ϕ_2, ϕ_3 , which vary slowly, depending on Z, T . Variations in the periodic traveling wave solution are governed by averaging over the system of conservation equations (3.29) and (3.30), along with an additional modulation equation known

as conservation of waves,

$$k_T + \omega_Z = 0, \quad (3.31)$$

where k is the wavenumber and ω is the nonlinear wave frequency [125]. Recalling the wavenumber k (3.26), we define the wavelength average of a generic smooth function $F(\phi)$ to be

$$\overline{F(\phi)} = \frac{k}{\pi} \int_{\phi_2}^{\phi_3} \frac{F(\phi)}{\sqrt{g(\phi)}} d\phi. \quad (3.32)$$

It is convenient here to use the nonlinear wave parameterization in terms of the three roots of $g(\phi)$. Later we will use the physical wave variables $a, k, \bar{\phi}$.

We now seek moving boundary conditions for $z_1(t)$ and $z_2(t)$ where the modulation solution is matched to the dispersionless limit. For the magma equation, the dispersionless limit is the zero-phase equation

$$\tilde{\phi}_T + n\tilde{\phi}^{n-1}\tilde{\phi}_Z = 0. \quad (3.33)$$

The GP boundary conditions [40] include the matching of the average value of the porosity to the dispersionless solution $\bar{\phi} \rightarrow \tilde{\phi}$, as well as a condition on the amplitude and wavenumber. Recalling figure 3.1, at the trailing edge, the wave amplitude vanishes. At the leading edge, the leading wave is assumed to take the form of a solitary wave and thus the wavenumber decays to zero. This could also be stated in terms of the roots of the potential function, as we saw in Section 3.4.3 where the diminishing amplitude limit corresponds to $\phi_2 \rightarrow \phi_3$ and the solitary wave limit to $\phi_2 \rightarrow \phi_1$. This implies that the boundary conditions align with double roots of the potential function. This orientation of the DSW with a rightmost solitary wave and a leftmost linear wave packet is expected for systems with negative dispersion, as is the case here, for at least small jumps [24]. These conditions result in the following moving boundary conditions for

an initial discontinuity:

$$z = z_1(t) : \quad \bar{\phi} = \phi_-, \quad a = 0, \quad \phi_2 \rightarrow \phi_3, \quad (3.34)$$

$$z = z_2(t) : \quad \bar{\phi} = \phi_+, \quad k = 0, \quad \phi_2 \rightarrow \phi_1. \quad (3.35)$$

In the $a \rightarrow 0$ and $k \rightarrow 0$ limits, one can show that $\overline{F(\phi)} = F(\bar{\phi})$. This is a fundamental mathematical property of averaging that allows for the Whitham system of three modulation equations to be reduced exactly to a system of two equations at the leading and trailing edges $z_1(t), z_2(t)$. An important note is that in the limit of vanishing amplitude, the nonlinear wave frequency $\omega = \omega(k, \bar{\phi}, a)$ becomes the linear dispersion relation $\omega_0(k, \bar{\phi}) = \omega(k, \bar{\phi}, 0)$ from eq. (3.15) which has no dependence on the amplitude. The exact reduction of the full modulation system to two PDE enables the construction of a self-similar simple wave solution. This simple wave of each boundary system is directly related to the simple wave associated with the second characteristic family of the full Whitham modulation system via the integral curve connecting the left state $(\phi_-, k_-, 0)$ to the right state $(\phi_+, 0, a_+)$. The goal is to determine k_- and a_+ and evaluate the characteristic speeds at the edges. Given ϕ_- and ϕ_+ , this construction provides the four key physical properties of the magma DSW as in figure 3.1. In the next two sections, we implement this method.

3.5.2 Determination of the Trailing Edge Speed

To determine the trailing edge speed of the DSW, we consider the above modulation system in a neighborhood of $z_1(t)$, where implementation of the boundary conditions yields the reduced limiting system

$$\bar{\phi}_T + (\bar{\phi}^n)_Z = 0, \quad (3.36)$$

$$k_T + (\omega_0)_Z = 0. \quad (3.37)$$

In characteristic form, the above system reduces to

$$-(\omega_0)_{\bar{\phi}} \frac{d\bar{\phi}}{dT} + (n\bar{\phi}^{n-1} - (\omega_0)_k) \frac{dk}{dT} = 0 \quad (3.38)$$

along the characteristic curve $\frac{dZ}{dT} = (\omega_0)_k$. The characteristic speed is the linear wave group velocity (3.16) but here with $\Phi \rightarrow \bar{\phi}$. To determine the linear wave speed, we integrate eq. (3.38) along the characteristic by introducing $k = k(\bar{\phi})$. Integrating from the leading edge solitary wave where the wavenumber vanishes, i.e. $k(\phi_+) = 0$, back across the DSW to the trailing edge determines the linear wavenumber k_- . Put another way, we connect states of our modulation system at the trailing edge $(k, \bar{\phi}) = (k_-, \phi_-)$ to the leading edge in the $a = 0$ plane $(k, \bar{\phi}) = (0, \phi_+)$, by assuming k varies in only one characteristic family. This is our simple wave assumption. To determine the speed, we evaluate $s_- = (\omega_0)_k$ at (k_-, ϕ_-) . The fact that we can restrict to the $a = 0$ plane follows from the assumed existence of an integral curve for the full Whitham modulation system and the GP matching conditions at the solitary wave edge, which are independent of a . Recalling the symmetry (3.18), without loss of generality, we restrict to the case

$$\phi(z, 0) = \begin{cases} 1, & z \in (-\infty, 0] \\ \phi_+, & z \in (0, \infty), \end{cases} \quad (3.39)$$

where $\phi_+ \in (0, 1)$. From the physical derivation, eq. (3.1) has already been non-dimensionalized on a background porosity scale so it is natural to normalize the upstream flow to unity in the dimensionless problem. Restriction of $\phi_+ \in (0, 1)$ results from physical interest in the problem of vertical flow from a magma chamber into a dryer region above, but one through which magma may still flow.

To determine the linear edge wavenumber k_- , it is necessary to solve the ordinary differential equation (ODE) initial value problem (IVP) resulting from the simple wave assumption $k = k(\bar{\phi})$

in eq. (3.38)

$$\frac{dk}{d\bar{\phi}} = \frac{(\omega_0)_{\bar{\phi}}}{n\bar{\phi}^{n-1} - (\omega_0)_k} = \frac{k [n-1 - (1+m)k^2\bar{\phi}^{n-m}]}{\bar{\phi} [(1 + \bar{\phi}^{n-m}k^2)^2 - (1 - \bar{\phi}^{n-m}k^2)]}, \quad k(\phi_+) = 0. \quad (3.40)$$

To find an integral of (3.40), it is convenient to use the change of variables

$$\alpha = \frac{\omega_0}{c(\bar{\phi})k}, \quad c(\bar{\phi}) = n\bar{\phi}^{n-1}, \quad (3.41)$$

which, upon substitution, is

$$\alpha = \frac{1}{1 + \bar{\phi}^{n-m}k^2}. \quad (3.42)$$

The IVP (3.40) therefore becomes

$$\frac{d\alpha}{d\bar{\phi}} = -\frac{[(m+n-2)\alpha + n-m]\alpha}{\bar{\phi}(2\alpha+1)}, \quad \alpha(\phi_+) = 1. \quad (3.43)$$

Equation (3.43) is separable with an integral giving an implicit relation between α and $\bar{\phi}$.

Defining $M = \frac{n-m}{n+m-2}$, the relation is

$$\begin{cases} \alpha e^{2(\alpha-1)} = \left(\frac{\bar{\phi}}{\phi_+}\right)^{2-2n}, & m+n=2 \\ \alpha \left(\frac{\alpha+M}{1+M}\right)^{2M-1} = \left(\frac{\bar{\phi}}{\phi_+}\right)^{m-n}, & \text{otherwise.} \end{cases} \quad (3.44)$$

The implicit function theorem proves that eq. (3.44) can be solved for $\alpha(\bar{\phi})$, provided $\alpha \neq -\frac{1}{2}$.

From eq. (3.43), $\alpha = -\frac{1}{2}$ corresponds to a singularity in the righthand side of the ODE. Moreover, negative values of α lead to negative average porosity which is unphysical. Therefore, we can generally solve eq. (3.44) to get $\alpha = \alpha(\bar{\phi})$.

To find the speed of the trailing linear wave packet s_- , we evaluate eq. (3.44) at the trailing

edge. There we find $\alpha(1) = \alpha_-$, with the initial condition (3.39), satisfies the implicit relation

$$\begin{cases} \alpha_- e^{2(\alpha_- - 1)} = \phi_+^{2(n-1)}, & m + n = 2, \\ \alpha_- \left(\frac{\alpha_- + M}{1 + M} \right)^{2M-1} = \phi_+^{n-m}, & \text{otherwise.} \end{cases} \quad (3.45)$$

Given particular values for the parameters, we can solve this expression for α_- , analytically or numerically. Note that for the physical range of (n, m) , α_- is a decreasing function of ϕ_+ . Via the transformation (3.42), we obtain k_- , the wavenumber at the trailing edge. Upon substitution into the group velocity (3.16), the trailing edge speed is

$$s_- = \frac{-n(k_-^2 - 1)}{(k_-^2 + 1)^2} = -n\alpha_-(1 - 2\alpha_-). \quad (3.46)$$

In general, we cannot find an explicit relation for α_- in (3.45) analytically, but when $m = 1$, $M = 1$ and the expression simplifies to a quadratic equation in α_- whose physical solution is

$$\alpha_- = -\frac{1}{2} \left[1 - (1 + 8\phi_+^{n-1})^{\frac{1}{2}} \right], \quad m = 1. \quad (3.47)$$

Then for $m = 1$, substitution of eq. (3.47) into eq. (3.46) yields the trailing edge speed

$$s_- = \frac{1}{2}n \left[3 + 8\phi_+^{n-1} - 3(1 + 8\phi_+^{n-1})^{\frac{1}{2}} \right], \quad m = 1. \quad (3.48)$$

Equation (3.48) provides a simple formula for the trailing edge speed in terms of the parameter n and the jump height ϕ_+ when $m = 1$, e.g. in viscous fluid conduits.

An interesting physical question to consider is whether the trailing edge speed can take on negative values for some choice of the parameters. Recall that even though the phase velocity is always positive, the linear group velocity (3.16), corresponding to the trailing edge speed, can be negative. Returning to the problem of vertical magma flow from a chamber, such a result would imply that for a magma chamber supplying a matrix of sufficiently small porosity relative

to the chamber, porosity waves could transmit back into the chamber and cause the matrix within the chamber to compact and distend. We refer to this condition as backflow. From our discussion in Section 3.4.1, the group velocity evaluated at the trailing edge becomes negative when $k_-^2 = \phi_-^{m-n}$, or $\alpha_- = \frac{1}{2}$. Using the determination of α_- (3.45), backflow occurs for any choice of (n, m) when $\alpha_- \leq \frac{1}{2}$. Substituting this value into eq. (3.45) gives the critical value $\phi_+ = \phi_b$ such that for any $\phi_+ < \phi_b$, $s_- < 0$:

$$\phi_b = \begin{cases} \left(\frac{1}{2e} \right)^{\frac{1}{2(n-1)}}, & m+n=2, \\ \left\{ \frac{1}{2} \left[\frac{1+2M}{2(1+M)} \right]^{2M-1} \right\}^{\frac{1}{n-m}}, & \text{otherwise.} \end{cases}$$

Negative propagation of porosity waves for sufficiently large jumps was observed numerically in [109] but could not be explained using viscous shock theory. Here we have identified an exact jump criterion that initiates backflow.

3.5.3 Determination of the Leading Edge Speed and Amplitude

The leading edge speed could be derived in a similar fashion to the trailing edge, but [24] describes a simpler approach by introducing a different system of basis modulation variables. The main idea is to mirror the description of the linear wave edge by introducing conjugate variables so that the potential curve $g(\phi)$, as in figure 3.2, is reflected about the ϕ axis. Then, averaging is carried out by integrating over the interval (ϕ_1, ϕ_2) where $-g(\phi) > 0$. The $\phi_2 \rightarrow \phi_1$ limit at the soliton edge now resembles the $\phi_2 \rightarrow \phi_3$ limit at the linear edge. The conjugate wavenumber \tilde{k} is defined as

$$\tilde{k} = \pi \left(\int_{\phi_1}^{\phi_2} \frac{d\phi}{\sqrt{-g(\phi)}} \right)^{-1}, \quad (3.49)$$

and will play the role of the amplitude a . $\Lambda = \frac{k}{\bar{k}}$ will be used instead of the wavenumber k . In the conjugate variables, the asymptotic matching conditions become

$$\begin{aligned} z = z_1(t) : \quad \bar{\phi} = 1, \quad \tilde{k} = 0, \quad \phi_2 \rightarrow \phi_3, \\ z = z_2(t) : \quad \bar{\phi} = \phi_+, \quad \Lambda = 0, \quad \phi_2 \rightarrow \phi_1. \end{aligned}$$

In the modulation system, the reduction of the magma conservation laws to the dispersionless limit (3.33) is retained, but the conservation of waves condition is rewritten in the new variables. To do so, it is helpful to define the conjugate wave frequency $\tilde{\omega} = \tilde{\omega}(\tilde{k}, \bar{\phi}, \Lambda) = -i\omega(i\tilde{k}, \bar{\phi}, a(\tilde{k}, \Lambda))$. Assuming the existence of a simple wave, the $\Lambda \rightarrow 0$ limiting behavior of the modulation system takes the form

$$\frac{d\tilde{k}}{d\bar{\phi}} = \frac{\tilde{\omega}_{\bar{\phi}}}{n\bar{\phi}^{n-1} - \tilde{\omega}_{\tilde{k}}}, \quad (3.50)$$

and

$$\Lambda_T + \frac{\tilde{\omega}}{\tilde{k}} \Lambda_Z = O(\Lambda \Lambda_Z).$$

Then the integral curve $\tilde{k} = \tilde{k}(\bar{\phi})$ satisfying eq. (3.50), which is the same expression as in the leading edge system (3.40) but in the conjugate variables, corresponds to the characteristics $\frac{dZ}{dT} = \frac{\tilde{\omega}_s(\tilde{k}, \bar{\phi})}{\tilde{k}}$, where now the characteristic speed is the conjugate phase velocity. Here $\tilde{\omega}_s(\tilde{k}, \bar{\phi}) = \tilde{\omega}(\tilde{k}, \bar{\phi}, 0)$ is called the solitary wave dispersion relation and is obtained from its expression in terms of the linear dispersion relation $\tilde{\omega}_s(\tilde{k}, \bar{\phi}) = -i\omega_0(i\tilde{k}, \bar{\phi})$. From eq. (3.15), the solitary wave dispersion relation is

$$\tilde{\omega}_s(\bar{\phi}, \tilde{k}) = \frac{n\bar{\phi}^{n-1}\tilde{k}}{1 - \bar{\phi}^{n-m}\tilde{k}^2}. \quad (3.51)$$

Upon substitution into eq. (3.50) and recalling that \tilde{k} behaves like an amplitude, the GP matching condition at the trailing edge takes the form $\tilde{k}(1) = 0$ so that we arrive at the IVP

$$\frac{d\tilde{k}}{d\bar{\phi}} = \frac{\tilde{k} \left[n - 1 - (1 + m)\tilde{k}^2\bar{\phi}^{n-m} \right]}{\bar{\phi} \left[(1 + \bar{\phi}^{n-m}\tilde{k}^2)^2 - (1 - \bar{\phi}^{n-m}\tilde{k}^2) \right]}, \quad \tilde{k}(1) = 0. \quad (3.52)$$

Again, a change of variables will lead to a separable ODE which yields an implicit representation, this time for the conjugate wavenumber at the leading edge. Defining

$$\tilde{\alpha} = \frac{\tilde{\omega}_s}{c(\bar{\phi})\tilde{k}} = \frac{1}{1 - \bar{\phi}^{n-m}\tilde{k}^2}, \quad (3.53)$$

the $\tilde{\alpha}$ IVP is

$$\frac{d\tilde{\alpha}}{d\bar{\phi}} = -\frac{[(m+n-2)\tilde{\alpha} + n - m]\tilde{\alpha}}{\bar{\phi}(2\tilde{\alpha} + 1)}, \quad \tilde{\alpha}(1) = 1. \quad (3.54)$$

This equation is the same as eq. (3.43) but with a different initial location because integration takes place from the trailing edge to the leading edge. Note that for the physical range of the constitutive parameters (n, m) , $\tilde{\alpha}$ is a decreasing function of $\bar{\phi}$. Integrating (3.54) gives the relation between $\tilde{\alpha}$ and $\bar{\phi}$

$$\begin{cases} \tilde{\alpha}e^{2(\tilde{\alpha}-1)} = \bar{\phi}^{2-2n}, & m+n=2 \\ \tilde{\alpha}\left(\frac{\tilde{\alpha}+M}{1+M}\right)^{2M-1} = \bar{\phi}^{m-n}, & \text{otherwise.} \end{cases} \quad (3.55)$$

and the requirement $\tilde{\alpha} > -\frac{1}{2}$ for finding $\tilde{\alpha} = \tilde{\alpha}(\bar{\phi})$. For all physically relevant $\bar{\phi} > 0$, $\tilde{\alpha} > 0$. Using the solitary wave dispersion relation, the leading edge speed s_+ becomes

$$s_+ = \frac{\tilde{\omega}_s(\phi_+, \tilde{k}_+)}{\tilde{k}_+} = \frac{n\phi_+^{n-1}}{1 - \phi_+^{n-m}\tilde{k}_+^2}, \quad (3.56)$$

where $\tilde{k}_+ = \tilde{k}(\phi_+)$. Defining $\tilde{\alpha}_+ = \tilde{\alpha}(\phi_+)$, we find $\phi_+^{n-m}\tilde{k}_+^2 = 1 - \frac{1}{\tilde{\alpha}_+}$, which upon substitution into eq. (3.56) yields

$$s_+ = n\phi_+^{n-1}\tilde{\alpha}_+, \quad (3.57)$$

for any choice of m . To solve for the solitary wave speed, we evaluate the implicit relation for $\tilde{\alpha}$ at the leading edge and insert into (3.57). The defining relations for $\tilde{\alpha}_+$ are found by evaluating

$\tilde{\alpha}(\phi_+)$ in (3.55)

$$\begin{cases} \tilde{\alpha}_+ e^{2(\tilde{\alpha}_+ - 1)} = \phi_+^{2-2n}, & m + n = 2 \\ \tilde{\alpha}_+ \left(\frac{\tilde{\alpha}_+ + M}{1 + M} \right)^{2M-1} = \phi_+^{m-n}, & \text{otherwise} . \end{cases} \quad (3.58)$$

Because $\tilde{\alpha}$ is a decreasing function and $\tilde{\alpha}(1) = 1$ and $\phi_+ < 1$, $\tilde{\alpha}_+ = \tilde{\alpha}(\phi_+)$ is an increasing function of ϕ_+ . As in the trailing edge, the case $m = 1$ can be solved explicitly so the leading edge speed is

$$s_+ = \frac{1}{2}n \left[\left(1 + 8\phi_+^{n-1} \right)^{\frac{1}{2}} - 1 \right], \quad m = 1 .$$

Here we have determined an explicit relation between the jump height, the constitutive parameter n , and the leading edge speed.

Determination of the leading edge amplitude a_+ follows from the solitary wave amplitude-speed relation (3.28), rescaled to a background porosity ϕ_+ using the scaling symmetry in eq. (3.18). In practice, a_+ is computed numerically.

3.5.4 Analysis of the Theoretical Predictions

The theoretical predictions of Sections 3.5.2 and 3.5.3 were limited to explicit speed formulae for the $m = 1$ case. In this section, we extend those results to the full physical range of the constitutive parameters. We will also check that the speeds satisfy the DSW admissibility criteria [24] and are consistent with KdV asymptotics in the weakly nonlinear limit.

First, we consider the DSW admissibility criteria. The dispersionless limit of the magma equation (3.33) has the characteristic speed $c = n\phi^{n-1}$. As the DSW evolves, it continuously expands with speeds s_- at the trailing edge and s_+ at the leading edge. For the DSW construction to be valid, the external characteristics must impinge upon the DSW region, transferring information from the dispersionless region into the modulated one-phase region. Then the DSW and external characteristic speeds must satisfy the relations $s_- < n$ and $s_+ > n\phi_+^{n-1}$. These conditions ensure a compressive DSW. Using the expressions for the speeds (3.46) and (3.57)

we find that in the interior of the shock region

$$s_- = -n\alpha_-(1 - 2\alpha_-) < n = c(1), \quad s_+ = n\phi_+^{n-1}\tilde{\alpha}_+ > n\phi_+^{n-1} = c(\phi_+), \quad (3.59)$$

because $\alpha_- < 1$ and $\tilde{\alpha}_+ > 1$ for $\phi_+ < 1$ as shown earlier. To admit a solitary wave-led dispersive shock solution as we have constructed, it must also be the case that $s_- < s_+$ so that the interior region continues to expand in time. We have verified numerically that this condition is satisfied for choices of the constitutive parameters and the jump height in the physical range. Hence, our analytical predictions for the speeds satisfy the DSW admissibility criteria.

Following our discussion in Section 3.4.2 of the weakly nonlinear limit $0 < 1 - \phi_+ \ll 1$, eqs. (3.46) and (3.57) must be consistent with the standard KdV speeds and amplitude for the KdV reduction of the magma equation (3.19)

$$s_- = n - (1 - \phi_+)2n(n - 1) \quad (3.60)$$

$$k_- = \left((1 - \phi_+) \frac{2}{3} n(n - 1) \right)^{1/2} \quad (3.61)$$

$$s_+ = n - (1 - \phi_+) \frac{1}{3} n(n - 1) \quad (3.62)$$

$$a_+ = 2(1 - \phi_+), \quad 0 < 1 - \phi_+ \ll 1. \quad (3.63)$$

Using an asymptotic expansion for α and $\tilde{\alpha}$ near 1 in expressions (3.45) and (3.58), respectively and a small amplitude expansion for the leading edge wave amplitude a_+ in the solitary wave amplitude-speed relation (3.28), we have verified that equations (3.60) – (3.63) indeed do describe the first order asymptotics of the magma results in equations (3.46), (3.57), and (3.28).

We now consider the speeds for more general parameter values over the full range of ϕ_+ , for which one must solve numerically by implicitly solving the expressions (3.45) and (3.58). To solve for the leading edge amplitudes, we invert the amplitude-speed relation (3.28) with a background porosity $\Phi = \phi_+$. In order to understand the effects of the constitutive parameters (n, m) on

DSW behavior, consider figures 3.3a and 3.3b that show the normalized predicted leading and trailing edge speeds s_+/n and s_-/n of the magma DSW as a function of the downstream porosity ϕ_+ for $m = 0$ and $m = 1$, respectively. The two plots look qualitatively similar indicating that the degree of nonlinearity n appears to have the greatest impact on DSW speeds while m has only a modest effect. The associated leading solitary wave amplitudes are plotted in figures 3.3c and 3.3d. In the amplitude plots, the lighter dashed lines indicate the predictions based on the weakly nonlinear KdV limit. The amplitudes of the leading edge depend rather dramatically on the choice of the viscosity constitutive parameter m . The inclusion of a porosity weakening matrix viscosity amplifies porosity wave oscillations causing the leading edge to grow large as the jump grows, bounded from below by the KdV amplitude. In the $m = 0$ case, however, the amplitudes grow less rapidly and are approximately bounded above by the KdV amplitude result.

From the plots of the trailing edge speeds 3.3a and 3.3b, we note that not only do the speeds take on negative values as we discussed in Section 3.5.2, but they also assume a global minimum in the interior of the ϕ_+ domain. Taking a derivative of eq. (3.46) with respect to ϕ_+ yields

$$\frac{ds_-}{d\phi_+} = \begin{cases} \frac{2(n-1)n(4\alpha_- - 1)\phi_+^{2n-3}e^{-2(\alpha_- - 1)}}{1 + 2\alpha_-}, & m + n = 2, \\ \frac{n(n-m)(4\alpha_- - 1)\phi_+^{n-m-1}\left(\frac{\alpha_- + M}{1+M}\right)^{1-2M}}{1 + \alpha_- \left(\frac{2M-1}{\alpha_- + M}\right)}, & \text{otherwise.} \end{cases}$$

Then the trailing edge speed derivative is zero only when $\alpha_- = \alpha_{\min} = \frac{1}{4}$. Inserting this value of α back into eq. (3.46), we find that the minimum linear speed, for any choice of (n, m) has the universal scaled value

$$\frac{s_-(\alpha_{\min})}{n} = -\frac{1}{8}. \quad (3.64)$$

We can use the expression (3.45) and $\alpha_- = \frac{1}{4}$ to find that the linear speed takes on a minimum

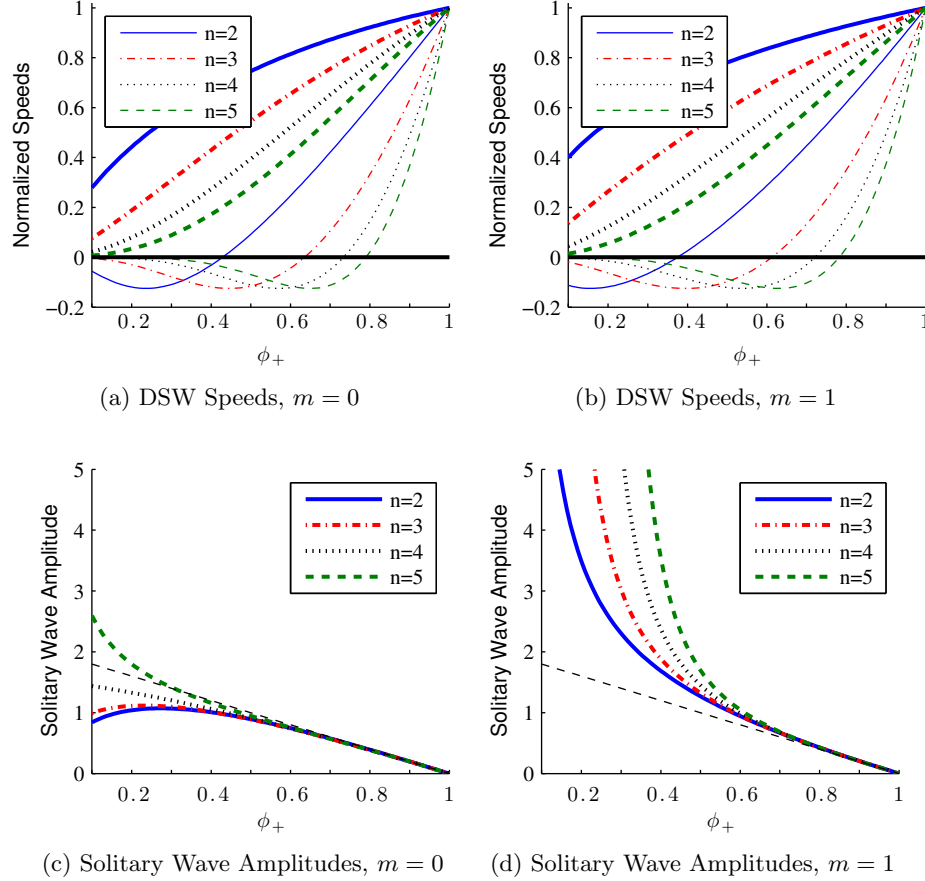


Figure 3.3: Analytical predictions for the normalized speeds and amplitude of magma DSWs. In (a) and (b) the thicker curves indicate the leading edge speeds, and the thinner curves show the trailing edge speeds. Note the existence of a zero and a universal global minimum in the normalized trailing edge speeds for all cases of (n, m) . For (c) and (d), the thinner dashed line is the KdV amplitude result.

when $\phi_+ = \phi_{\min}$ where

$$\phi_{\min} = \begin{cases} \left(\frac{1}{4} e^{-\frac{3}{2}} \right)^{\frac{1}{2(n-1)}}, & m+n=2 \\ \left\{ \frac{1}{4} \left[\frac{1+4M}{4(1+M)} \right]^{2M-1} \right\}^{\frac{1}{n-m}}, & \text{otherwise.} \end{cases} \quad (3.65)$$

Note then for $m=1$, we can explicitly verify from eq. (3.48) that $\phi_b > \phi_{\min}$. We confirm that this inequality holds for any choice of (n, m) in the valid range. We will say more about the significance of ϕ_{\min} and its relation with ϕ_b in Section 3.6.2.

3.6 Comparison with Numerical Simulations

The purpose of this section is to compare the analytical predictions of Section 3.5 for the speeds and amplitudes of magma DSWs with careful numerical simulations, as well as to use simulations to examine the internal shock structure. We see strong agreement between predictions and numerics for small to moderate jumps and identify criteria for the breakdown of the theoretical construction for large amplitudes. We find in particular that for $\phi_+ < \phi_{\min}$, the DSW implodes. This regime is characterized by the onset of internal wave interactions corresponding to gradient catastrophe in the Whitham modulation equations.

3.6.1 Numerical Simulations

The magma equation (3.1) with initial data given by (3.39) was simulated using a finite difference spatial discretization and an explicit Runge-Kutta time stepping method. Details of our numerical method and accuracy verification are found in Appendix 3.8. Studying numerical simulations allows us not only to verify the analytical predictions described in Section 3.5, but also to study the internal structure of the DSWs, which we sought to bypass before, as well as the limitations of the asymptotic DSW construction

We choose to focus on two particular parameter regimes, $(n, m) \in \{(2, 1), (3, 0)\}$. The first

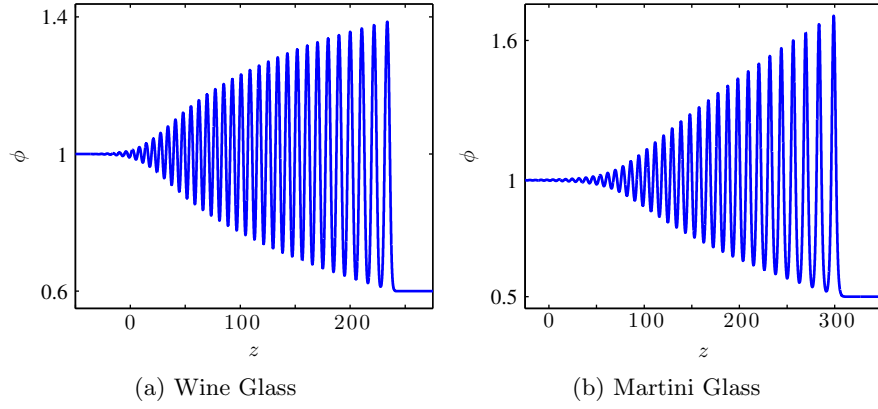


Figure 3.4: Two different types of envelope structures observed in simulations of eq. (3.1). (a) The numerical solution at $t = 120$ for parameter values $\phi_+ = 0.6$, $(n, m) = (3, 0)$. (b) The magma equation at $t = 200$ for parameter values $\phi_+ = 0.5$, $(n, m) = (2, 1)$.

case is physically motivated by the fluid conduit problem described in Section 3.3.2 while the second was the problem studied numerically by [109] and [73]. Further, taking different values for n and m in each case allows us to illustrate the different DSW forms arising from eq. (3.1). Figure 3.4 shows the difference in the internal oscillatory structure which results from varying the values of the constitutive parameters. In language consistent with [56], figure 3.4a when $(n, m) = (3, 0)$, depicts a wave envelope in the form of a wine glass, while in figure 3.4b with $(n, m) = (2, 1)$, the envelope resembles the shape of a martini glass. The degree of nonlinearity n influences the internal structure of the DSW.

In figure 3.5 we show how the numerically simulated leading edge speed and amplitude compare with our predicted values. From figure 3.5a, we obtain strong agreement for $\phi_+ \in (0.5, 1)$ but increasing deviation thereafter. Figure 3.5c gives a similar picture for the amplitudes, though curiously the calculated amplitudes appear better predicted by the KdV asymptotics for larger jump sizes. From figure 3.5b and 3.5d, we see strong quantitative agreement for jumps up to $\phi_+ = 0.2$, but then increased disagreement for the larger jump. It is interesting to note that in the case $(n, m) = (3, 0)$, the leading edge speed is consistently underestimated, and thus the leading edge amplitude is as well, while in the case $(n, m) = (2, 1)$ they are consistently

overestimated. We also observe that good agreement with the speed and amplitude predictions occurs even for negative trailing edge velocities. This demonstrates that backflow is a real physical feature of eq. (3.1), not just a mathematical artifact of the solution method. Note also that while our numerical simulations for the leading solitary wave may deviate from the DSW predictions, we verify that the leading edge is indeed a well-formed solitary wave that satisfies the soliton amplitude-speed relation. With the numerically extracted amplitudes we compute the predicted speed from eq. (3.28) and compare it with the speed extracted from the simulations. The relative errors over all simulations are less than 0.3 %. The trailing edge speeds were more difficult to extract in an objective, systematic manner due to the different structures of the trailing edge wave envelope. Instead, we show a contour plot of sample solutions in the z - t plane for the two different cases $(n, m) = (3, 0)$ in figure 3.6a and $(n, m) = (2, 1)$ in figure 3.6b. Overlying the contour plots are the predicted DSW region boundary slopes from Section 3.5. One can see that our predictions are in excellent agreement with numerical simulations. We will further validate our predictions of the linear edge speeds in Section 3.6.2.

This excellent agreement between predictions and numerical simulations in the case of small to moderate amplitude jumps has been seen in other non-integrable physical systems, cf. [29, 26]. However, deviations in the large jump regime are also observed, leading one to question the validity of the method in the case of large amplitude. [25] posits genuine nonlinearity in the modulation equations as one possible assumption that could be violated as the jump size increases. We will generalize their criteria in the next section by introducing four verifiable conditions which violate our analytical construction.

3.6.2 Breakdown of Analytical Method

The Whitham-El DSW simple wave closure method used here requires the existence of a self-similar simple wave solution to the full set of the Whitham modulation equations. In this section, we identify two mechanisms that lead to the breakdown of this simple wave theory, the onset of linear degeneracy or zero dispersion. In the former case, a loss of monotonicity manifests such

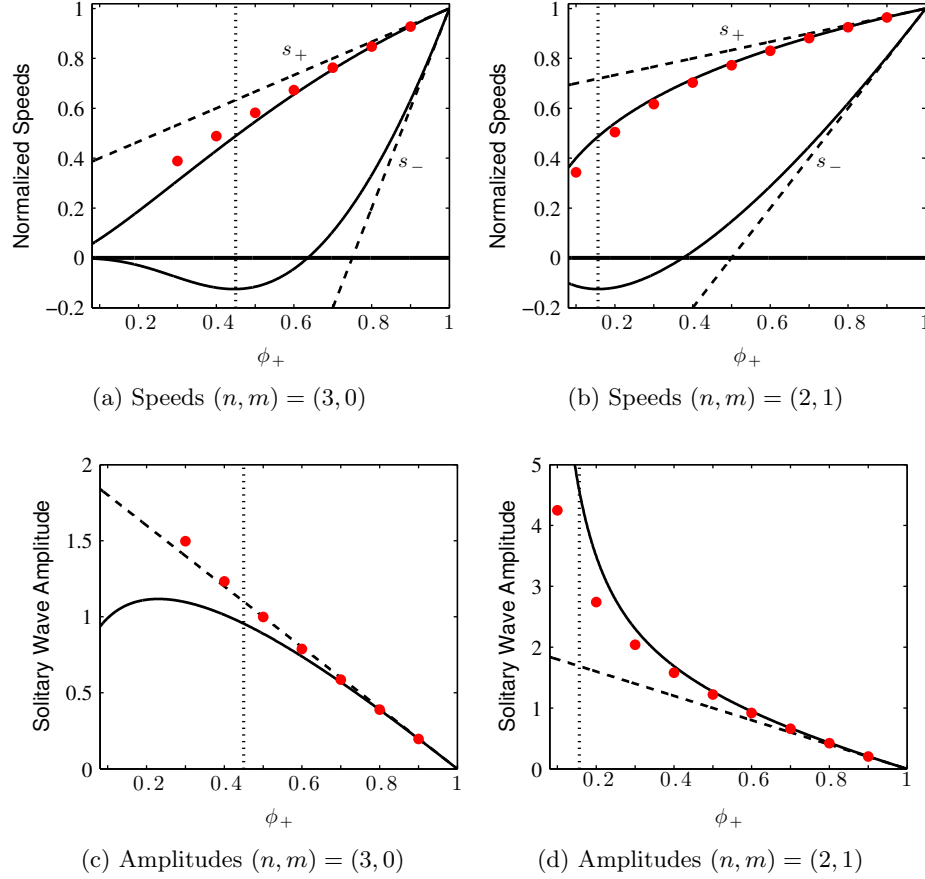


Figure 3.5: Comparisons for $(n, m) = (3, 0)$ and $(n, m) = (2, 1)$ of the predicted (solid lines) versus computed values (dot points) of the leading edge speeds and amplitudes for varying ϕ_+ . The dashed lines indicate the predictions from KdV theory in the weakly nonlinear regime. The vertical dotted line is the critical jump height ϕ_c , beyond which the analytical theory is no longer valid.

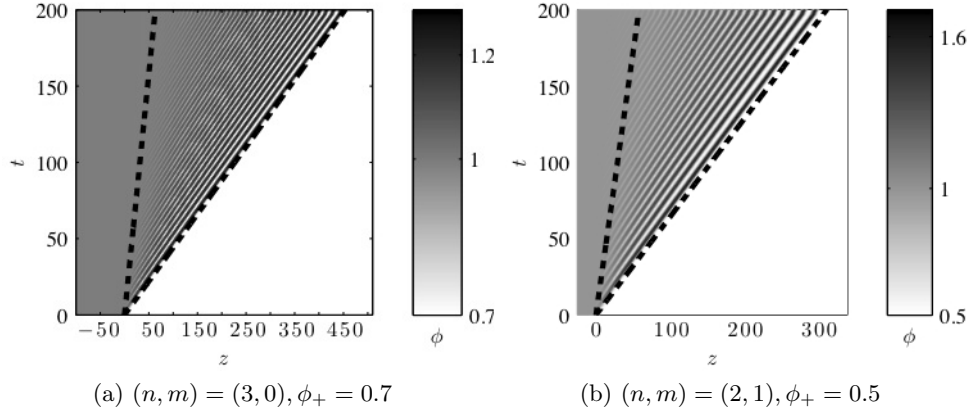


Figure 3.6: Contour plots of numerical solutions for $\phi(z, t)$ plotted in the characteristic z - t plane for different parameter values with the overlying dashed lines indicating the predicted values for the leading and trailing edge speeds. The angles (speeds) line up excellently.

that the simple wave can no longer be continued. For the latter case, zero dispersion corresponds to a gradient catastrophe in the Whitham modulation equations leading to compression and implosion of the DSW.

First we consider the zero dispersion case at the trailing edge. The right eigenvector of the system (3.36), (3.37) associated with the characteristic speed $\frac{\partial}{\partial k}\omega_0$ of the trailing edge is $[0, 1]^T$. Therefore, in the vicinity of the trailing edge, the self-similar simple wave satisfies

$$\bar{\phi}' = 0, \quad k' = \left(\frac{\partial^2 \omega_0}{\partial k^2} \right)^{-1}.$$

Hence, if $\frac{\partial^2}{\partial k^2}\omega_0(k, 1) \rightarrow 0$ for k near k_- , gradient catastrophe in the modulation system is experienced. This condition corresponds to a change in the sign of dispersion and is equivalent to the loss of genuine nonlinearity in the trailing edge system itself. As we will show later, this is distinct from the loss of genuine nonlinearity of the full Whitham modulation system, in the limit of the trailing edge. Recalling that the sign of dispersion changes when $k^2 = 3\Phi^{m-n}$ (see eq. (3.17)), we have the criterion $k_- \geq \sqrt{3}$ leading to gradient catastrophe. More generally, for any simple wave, one-phase DSW resulting from step-like initial data of a scalar, dispersive,

nonlinear wave equation for ϕ , we can formulate the following condition which must hold for the assumption of a continuously expanding, one-phase region:

$$\left. \frac{\partial^2}{\partial k^2} \omega_0(k, \bar{\phi}) \right|_{(k_-, \phi_-)} < 0. \quad (3.66)$$

The criterion (3.66) holds for systems with negative dispersion in the long wavelength regime, the inequality reversed for the positive dispersion case. This is a natural generalization of the criterion in modulated *linear* wave theory where a change in the sign of dispersion is associated with the formation of caustics and break down of the leading order stationary phase method [85]. It is notable that Whitham hypothesized that breaking of the modulation equations could lead to an additional source of oscillations (see Section 15.4 in [126]). Previous works have resolved breaking in the Whitham equations by considering modulated multiphase waves in the context of DSW interactions [37, 48, 2] or in the context of certain initial value problems [51]. Beginning with the initial, groundbreaking work [30] on multiphase Whitham averaging for KdV, all studies since have involved integrable systems. Since k_- is a monotonically decreasing function of ϕ_+ for the magma DSW, we expect gradient catastrophe and DSW implosion for sufficiently large jumps, i.e. $\phi_+ < \phi_c$ for the critical jump height ϕ_c . Using our work in Section 3.5, we can derive ϕ_c for which we violate (3.66). We note the following

$$\frac{d}{d\phi_+} \left[\frac{\partial}{\partial k} \omega_0(k_-, 1) \right] = - \left(\frac{\partial^2}{\partial k^2} \omega_0(k_-, 1) \right) k'(1). \quad (3.67)$$

The trailing edge wavenumber $k_- = k(1)$ depends on ϕ_+ through the initial condition $k(\phi_+) = 0$ (recall eq. (3.40)). Therefore, in eq. (3.67), $dk_-/d\phi_+ = -k'(1)$. Hence, the change in sign of dispersion evaluated at the trailing edge coincides with a minimum of the linear edge speed as a function of ϕ_+ (see figures 3.3a and 3.3b). The dispersion sign changes from negative to positive when $\phi_+ = \phi_c = \phi_{\min}$, where ϕ_{\min} is given in eq. (3.65). Our analytical method then is no longer valid for jumps larger than this threshold value. This coincidence of a global minimum edge speed and breakdown of the analytical method was also noted in the case of unsteady,

undular bores in shallow-water by [25], however the mechanism was argued to be due to the loss of genuine nonlinearity in the modulation system. The sign of dispersion did not change.

A similar argument holds in the vicinity of the leading edge. There, gradient catastrophe occurs if the conjugate phase velocity (i.e. the speed of the leading edge) increases with decreasing \tilde{k} . Then one-phase behavior is expected to be retained when

$$\left. \frac{\partial}{\partial \tilde{k}} \left(\frac{\tilde{\omega}_s}{\tilde{k}} \right) \right|_{(\tilde{k}_+, \phi_+)} > 0. \quad (3.68)$$

The condition (3.66) says that the sign of dispersion must remain negative when evaluated at the trailing edge. The second condition (3.68) requires that the sign of the conjugate dispersion (now defined through changes in the phase velocity) remain positive when evaluated at the leading edge. Verifying (3.68), we find that it does indeed hold for every $\phi_+ \in (0, 1)$.

The simple wave construction also requires that the full modulation system be strictly hyperbolic and genuinely nonlinear. Strict hyperbolicity of the full modulation system requires the three characteristics be real and distinct at all points except at the DSW boundaries which correspond to the merger of two characteristics. In integrable systems, this can be validated directly due to the availability of Riemann invariants, but in the non-integrable case we assume strict hyperbolicity. Genuine nonlinearity, on the other hand, is a condition necessary for the construction of the integral curve connecting the leading and trailing edges and requires that the characteristic speed λ varies *monotonically* along the integral curve. Again, we cannot check this condition for all parameters in the full modulation system, but we can in neighborhoods near the boundaries. Parameterizing the integral curve by $\bar{\phi}$, the monotonicity criteria are

$$\left. \frac{d\lambda}{d\bar{\phi}} \right|_{(k=k_-, \bar{\phi}=1, a=0)} = \frac{\partial \lambda}{\partial k} k' + \frac{\partial \lambda}{\partial \bar{\phi}} + \frac{\partial \lambda}{\partial a} \frac{da}{d\bar{\phi}} \Big|_{(k=k_-, \bar{\phi}=1, a=0)} < 0, \quad (3.69)$$

$$\left. \frac{d\lambda}{d\bar{\phi}} \right|_{(\tilde{k}=\tilde{k}_+, \bar{\phi}=\phi_+, \Lambda=0)} = \frac{\partial \lambda}{\partial \tilde{k}} \tilde{k}' + \frac{\partial \lambda}{\partial \bar{\phi}} + \frac{\partial \lambda}{\partial \Lambda} \frac{d\Lambda}{d\bar{\phi}} \Big|_{(\tilde{k}=\tilde{k}_+, \bar{\phi}=\phi_+, \Lambda=0)} > 0. \quad (3.70)$$

These monotonicity conditions are the correct way to determine genuine nonlinearity at the

trailing and leading edges. Testing for genuine nonlinearity in the reduced system of two modulations equations fails to provide the proper condition (recall eq. (3.66)) because they are restricted to the $a = 0$ plane. Since the trailing and leading edges correspond to double characteristics, right and left differentiability, respectively, imply $\frac{\partial \lambda}{\partial a} \rightarrow 0$ and $\frac{\partial \lambda}{\partial \Lambda} \rightarrow 0$ at the appropriate edge. Also, the limiting characteristic speeds are $\lambda \rightarrow \frac{\partial}{\partial k} \omega_0$ and $\lambda \rightarrow \frac{\tilde{\omega}}{k}$ at the trailing and leading edges, respectively. Then the monotonicity criteria (3.69) and (3.70), after the change of variables to α and $\tilde{\alpha}$, simplify to

$$\begin{aligned} \left. \frac{d\lambda}{d\bar{\phi}} \right|_{(k=k_-, \bar{\phi}=1, a=0)} &= \frac{\frac{\partial^2}{\partial k^2} \omega_0 \frac{\partial}{\partial \bar{\phi}} \omega_0}{n\bar{\phi}^{n-1} - \frac{\partial}{\partial k} \omega_0} + \left. \frac{\partial^2 \omega_0}{\partial k \partial \bar{\phi}} \right|_{(k=k_-, \bar{\phi}=\phi_-, a=0)} \\ &= -\frac{n\alpha_- (16\alpha_-^3 m - (16m+4)\alpha_-^2 + (3n-m+2)\alpha_- + m-1)}{2\alpha_- + 1} < 0, \end{aligned} \quad (3.71)$$

$$\begin{aligned} \left. \frac{d\lambda}{d\bar{\phi}} \right|_{(\tilde{k}=\tilde{k}_+, \bar{\phi}=\phi_+, \Lambda=0)} &= \frac{\frac{\partial}{\partial \bar{\phi}} \tilde{\omega}_0 (\tilde{k} n \bar{\phi}^{n-1} - \tilde{\omega}_0)}{\tilde{k}^2 \left(n \bar{\phi}^{n-1} - \frac{\partial}{\partial \tilde{k}} \tilde{\omega}_0 \right)} \Big|_{(\tilde{k}=\tilde{k}_+, \bar{\phi}=\phi_+, \Lambda=0)} \\ &= \frac{\phi_+^{n-2} n \tilde{\alpha} (4\tilde{\alpha}^2 + (n-m+4)\tilde{\alpha} + m-1)}{2\tilde{\alpha} + 1} > 0. \end{aligned} \quad (3.72)$$

When either of these two conditions is not satisfied, a breakdown in genuine nonlinearity of the full 3×3 modulation system occurs at the boundaries, (3.71) and (3.72) corresponding to the trailing, linear edge and the leading solitary wave edge, respectively. We can verify analytically that for any value of $\phi_+ \in (0, 1)$ and for all (n, m) in the physical range, condition (3.72) is satisfied. For the linear edge condition (3.71), however, we can derive a condition for ϕ_+ such that the monotonicity condition is broken. Linear degeneracy first occurs when $\alpha = \alpha_1$, where α_1 satisfies

$$16m\alpha_1^3 - (16m+4)\alpha_1^2 + (3n-m+2)\alpha_1 + m-1 = 0. \quad (3.73)$$

From the IVP (3.43) and the implicit relation between α and $\bar{\phi}$ (3.45), we know that if there exists an $\alpha_1 \in (0, 1]$ which satisfies (3.73), then we can find $\phi_+ = \phi_1$ such that (3.71) is no longer satisfied. Then for each (n, m) in the physical range, there is a critical jump height ϕ_1 such that

genuine nonlinearity is lost at the trailing edge. Note that for $m = 1$, $\alpha_1 = 0$ is the only root of eq. (3.73) in the valid range and this gives the value $\phi_1 = 0$ which is outside the range of interest. We have verified numerically that $\phi_c > \phi_1$ for all $n \in [2, 5]$, $m \in [0, 1]$ so implosion occurs before the loss of genuine nonlinearity. Before linear degeneracy occurs, the analytical construction has already broken down due to a change in sign of dispersion (3.66). We have found three distinguished jump heights exhibiting the ordering $\phi_b > \phi_c > \phi_1$. As ϕ_+ is decreased through these values, the DSW exhibits backflow and then implosion before it ever reaches linear degeneracy.

Figure 3.7 shows the key results of our analysis. Plots of the numerically computed solutions for the two parameter cases tested in the regimes $\phi_+ \in \{(\phi_b, 1), (\phi_c, \phi_b), (0, \phi_c)\}$ are shown. We see in both cases that our analytical predictions for ϕ_b and ϕ_c are in agreement with the numerical solution as backflow and DSW implosion occur when expected and not otherwise. The choices for ϕ_+ in figure 3.7 were chosen for visual clarity but we have performed further simulations with ϕ_+ much closer to ϕ_b and ϕ_c , finding that they do indeed accurately predict the transitions in DSW behavior. For $\phi_+ < \phi_c$, the DSW rank-ordering breaks down due to catastrophe and results in wave interactions in the interior of the oscillatory region. In figure 3.8 we show an example of how the solution evolves from step initial data for $\phi_+ < \phi_c$. The interior of the DSW initially develops into approximately a modulated one-phase region. However, as the simulation continues, the trailing edge linear waves stagnate due to the minimum in the group velocity. The DSW is compressed as shorter waves at the leftmost edge are overtaken by longer waves from the interior. Wave interactions in the DSW interior ensue. Another one-phase region develops, separated from the main trunk of the DSW by a two-phase region, further clarified by the contour plot of ϕ in the characteristic z - t plane in figure 3.9. We find that the closer ϕ_+ is to ϕ_c , the longer it takes for the interaction region to develop from step initial data.

This analysis suggests not only that our analytical construction accurately captures physically important, critical values in ϕ_+ , but also that our predictions of the trailing edge speed s_- from Section 3.5.2 are consistent with the numerical simulations.

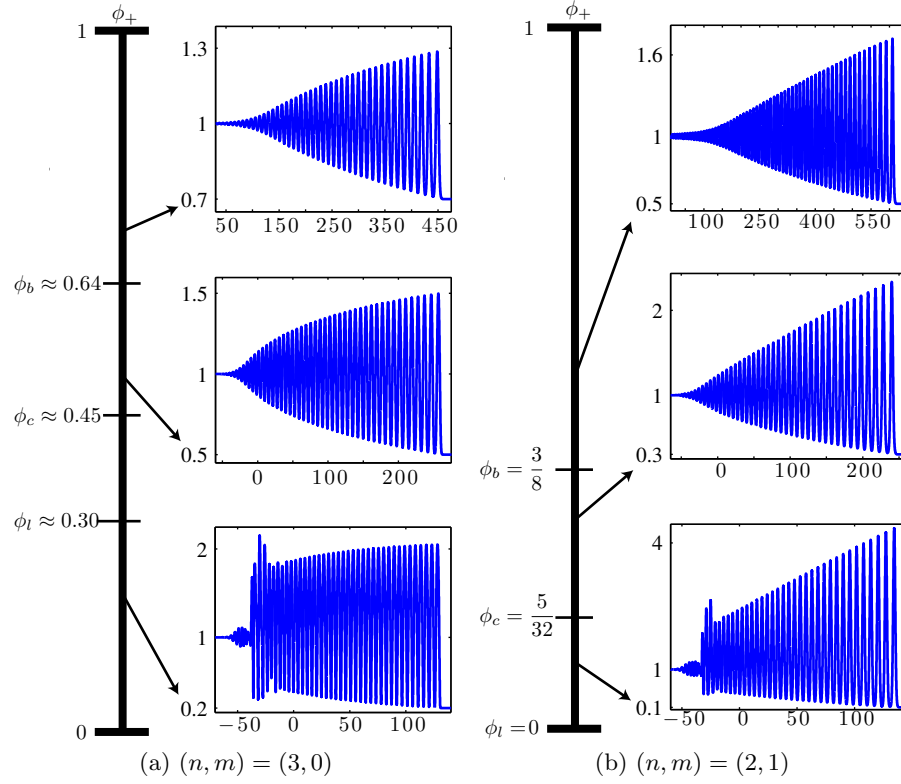


Figure 3.7: From top to bottom, magma DSWs in the forward propagating case, the backflow regime before gradient catastrophe, and after DSW implosion. The solutions shown correspond, from top to bottom, to (a) $t_f = \{200, 150, 150\}$, (b) $t_f = \{400, 200, 200\}$.

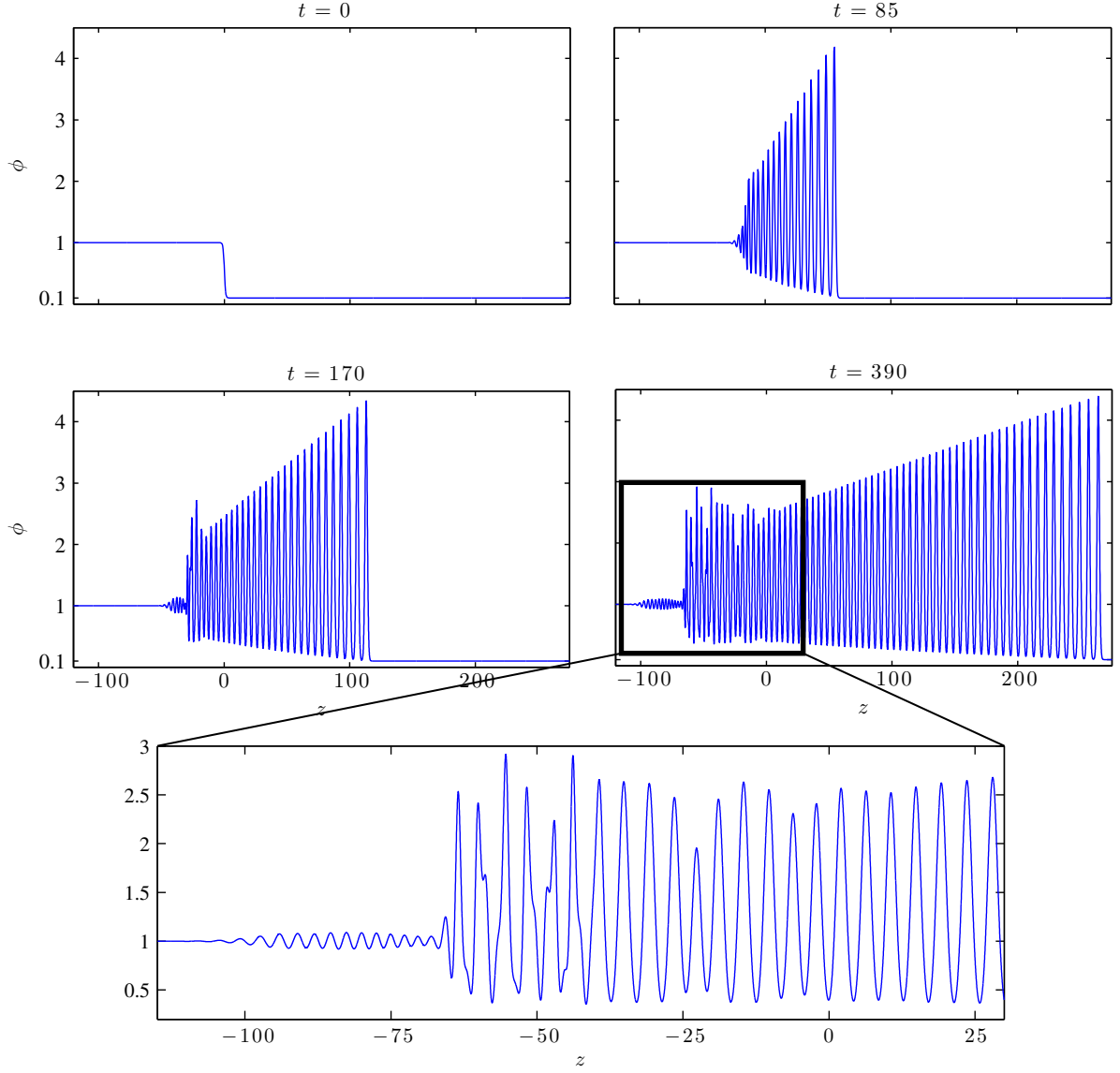


Figure 3.8: DSW implosion. Evolution of the solution to eq. (3.1) with $(n, m) = (2, 1)$, $\phi_+ = .1 < \phi_c \approx 0.16$. The solution initially develops into a typical DSW with one-phase interior, but as it evolves, the trailing edge compresses and longer waves from the interior overtake shorter waves near the edge. Internal wave interactions (implosion) commence and the one-phase assumption is no longer valid.

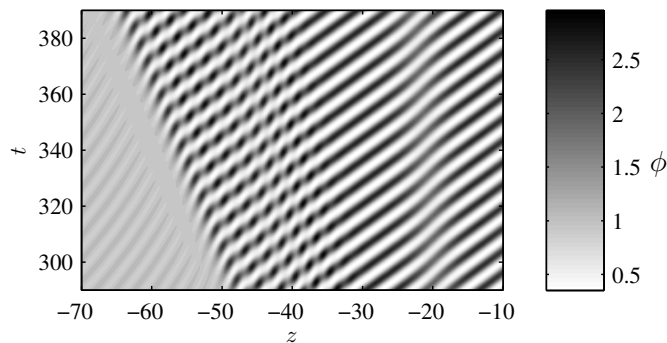


Figure 3.9: Contour plot of numerically computed $\phi(z, t)$ from figure 3.8 in the characteristic z - t plane exhibiting modulated one-phase and two-phase behavior.

3.7 Summary and Conclusions

In summary, we have analytically determined DSW speeds and amplitudes for arbitrary initial jumps and for physical values of the constitutive parameters. It is likely that these results extend directly to non-physical parameter values as well. In figure 3.7, we see backflow and DSW implosion for jumps beyond the catastrophe point ϕ_c , revealing internal wave interactions and the need for modification of the one-phase region ansatz in the description of the DSW. Direct analysis of the full Whitham system would be required for further study, a highly nontrivial task for arbitrary (n, m) . The significance of this work is its characterization of magma DSW solutions, an open problem since observed in [109], its generalization to include the effects of bulk viscosity on porosity oscillations, and, more generally in the field of dispersive hydrodynamics, the new DSW dynamics predicted and observed. A regime which remains to be understood is the flow of a magma into a “dry” region, i.e. $\phi \rightarrow 0$. The original paper [109] conjectured that the leading solitary wave would take on unbounded amplitude, implying physical disaggregation of the multiphase medium. This paper has not explored the behavior of solutions as the jump approaches this singular limit, and a viable alternative approach is yet to be proposed.

Aside from the novelty of dispersive shock behavior in viscously dominated fluids, this work provides the theoretical basis with which to experimentally study DSW generation. Solitary waves

in the fluid conduit system have been carefully studied experimentally [99, 83, 43], showing good agreement with the soliton amplitude/speed relation (3.28) in the weak to moderate jump regime. DSW speeds, the lead solitary wave amplitude, and the onset of backflow are all experimentally testable predictions. Furthermore, the ability to carefully measure DSW properties in this system would enable the first *quantitative* comparison of non-integrable Whitham theory with experiment, previous comparisons being limited to qualitative features [46, 119, 20] or the weakly nonlinear, KdV regime for plasma [116] and the weakly nonlinear, Benjamin-Ono equation for atmospheric phenomena [89]. Due to its experimental relevance, the viscous fluid conduit system deserves further theoretical study in the large amplitude regime. What are the limits of applicability of the magma equation to this system? How do higher order corrections affect the dynamics?

Finally, we have established new, testable criteria for the breakdown of the DSW solution method in equations (3.66), (3.68), (3.69), and (3.70). The additional four admissibility criteria—loss of genuine nonlinearity, change in sign of dispersion at the solitary wave, linear wave edges—apply to the simple wave DSW construction of any nonlinear dispersive wave problem. Linear degeneracy and nonstrict hyperbolicity have been accommodated in various integrable nonlinear wave problems [88, 56, 53]. Extensions to non-integrable problems are needed.

We thank Marc Spiegelman for introducing us to the magma equation and for many helpful suggestions and fruitful discussion. We appreciate thoughtful comments from Noel Smyth. This work was supported by NSF Grant Nos. DGE-1252376 and DMS-1008973.

3.8 Appendix – Numerical method

The magma equation was simulated using a sixth-order finite difference spatial discretization with explicit Runge-Kutta time stepping. The initial condition (3.39) was approximated by a

smoothed step function centered at $z = 0$

$$\phi(z, 0) = \frac{1}{2} \left[(1 + \phi_+) + (\phi_+ - 1) \tanh \left(\frac{z}{4\lambda} \right) \right], \quad (3.74)$$

where ϕ is the porosity and we assume $\phi(z, t) > 0$ and $\phi_+ \in (0, 1)$. The width λ was chosen to be sufficiently large in comparison with the spatial grid spacing, typically $\lambda = 10\Delta z$ for grid spacing Δz . This is reasonable since we are concerned with the long-time asymptotic behavior of the solution and any effects of the initial profile's transients will be negligible. We choose a truncated spatial domain wide enough in order to avoid wave reflections at the boundary. It is also convenient to consider the magma equation in the form (3.8), (3.9). In this form, we have an ODE coupled to a linear elliptic operator $L(\phi)\mathcal{P} = -(\phi^n)_z$. We first solve for \mathcal{P} by discretizing and inverting $L(\phi)$ using sixth-order, centered differences. To obtain boundary conditions, we note $\mathcal{P} = \phi^{-m}\phi_t$, and due to the wide domain, the function ϕ assumes a constant value at the boundaries so \mathcal{P} decays to zero near the boundaries. Hence we implement Dirichlet boundary conditions on the compaction pressure. We then use the solution for \mathcal{P} to update the righthand side of eq. (3.8) and step forward in time using the classical, explicit 4th order Runge-Kutta method. The temporal grid spacing was chosen to satisfy the Courant–Friedrichs–Lewy (CFL) condition for the dispersionless limit, $\frac{\Delta t}{\Delta z} \leq \frac{1}{n}$. Typically, we took $\Delta t = \frac{\Delta z}{2n}$.

The accuracy of our numerical scheme has been determined by simulating solitary wave solutions on a background porosity $\phi = 1$ as derived by [82], for the particular parameter regimes $(n, m) \in \{(2, 1), (3, 0)\}$, used in our analysis. We numerically solve for ϕ from the nonlinear traveling wave equation $(\phi')^2 = g(\phi)$, i.e. eq. (3.24) with $\phi_2 \rightarrow \phi_1$, and use this as our initial profile. The ∞ -norm difference between the numerically propagated solution ϕ^* and the true solitary wave solution ϕ is our figure of merit.

To compute the initial solitary wave profile, we implicitly evaluate

$$z - ct = I = \int_{\phi}^A \frac{d\tilde{u}}{\sqrt{g(\tilde{u})}}, \quad z \leq 0 \quad (3.75)$$

where A is the peak height of the solitary wave, and $\phi > 1$. We then perform an even reflection about the solitary wave center. The difficulty in evaluation of (3.75) arises from the square root singularity in the integrand when $\tilde{u} = A$ and the logarithmic singularity when \tilde{u} is near one. We deal with this by breaking up the integral around these singular points as

$$I = I_1 + I_2 + I_3 \quad (3.76)$$

where

$$I_1 = \int_{\phi}^{\phi+\mu} \frac{d\tilde{u}}{\sqrt{g(\tilde{u})}}, \quad I_2 = \int_{\phi+\mu}^{A-\epsilon} \frac{d\tilde{u}}{\sqrt{g(\tilde{u})}}, \quad I_3 = \int_{A-\epsilon}^A \frac{d\tilde{u}}{\sqrt{g(\tilde{u})}}, \quad (3.77)$$

and $\mu > 0, \epsilon > 0$ are small and to be chosen. We evaluate I_1 and I_3 using Taylor expansions up to first order and calculate I_2 via standard numerical quadrature. The parameters μ and ϵ are chosen so that the approximate error in evaluation of I_1 , I_2 , and I_3 are less than some desired level of tolerance, `tol`. Errors in I_1 and I_3 are due to the local Taylor expansion near the singularities. The errors in I_2 are due to the loss of significant digits in floating point arithmetic.

For $0 < \tilde{u} + \mu - 1 \ll 1$, the approximate rounding error in I_2 is

$$fl\left(\frac{1}{\sqrt{g(\tilde{u} + \mu)}}\right) \approx \left(\frac{1}{2}g''(1)\right)^{-\frac{1}{2}}(\tilde{u} + \mu - 1 + \epsilon_{\text{mach}})^{-1}, \quad (3.78)$$

where $fl(x)$ represents the evaluation of x in floating point arithmetic and ϵ_{mach} is machine precision ($\approx 2.2 \times 10^{-16}$ in double precision). To constrain the error so that it is less than `tol`, we require

$$\mu > \left(\frac{\epsilon_{\text{mach}}}{\text{tol} (2g''(1))^{\frac{1}{2}}}\right)^{\frac{1}{2}} - \tilde{u} - 1, \quad (3.79)$$

and

$$\epsilon > \frac{A \epsilon_{\text{mach}}}{2 (-g'(A))^{\frac{1}{2}} \text{tol}}. \quad (3.80)$$

To evaluate I_1 , we utilize a first order Taylor expansion of $g(\tilde{u})$ near $\tilde{u} = 1$, which gives

$$I_1 \approx \left(\frac{1}{2} g''(1) \right)^{-\frac{1}{2}} \left[\ln \left(\frac{\tilde{u} + \mu - 1}{\tilde{u} - 1} \right) - \frac{\mu g'''(1)}{6g''(1)} \right]. \quad (3.81)$$

Then if we take the second term to be the approximate error and require it be less in magnitude than `tol`, we find a second restriction on μ

$$\mu < \frac{6\sqrt{2} |g''(1)|^{\frac{3}{2}} \text{tol}}{|g'''(1)|}. \quad (3.82)$$

A similar procedure for I_3 leads to

$$\epsilon < \left(\frac{6(-g'(A)) \text{tol}}{g''(A)} \right)^{\frac{2}{3}}. \quad (3.83)$$

Hence, we choose ϵ and μ such that

$$\epsilon = \frac{A \epsilon_{\text{mach}}}{2(-g'(A))^{\frac{1}{2}} \text{tol}}, \quad (3.84)$$

and

$$\mu = \max \left\{ 0, \left(\frac{\epsilon_{\text{mach}}}{\text{tol} (2g''(1))^{\frac{1}{2}}} \right)^{\frac{1}{2}} - u - 1 \right\}. \quad (3.85)$$

We chose `tol` = 10^{-7} and found this to give a sufficiently accurate solitary wave profile. Using this as an initial condition, we initiate our magma equation solver for a solitary wave of height twice the background and a time evolution of approximately 10 dimensionless units. We ran successive simulations for a range of decreasing Δz values and Δt chosen as described above (note that simulations of fixed Δz and a variable Δt showed that the spatial grid was the dominant source of numerical error). The convergence of the numerical error is described by figure 3.10, where the solution converges at sixth order as expected. Note that there is an alternative method for numerically calculating solitary wave solutions to eq. (3.1) for arbitrary n, m in all dimensions [102].

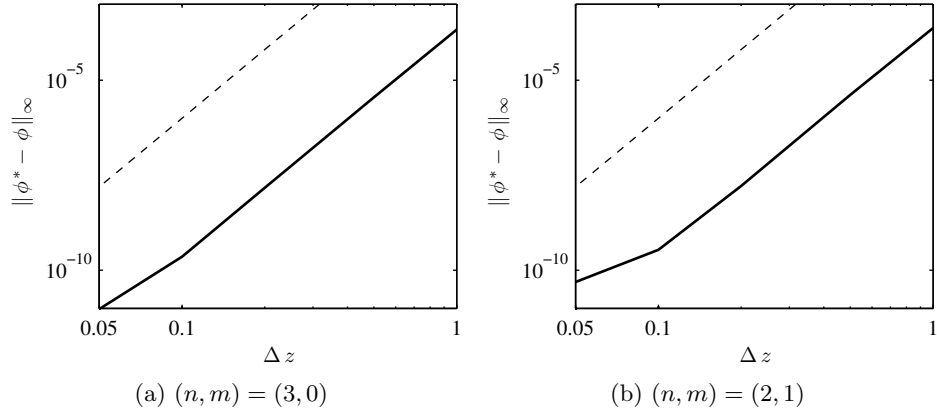


Figure 3.10: Convergence plots of the ∞ -norm of the difference of the numerically evolved solitary wave versus the true solution. In both cases, the time discretization Δt is fixed and we vary Δz . The dotted lines indicate the desired sixth order convergence.

Based on these solitary wave validation studies, we typically use the conservative value $\Delta z = 0.05$, though coarser grids were taken in small amplitude cases where the solutions exhibited longer wavelength oscillations and had to propagate for much longer times. The final time t_f depended upon the jump ϕ_+ , with t_f typically at least 1000 for smaller jumps and $t_f \approx 200$ for larger jumps.

To calculate the leading edge speed s_+ and its amplitude a_+ , we generally consider the long time numerical simulations for the last two dimensionless units of time. We then find the maximum at each fixed time and locally interpolate the discrete porosity function on a grid with spacing $10^{-4}\Delta z$. This ensures we find the “true” numerical maximum and not just the highest point on the grid. We then recompute the maximum of the interpolated porosities, and the value at the final time is the amplitude a_+ . To find s_+ , we compute the slope of the least squares linear fit to the function connecting the positions of the interpolated porosity maxima versus their respective times. This is the leading edge speed.

Chapter 4

Simple Wave DSW Admissibility for Scalar Equations

The criteria for breakdown of the simple wave assumption required for validity of the Whitham-El modulation theory [24], introduced in the previous chapter for the magma equation, are generalizable to a broad class of scalar, third-order, nonlinear dispersive PDEs. Here we present four new admissibility criteria for the Whitham-El method [69]. Similar conditions have also recently been identified for application of the method for a class of bidirectional dispersive hydrodynamic systems [47].

Consider a nonlinear, dispersive, scalar PDE of the form

$$\phi_t + f(\phi)_x = (D[\phi])_x, \quad (4.1)$$

where D_x is a third-order dispersion operator such that eq. (4.1) admits the real-valued linear dispersion relation $\omega = \omega(k, \Phi)$, where k is the wavenumber and Φ is the background constant state about which the system is linearized. Here we assume that for small k , i.e. for long waves, the dispersion sign is negative, $\partial^2 \omega / \partial k^2 < 0$, at least for k sufficiently small. This means we consider solitary wave-led DSWs here for ease of presentation, though similar criteria hold in

either case, with only changes in signs of inequalities. The equation must also admit a periodic traveling wave solution with soliton and harmonic limits, as well as one additional, independent conservation law from the equation (4.1) itself. Along with the conservation of waves equation, this yields three independent conservation laws, as required by the Whitham-El procedure. Finally, we assume the flux function in the dispersionless limit is convex, i.e. $f''(\phi) \neq 0$, for the parameter space of interest.

Recall that the DSW modulation theory under consideration is applicable for step initial data, here taken without loss of generality to be centered about the $x = 0$ axis, of the form

$$\phi(x, 0) = \begin{cases} \phi_- , & x < 0 \\ \phi_+ , & x \geq 0 \end{cases} . \quad (4.2)$$

We assume ϕ_{\pm} are real-valued scalars which satisfy $f'(\phi_-) > f'(\phi_+)$ so that wave breaking occurs. Applying modulation theory [125], the shock interior is described by a system of three quasi-linear conservation laws, the Whitham equations, which can be written

$$\mathbf{q}_T + A(\mathbf{q})\mathbf{q}_X = 0 , \quad (4.3)$$

where $T = \epsilon t$, $X = \epsilon x$, $0 < \epsilon \ll 1$ and $A(\mathbf{q})$ is a real, 3×3 matrix with real eigenvalues $\lambda_i(\mathbf{q})$ and associated right eigenvectors $\mathbf{r}_i(\mathbf{q})$. Note that here we formally introduce the small parameter ϵ to rescale the time and space variables, but this is equivalent to considering long time and space. If A has complex eigenvalues, the Whitham equations are of elliptic type and the system possesses a modulational instability, cf. the case of the modulation equations for the focusing nonlinear Schrödinger equation [32]. The modulation system variables \mathbf{q} are taken to be the physical wave variables describing the single-phase periodic wave solution,

$$\mathbf{q} = \mathbf{q}(X, T) = [\bar{\phi} , k , a]^T , \quad (4.4)$$

for a wave of amplitude a , wavenumber k , and mean height $\bar{\phi}$. The average $\bar{\phi}$ is taken to be the average value of the periodic wave over one wavelength. The GP boundary conditions for the linear wave edge \mathbf{q}_- and solitary wave edge \mathbf{q}_+ are, respectively,

$$\mathbf{q}_- = [\phi_-, k_-, 0]^T, \quad \mathbf{q}_+ = [\phi_+, 0, a_+]^T. \quad (4.5)$$

Note that (4.3) is invariant under the variable rescaling $\tilde{X} = bX$, $\tilde{T} = bT$ for any nonzero scalar b . Given this scaling symmetry, it is natural to look for a self-similar solution of the form $\mathbf{q}(X, T) = \mathbf{q}(\xi)$, $\xi = \frac{X}{T}$ since solutions of this form preserve the symmetry of the original system and the step initial data.

Substituting $\mathbf{q}(\xi)$ into (4.3) leads to

$$A(\mathbf{q}) \mathbf{q}' = \xi \mathbf{q}', \quad (4.6)$$

where $'$ indicates differentiation with respect to the self-similar variable ξ . Hence, this relationship is satisfied if there exists a scalar $\alpha(\mathbf{q})$ such that $(\mathbf{q})' = \alpha(\mathbf{q})\mathbf{r}_i(\mathbf{q})$ for some i and $\xi = \lambda_i(\mathbf{q})$. Now let $(\mathbf{q})' = \alpha(\mathbf{q})\mathbf{r}$ and $\lambda(\mathbf{q}) = \xi$. We need to find $\alpha(\mathbf{q})$. Differentiating the expression $\lambda(\mathbf{q}) = \xi$ with respect to ξ gives $1 = \nabla\lambda \cdot (\mathbf{q})'$, where the gradient is taken with respect to \mathbf{q} . Then substituting $\mathbf{q}' = \alpha\mathbf{r}$ into the previous expression yields

$$\alpha(\mathbf{q}) = \frac{1}{\nabla\lambda \cdot \mathbf{r}(\mathbf{q})} \quad (4.7)$$

which holds only if $\nabla\lambda \cdot \mathbf{r}(\mathbf{q})$ is nonzero. Then if $\nabla\lambda \cdot \mathbf{r} \neq 0$ for all (λ, \mathbf{r}) pairs, we say the conservation system is genuinely nonlinear (cf. [64]). We observe that $\lambda(\mathbf{q}) = \xi$ implies that the characteristic speed λ must vary monotonically as the integral curve is traversed by any scalar which parameterizes the integral curve connecting the left and right states of the shock interior. Verifying genuine nonlinearity can be done by taking a total derivative of the eigenvalue with respect to the parameterization. Note that strict hyperbolicity is also assumed in the construction

of the simple wave solution, i.e. $\lambda_1 < \lambda_2 < \lambda_3$ and all eigenvalues are real. Nonstrict hyperbolicity ($\lambda_i = \lambda_{i+1}$ for some i) implies linear degeneracy ($\nabla \lambda_i \cdot \mathbf{r}_i = 0$) [22]. The requirements of strict hyperbolicity and genuine nonlinearity are necessary conditions to maintain the monotonicity requirement for the existence of a self-similar, simple wave. A simple wave corresponds to a self-similar solution with variation in only one characteristic field. Linear degeneracy or nonstrict hyperbolicity leads to more complexity, i.e. self-similar variation in multiple characteristic fields, see, e.g., [53]. Now we have the simple wave solution for the full modulation system in terms of an eigenvector $\mathbf{r}(\mathbf{q})$ and eigenvalue λ

$$(\mathbf{q})' = \frac{r(\mathbf{q})}{\nabla \lambda \cdot \mathbf{r}(\mathbf{q})} . \quad (4.8)$$

The above discussion holds for quasi-linear hyperbolic systems in general, but we want to apply this theory to the simple wave closure method for DSWs to understand what criteria must be satisfied. Recalling the previous chapter, the difficulty in the study of DSWs for general equations of the form (4.1) is that the resulting modulation system (4.3) is not diagonalizable. Further, the Whitham-El method is meant to subvert the difficulty of explicitly constructing the matrix $A(\mathbf{q})$, so we wish to find easily verifiable criteria for the breakdown of the method using only information from the two distinguished limits of the linear and solitary wave edges. We focus our efforts here on the linear edge limit and present the analogous results for the solitary wave limit, as the arguments follow similarly. In the linear edge, $a = 0$, limit, the modulation system becomes (using the same notation from the previous chapter),

$$\begin{bmatrix} \bar{\phi} \\ k \end{bmatrix}_T + \begin{bmatrix} f'(\bar{\phi}) & 0 \\ \partial\omega/\partial\bar{\phi} & \partial\omega/\partial k \end{bmatrix} \begin{bmatrix} \bar{\phi} \\ k \end{bmatrix}_X = 0 . \quad (4.9)$$

From [24], we know the eigenvalue/eigenvector pair corresponding to the DSW simple wave

solution (namely, the middle characteristic of the full modulation system) is

$$\lambda = \frac{\partial \omega}{\partial k} , \quad \mathbf{r} = [0, 1]^T . \quad (4.10)$$

Further, we know that the relevant integral curve which connects the linear wave and solitary wave edges of the DSW can be obtained by left multiplying eq. (4.9) by the left eigenvector associated with the group velocity eigenvalue and looking for a solution of the form $k = k(\bar{\phi})$. Hence, the integral curve can be parameterized by $\bar{\phi}$.

From eq. (4.8), we see that the simple wave solution for the linear edge modulation system satisfies

$$\bar{\phi}' = 0 , \quad k' = \frac{1}{\partial^2 \omega / \partial k^2} . \quad (4.11)$$

Then if $\partial^2 \omega / \partial k^2 \rightarrow 0$ near $k(\phi_-) = k_-$, i.e. if the sign of dispersion changes for some distinguished wavenumber as we observed for the magma equation, then the modulation system undergoes gradient catastrophe, a phenomenon described in the previous chapter as DSW implosion. Hence for solitary wave led DSWs, implosion occurs if

$$\left. \frac{\partial^2 \omega}{\partial k^2} \right|_{\bar{\phi}=\phi_-, k=k_-} \geq 0 . \quad (4.12)$$

The identification of DSW implosion with a change in the dispersion sign (4.12) is a natural extension to nonlinear waves of the criterion associated with the formation of caustics in modulated linear wave theory [85].

We also require genuine nonlinearity to hold in the full system of modulation equations across the entire DSW region. This can be verified in the neighborhood of the trailing edge system. Genuine nonlinearity requires that the characteristic speed λ for the full modulation system, which reduces to the linear wave group velocity near the linear edge, varies monotonically across the shock region. By parameterizing the shock region by $\bar{\phi}$, we see that we can verify this criterion near the linear edge for solitary wave led DSWs (speed must increase across the shock

region from left to right, where $\bar{\phi}$ decreases) by determining if

$$\left. \frac{d\lambda}{d\bar{\phi}} \right|_{q \rightarrow q_-} = \frac{\partial \lambda}{\partial k} k' + \frac{\partial \lambda}{\partial \bar{\phi}} + \frac{\partial \lambda}{\partial a} a' \Big|_{q \rightarrow q_-} < 0 , \quad (4.13)$$

where ' here indicates differentiation with respect to $\bar{\phi}$. Recalling that the group velocity in the weakly nonlinear limit is an even function of the amplitude, e.g. [66, 126], $\partial \lambda / \partial a \rightarrow 0$. Then the condition for loss of genuine nonlinearity in the full modulation system, as verified at the trailing edge by eq. (4.13), becomes

$$\frac{\partial^2 \omega}{\partial k^2} \frac{dk}{d\bar{\phi}} + \frac{\partial^2 \omega}{\partial k \partial \bar{\phi}} \Big|_{(k=k_-, \bar{\phi}=\phi_-)} \geq 0 , \quad (4.14)$$

where $dk/d\bar{\phi}$ is the characteristic ODE for the integral curve from [24] given by

$$\frac{dk}{d\bar{\phi}} = \frac{\partial \omega / \partial \bar{\phi}}{f'(\bar{\phi}) - \partial \omega / \partial k} . \quad (4.15)$$

Similar arguments for the solitary wave limit of the full modulation system yield the criterion leading to implosion, in terms of the conjugate variables introduced in the previous chapter,

$$\frac{\partial}{\partial \tilde{k}} \left(\frac{\tilde{\omega}}{\tilde{k}} \right) \leq 0 . \quad (4.16)$$

Recall that while the trailing edge is described by a packet of nearly linear waves propagating at the group velocity, the leading edge limit is defined by a solitary wave which propagates with a phase speed. Similarly, loss of genuine nonlinearity of the full modulation system is realized in the leading edge when

$$\frac{\partial}{\partial \tilde{k}} \left(\frac{\tilde{\omega}}{\tilde{k}} \right) \frac{d\tilde{k}}{d\bar{\phi}} + \frac{\partial}{\partial \bar{\phi}} \left(\frac{\tilde{\omega}}{\tilde{k}} \right) \Big|_{\tilde{k}=\tilde{k}_+, \bar{\phi}=\phi_+} \leq 0, \quad (4.17)$$

where

$$\frac{d\tilde{k}}{d\bar{\phi}} = \frac{\partial \tilde{\omega} / \partial \bar{\phi}}{f'(\bar{\phi}) - \partial \tilde{\omega} / \partial \tilde{k}} . \quad (4.18)$$

While the criteria (4.12),(4.14),(4.16),(4.17) are relatively simple expressions to evaluate, there remains the question of whether the distinguished wavenumber or conjugate wavenumber is actually realized by the modulation system for a combination of upstream and downstream states ϕ_{\pm} . Motivated by the previous chapter, in which we observed that DSW implosion could be predicted by identifying a global minimum in the trailing edge speed curve when plotted as a function of the variable upstream ϕ_+ , we find that each of the breakdown criteria can be verified graphically by plotting an appropriate DSW speed curve.

Consider the analysis of the previous chapter, where we fixed the upstream jump height ϕ_- and varied the downstream ϕ_+ . First, recall that the speeds are given by

$$s_-(\phi_+, \phi_-) = \frac{\partial \omega}{\partial k} (k(\bar{\phi}; \phi_+), \bar{\phi}) \Big|_{\bar{\phi}=\phi_-}, \quad s_+(\phi_+, \phi_-) = \frac{\tilde{\omega}}{\tilde{k}} (\tilde{k}(\bar{\phi}; \phi_-), \bar{\phi}) \Big|_{\bar{\phi}=\phi_+}, \quad (4.19)$$

where $k(\bar{\phi}; \phi_+)$ indicates that the wavenumber is found by the solution of the characteristic ODE, parameterized by a variable initial condition and similarly for the conjugate wavenumber, though with a fixed initial condition. Then differentiating the two speeds, s_{\pm} with respect to ϕ_+ , yields

$$\frac{\partial s_-}{\partial \phi_+} = -\frac{\partial^2 \omega}{\partial k^2} \frac{dk}{d\bar{\phi}} \Big|_{\bar{\phi}=\phi_-}, \quad \frac{\partial s_+}{\partial \phi_+} = \frac{\partial}{\partial \tilde{k}} \left(\frac{\tilde{\omega}}{\tilde{k}} \right) \frac{d\tilde{k}}{d\bar{\phi}} + \frac{\partial}{\partial \bar{\phi}} \left(\frac{\tilde{\omega}}{\tilde{k}} \right) \Big|_{\bar{\phi}=\phi_+}. \quad (4.20)$$

Therefore, extrema in these speed curves correspond exactly to the criteria for DSW implosion and loss of genuine nonlinearity, realized in the trailing and leading edges, respectively. In the case where we fix the downstream ϕ_+ and vary the upstream ϕ_- , we find that an extremum in the trailing edge speed curve $s_-(\phi_+, \phi_-)$ corresponds to loss of genuine nonlinearity, and an extremum in the leading edge speed curve $s_+(\phi_+, \phi_-)$ corresponds to zero conjugate dispersion. Hence, there are simple graphical criteria which allow one to identify breakdown of the Whitham-El modulation theory for loss of genuine nonlinearity and DSW implosion. We now provide a brief summary of the results, applicable to both positive and negative dispersion cases.

The criteria put forth by [24] for admissibility of the Whitham-El DSW closure method were

generalizations of the Lax entropy conditions for classical shocks, in requiring that information is transferred into the shock region, defined by the characteristic speed s_- in the trailing edge and s_+ in the leading edge. For general equations of the form (4.1), these can be written in the following manner:

1. $s_- < s_+$

This chooses the orientation of the DSW.

2. $s_- < c(\phi_-)$ and $s_+ > c(\phi_+)$, where $c(\phi) = f'(\phi)$ is the linear wave speed

This ensures the characteristics of the external dispersionless limit impinge on the internal DSW characteristics.

Based on the discussion in this chapter, we add the following criteria which are necessary for the self-similar simple wave assumption required by the modulation construction:

1. $\frac{\partial^2 \omega}{\partial k^2} (k(\bar{\phi}), \bar{\phi}) \Big|_{(k_-, \phi_-)} \neq 0$ or $\partial s_- / \partial \phi_+ \neq 0$,
2. $\frac{\partial}{\partial k} \left[\frac{\tilde{\omega}_s}{\tilde{k}(\bar{\phi})} \right] \left(\tilde{k}(\bar{\phi}), \bar{\phi} \right) \Big|_{(\tilde{k}_+, \phi_+)} \neq 0$ or $\partial s_+ / \partial \phi_- \neq 0$.

These two criteria prevent gradient catastrophe in the system of modulation equations.

3. $\frac{d}{d\phi} \left[\frac{\partial}{\partial k} \omega_0(k(\bar{\phi}), \bar{\phi}) \right] \Big|_{(k_-, \phi_-)} \neq 0$ or $\partial s_+ / \partial \phi_+ \neq 0$,
4. $\frac{d}{d\phi} \left[\frac{\tilde{\omega}_s(\tilde{k}(\bar{\phi}), \bar{\phi})}{\tilde{k}(\bar{\phi})} \right] \Big|_{(\tilde{k}_+, \phi_+)} \neq 0$ or $\partial s_- / \partial \phi_- \neq 0$

These two conditions indicate a breakdown in genuine nonlinearity of the full 3×3 modulation system.

Chapter 5

Experiments on Large Amplitude Solitary Wave Interactions in Viscous Fluid Conduits

Up to this point, we have presented the theoretical basis for understanding nonlinear wave phenomena arising in the viscous fluid conduit setting, a validated numerical solver for the conduit equation and its generalization, and the appropriate relations between the physical parameters which must hold for laboratory studies of the full system. Previous experimental studies have provided validation of the theoretical amplitude-speed relation for single and interacting solitary waves. Here we add to the conduit experimental literature, as well as to the mathematical solitary wave community, by considering the geometry of the wave complex formed at the height of a two solitary wave interaction. The contents of this chapter are based on a manuscript which has been submitted for peer review [71]:

Lowman, N. K., Hoefer, M. A., and El, G. A. (2013) “Interactions of large amplitude solitary waves in viscous fluid conduits,” *under consideration for publication by the Journal of Fluid Mechanics*.

5.1 Abstract

The free interface separating an exterior, viscous fluid from an intrusive conduit of buoyant, less viscous fluid is known to support strongly nonlinear solitary waves due to a balance between viscosity-induced dispersion and buoyancy-induced nonlinearity. The overtaking, pairwise interaction of weakly nonlinear solitary waves has been classified theoretically for the Korteweg-de Vries equation and experimentally in the context of shallow water waves, but a theoretical and experimental classification of strongly nonlinear solitary wave interactions is lacking. The interactions of large amplitude solitary waves in viscous fluid conduits, a model physical system for the study of one-dimensional, truly dissipationless, dispersive nonlinear waves, are classified. Using a combined numerical and experimental approach, three classes of nonlinear interaction behavior are identified: purely bimodal, purely unimodal, and a mixed type. The magnitude of the dispersive radiation due to solitary wave interactions is quantified numerically and observed to be beyond the sensitivity of our experiments, suggesting that conduit solitary waves behave as “physical solitons.” Experimental data are shown to be in excellent agreement with numerical simulations of the reduced model. Experimental movies are available with the online version of the paper.

5.2 Introduction

Exponentially localized solitary waves arise in nature as a balance between the steepening effects of nonlinearity and the spreading effects of dispersion. These fundamental, nonlinear coherent structures exhibit an amplitude-dependent phase speed, often with larger waves propagating faster than slower ones, e.g. [126]. A distinguishing feature of solitary waves in one-dimension is the nature of the resulting interaction when a larger, trailing solitary wave overtakes a smaller, leading wave, a scenario sometimes referred to as strong interaction of solitary waves [78]. A classical model of weakly nonlinear solitary wave interactions is the Korteweg de-Vries (KdV) equation. Unlike in the case of linear waves, where superposition applies, the nonlinear interaction

is characterized by the larger wave decreasing in height and experiencing a forward shift in position, while the smaller solitary wave increases in amplitude and experiences a negative position shift [128]. The two solitary waves then emerge from the interaction with their initial profiles and speeds restored. The absence of interaction-induced radiation is associated with mathematical solitons and complete integrability of the governing equation, as is the case for KdV. The exact two soliton KdV solution was derived [44] and the soliton overtaking interaction has been classified by amplitude ratio into three distinct regimes according to the qualitative structure during the interaction [59]. When the ratio of the trailing and leading amplitudes is sufficiently small, a bimodal structure persists through the interaction with the trailing wave passing its mass forward to the leading wave. When the ratio is large, the interaction is unimodal, with the larger wave engulfing the smaller one before emitting it. For intermediate ratios, there is a hybrid state, in which the interaction begins with the larger wave absorbing the smaller one and forming an asymmetric, unimodal mass. During the peak of the interaction, a distinctly bimodal wave appears before the process undoes itself (see Fig. 5.2 for images of each interaction type in the context of the model equation considered here). This classification scheme for KdV depends solely on the ratio of the soliton amplitudes due to the existence of scaling and Galilean symmetries. It has been confirmed experimentally in the case of weakly nonlinear, shallow water waves [120, 21, 65]. Due to a capillary instability and small dissipation, solitary water waves are limited to nondimensional amplitudes less than 0.78 [114, 3], thus water waves are a limited system in which to probe large amplitude, conservative solitary wave interactions. Moreover, experiments and numerical simulations of the water wave equations accessed amplitudes only up to 0.4 [21]. Thus, to the authors' knowledge, a systematic, quantitative classification of strongly nonlinear solitary wave interaction behaviors in any physical system is lacking experimentally and theoretically.

In this work, we extend the classification of overtaking interactions of solitary waves to a nonintegrable, strongly nonlinear, dissipationless/dispersive wave equation, the so-called conduit equation, cf. [68] and to experiments involving solitary wave interactions with nondimensional

amplitudes up to ~ 14 . The conduit equation arises in the study of viscous fluid conduits, a medium in which solitary waves have been studied experimentally in isolation [99, 83] and post-interaction [43], but not during the interaction process. The viscous fluid conduit setting is realized by introducing a steady source of buoyant, viscous fluid to a quiescent medium of heavier, more viscous fluid. A stable, fluid-filled pipe is formed. Slow changes in the rate of injection induce interfacial dynamics involving a maximal balance between buoyancy of the intrusive fluid and the resistance to motion by the exterior fluid (see Fig. 5.1). The scalar, nonlinear, dispersive conduit equation capturing the interfacial dynamics has been derived from the full set of coupled fluid equations [68]. Unlike well-known models of small amplitude, weakly nonlinear, interfacial fluid dynamics such as the KdV [57] and Benjamin-Ono [10, 84] equations, the conduit equation is derived under long wave assumptions only, valid for large amplitudes [68], much like the Green-Naghdi (or Serre, Su-Gardner) equations of large amplitude, shallow water waves [101, 112, 38]. Moreover, large amplitude conduit solitary waves are asymptotically stable [105], exhibit good agreement with experiments [99, 83, 43], and are robust, physical features of viscous fluid conduit interfacial dynamics.

Using careful numerical simulations, we find that although the conduit equation does not possess the KdV Galilean invariance, the qualitative Lax classification scheme from KdV theory extends to the strongly nonlinear regime for physically realizable solitary wave amplitudes. The type of interaction depends on the absolute amplitudes of the two waves, rather than solely on their ratio. A scaling invariance of the conduit equation renders a unit solitary wave background but cannot be used to scale individual solitary wave amplitudes. Our numerical computations demonstrate small energy loss (10^{-2} relative change in the solitary wave two-norm) due to interaction, also numerically observed in a closely related equation [7]. This confirms the non-integrability of the conduit equation, as shown by the Painlevé test [42]. However, any dispersive radiation following experimental solitary wave interaction was below the resolution of our imaging system, a feature also observed in previous experiments [43]. This suggests that while not *mathematical* solitons, conduit solitary waves are *physical* solitons. We support these

numerical observations with quantitative interaction classification experiments, which are in excellent agreement and represent the first observations of the mixed and unimodal interaction types in viscous fluid conduits.

The importance of this work extends beyond the remarkable agreement between theoretical and numerical predictions of conduit solitary wave dynamics and our experimental observations. In particular, the overtaking interaction between two solitary waves can be seen as a fundamental property of one-dimensional, dissipationless, dispersive hydrodynamics. As such, these observations further establish the viscous fluid conduit setting as a practically accessible experimental and theoretical platform for future investigations into solitary waves, slowly modulated nonlinear wavetrains, and their interactions, for which quantitative experiments in any physical system are essentially lacking in the literature. Moreover, the fact that we do not observe qualitatively new behaviors in the interactions of solitary waves beyond the weakly nonlinear regime is highly nontrivial due to the lack of integrability and the increased dimensionality of the parameter space. This suggests there could be some robustness or universality to the Lax categories for wave equations which asymptotically reduce to KdV. There is also renewed interest in the nature of two soliton interactions in integrable and nearly integrable systems in connection with the theory of soliton gas (or soliton turbulence) [27]. Interactions falling into different Lax categories have distinct effects on the statistical characteristics of soliton turbulence [87], and thus viscous fluid conduits provide a promising setting for the experimental study of statistical properties of incoherent soliton gases.

In the following section, we present the theoretical foundations for the classification of conduit solitary waves and describe the experimental set-up. Section 5.4 presents the details of our findings, and the manuscript is concluded in § 5.5 with a discussion of future directions.

5.3 Theoretical foundations

In this section, we give an overview of the theoretical foundations needed for classifying viscous fluid conduit solitary wave interactions. We provide intuition regarding the physical effects that

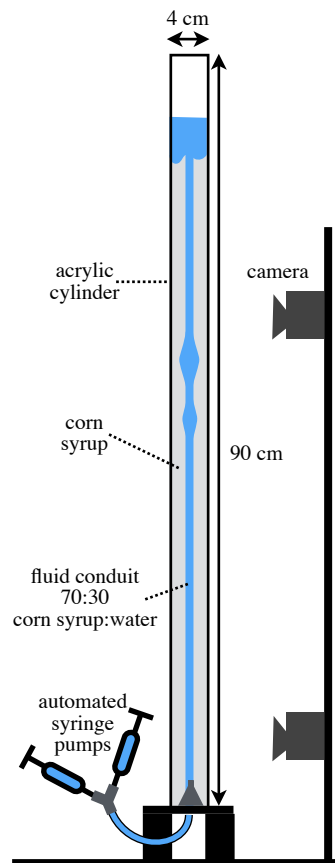


Figure 5.1: Diagram of the fluid conduit experimental system.

give rise to interfacial dynamics, develop relevant numerical tools, and describe the experimental set-up.

5.3.1 Derivation of the conduit equation and solitary wave solutions

A complete mathematical description of the viscous fluid conduit setting requires the consideration of the full system of Navier-Stokes equations for the intrusive and exterior fluids, with boundary conditions along a moving, free interface. To subvert this difficulty, an approximate model governing the interfacial dynamics has been derived from physical principles [83, 99] and via an asymptotic, multiple scales procedure [68] using the ratio of the viscosities as the small parameter,

$$\epsilon = \mu^{(i)}/\mu^{(e)} \ll 1, \quad (5.1)$$

where $\mu^{(i)}$ indicates the (dynamic) viscosity of the intrusive fluid and $\mu^{(e)}$ that of the exterior fluid. Here we outline the asymptotic derivation and identify the additional key nondimensional quantities and assumptions required to ensure model validity for comparison with experimental parameters.

The steady injection from below of a buoyant, viscous fluid into a basin of a much more viscous fluid evolves to form a vertically uniform, axisymmetric conduit, well-described by the governing equations of Poiseuille-type flow [124]. In this unperturbed setting, the vertical velocity of the intrusive fluid is driven by a vertical pressure gradient due to buoyancy, and the conduit radius is set by the injection rate, assuming the velocity is $\mathcal{O}(\epsilon)$ at the interface. In response to perturbations of the injection rate, radial velocities are excited along the interface, inducing a normal, viscous stress, which balances the pressure difference between the two fluids across the boundary. This dominant balance is satisfied, provided the following assumptions hold: (1) the vertical variation along the conduit wall is small relative to the radial, i.e. the vertical length scale L is large relative to the radius of the unperturbed conduit R_0 ,

$$L = \left(\frac{A_0}{8\pi\epsilon} \right)^{1/2}, \quad A_0 = \pi R_0^2, \quad (5.2)$$

(2) the two fluids are miscible with negligible mass diffusion across the interface, and (3) the Reynolds number of the intrusive fluid, defined to be

$$Re = \frac{\rho^{(i)}UL}{\mu^{(i)}} , \quad U = \frac{gA_0\Delta\rho}{8\pi\mu^{(i)}} , \quad (5.3)$$

for intrusive fluid density $\rho^{(i)}$ and density difference $\Delta\rho = \rho^{(e)} - \rho^{(i)}$, is no larger than $\mathcal{O}(1)$. Under these provisions, the vertical pressure gradient within the conduit has two contributions, one from buoyancy and the other from viscous stress. This leads to the (nondimensional) volumetric flux $Q(z, t)$, with characteristic scale Q_0 , which can be written in terms of the nondimensional conduit cross-sectional area, $A(z, t)$ in the form

$$Q(z, t) = A^2(z, t) \left\{ 1 - \frac{\partial}{\partial z} \left[\frac{1}{A(z, t)} \frac{\partial A(z, t)}{\partial t} \right] \right\} , \quad Q_0 = A_0 U . \quad (5.4)$$

Lastly, the flux is related to the evolution of the conduit area by appealing to the continuity equation and imposing the kinematic boundary condition along the interface, yielding $\partial_t A(z, t) + \partial_z Q(z, t) = 0$, or the conduit equation

$$\frac{\partial A(z, t)}{\partial t} + \frac{\partial}{\partial z} \left(A^2(z, t) \left\{ 1 - \frac{\partial}{\partial z} \left[\frac{1}{A(z, t)} \cdot \frac{\partial A(z, t)}{\partial t} \right] \right\} \right) = 0 . \quad (5.5)$$

The conduit equation can be approximated by the KdV equation in the small amplitude, long wavelength regime [?]. A key result for the present study is that eq. (5.5) is valid for long times, $t = o(\epsilon^{-1})$ and large amplitudes $A = o(\epsilon^{-1})$, provided the aforementioned assumptions are satisfied and ϵ is sufficiently small [68].

Conduit solitary waves, first considered by [97], are derived by introducing the ansatz $A(z, t) = A(\zeta)$, $\zeta = z - ct$, where c is the wave speed and A decays exponentially to a background constant, here taken to be unity without loss of generality. Inserting this form of the solution into eq. (5.5) and integrating twice yields the ordinary differential equation (ODE)

defining the solitary wave profile $A(\zeta)$,

$$\begin{aligned}\alpha_0 \left(\frac{dA}{d\zeta} \right)^2 &= \alpha_1 + \alpha_2 A + \alpha_3 A^2 + \alpha_4 A^2 \ln A , \\ \alpha_0 &= \frac{1}{2} (2A_s^2 \ln A_s - A_s^2 + 1) , \quad \alpha_1 = A_s^2 \ln A_s - A_s^2 + A_s , \quad \alpha_2 = -2\alpha_0 , \\ \alpha_3 &= A_s^2 \ln A_s - A_s + 1 , \quad \alpha_4 = -(A_s^2 - 2A_s + 1) ,\end{aligned}\tag{5.6}$$

where A_s is the total *height* of the solitary wave, i.e. background plus amplitude, and the amplitude-speed relation is given by

$$c(A_s) = \frac{2A_s^2 \ln A_s - A_s^2 + 1}{A_s^2 - 2A_s + 1} .\tag{5.7}$$

Note that the speed is monotone increasing in A_s , so larger solitary waves always move faster.

5.3.2 Numerical methods

To study the overtaking interaction of conduit solitary waves, we initialize A in eq. (5.5) with two well-separated solitary waves. The trailing wave has amplitude a_{trail} ($a = A_s - 1$ is the amplitude above the background) and the lead wave has amplitude a_{lead} . We take $a_{\text{trail}} > a_{\text{lead}}$ so that $c_{\text{trail}} > c_{\text{lead}}$. The localized solitary waves are separated initially so that their superposition on a uniform background of unity exhibits small, $\mathcal{O}(10^{-7})$, difference above background. The ODE (5.6) is integrated as in [69] with tolerance below $\mathcal{O}(10^{-7})$. The dynamical solver for (5.5) has been validated in [69]. The width of the truncated spatial domain is chosen so that, at all times, the solitary waves are 10^{-8} close to the background state at the end points. The grid spacing is chosen so that the individual solitary waves are well-resolved, with values selected from the range $\Delta z \in [0.05, 0.5]$, with larger amplitude solitary waves requiring higher resolution. The time step is $\Delta t = \Delta z / 2c_{\text{trail}}$.

5.3.3 Experimental set-up

The experimental apparatus, depicted in Fig. 5.1, used to study conduit solitary waves is an acrylic cylinder with square sides 4 cm by 4 cm and a height of 90 cm, filled to a depth of approximately 75 cm with a generic brand light corn syrup. To ensure miscibility, the intrusive fluid was taken to be a 70:30 mixture of corn syrup and water, with food coloring used for imaging. This set-up closely follows previous experiments by [83, 99, 43]. Injection of the intrusive fluid through the base of the apparatus was precisely controlled by use of an automated syringe pump, with the base injection rate 0.1 mL/min to create a vertically uniform, background conduit. Solitary waves were formed by producing an additional localized pulse in the rate of injection using a second syringe pump, connected to the apparatus via a y-junction, hence affording precision control on the size of the solitary waves generated. Viscosities of the two fluids were measured by a rotational viscometer, with 2% measurement uncertainty. Densities were measured using a scale and graduated cylinder with uncertainty 1%. Nondimensional, solitary wave amplitudes relative to background were measured by counting pixels across the conduit from still frame images captured with a digital SLR camera. The dimensional radius of the background conduit, held constant throughout the experiments, was measured by comparing images of the background conduit with a grid of known size attached to the back wall of the apparatus. To compute the correction due to the projection of the conduit fluid in the middle of the apparatus onto the back wall, the grid was compared with a copy of the same grid submerged within the filled apparatus before injection commenced. Errors due to imaging techniques and measurement were estimated by measuring the diameter of the background conduit across a range of images yielding a standard deviation of 2%, on the order of the viscosity measurements. Interaction classification was achieved by high definition video recording of the interaction using a second camera. Still frames of the interactions were then extracted from the video, and downsampled using bicubic interpolation in the vertical coordinate by a factor of $0.1 \approx \epsilon^{1/2}$ in order to enforce an aspect ratio of 1. Recall the long wavelength scaling in (5.2) sets an aspect ratio of the vertical to radial lengths of order $\epsilon^{-1/2}$. This scaling significantly improves the

Table 5.1: Key experimental parameters.

$\rho^{(i)}$	$\rho^{(e)}$	$\mu^{(i)}$	$\mu^{(e)}$	A_0	U	Re	ϵ
1.23 g/mL	1.37 g/mL	0.789 P	83.6 P	0.017 cm ²	0.118 cm/s	0.049	9.4×10^{-3}

fidelity with which we can classify the solitary wave interaction types. In cases where it was difficult to determine the classification, edge detection algorithms were also used. Measured and derived fluid properties are provided in Table 5.1.

A major difficulty previously encountered during experiments with this system was creating and maintaining a straight, vertical conduit. We find the following protocol to be effective. The injection line is prepared so that a small amount of air is left in the line just ahead of the intrusive fluid. The remaining intrusive fluid has no air bubbles. A well-mixed volume of corn syrup is poured down the side of the cylinder to fill, minimizing the entrainment of air. The apparatus is allowed to equilibrate overnight. The experiment is initiated with steady injection at a rate of 0.5 mL/min. First, controlled air bubbles are produced so that the initial penetration of the intrusive fluid follows behind the air bubbles. This latter protocol is similar to the procedure described in [43]. We find the background conduit to be straight to within 0.2° across 60 cm. It merits mention that the conduit equation (5.5) has been shown to be valid for conduits canted by $\mathcal{O}(6^\circ \approx \epsilon^{1/2} 180^\circ / \pi)$ or less [68], which was not violated here due to our controlled initiation procedure.

5.4 Overtaking interactions between strongly nonlinear solitary waves

Using the theoretical, experimental, and numerical techniques developed in the previous section, we now describe the classification of strongly nonlinear solitary wave interactions in the viscous fluid conduit setting. Long time, high resolution numerical simulations in Fig. 5.2 exhibit the three interaction categories, which are also found experimentally and displayed in a photo

montage in Fig. 5.4. It is further shown that the dispersive tail generated by solitary wave interactions is beyond the sensitivity of our experiments.

5.4.1 Classification of interactions: KdV

In the case of the KdV equation, i.e. the weakly nonlinear, long wavelength regime, properties due to integrability have been used to classify the overtaking interaction analytically into three distinct categories, based solely on amplitude ratio $a_{\text{trail}}/\alpha_L$ [59]:

$$\begin{aligned} 1 < \frac{a_{\text{trail}}}{\alpha_L} < \frac{3 + \sqrt{5}}{2} \approx 2.62 & : \quad \text{bimodal} , \\ \frac{3 + \sqrt{5}}{2} < \frac{a_{\text{trail}}}{\alpha_L} < 3 & : \quad \text{mixed} , \\ \frac{a_{\text{trail}}}{\alpha_L} > 3 & : \quad \text{unimodal} , \end{aligned} \tag{5.8}$$

where a_{trail} and α_L are the trailing and leading soliton amplitudes, respectively for $t \rightarrow -\infty$. A bimodal interaction denotes the case where the wave complex maintains a bimodal structure throughout the interaction. This type of exchange interaction corresponds to a transfer of mass from the larger, trailing solitary wave to the smaller, lead solitary wave. In contrast, unimodal interaction involves the complete fusion of the lead wave by the trailing wave, followed by fission into two waves. The intermediate, mixed-type interaction, which has a limited range of amplitude ratios in the weakly nonlinear case, possesses both qualities, a unimodal structure just before and just after interaction but a distinctly bimodal one at $t = t_i$.

5.4.2 Classification of interactions: conduit equation

The numerical classification of strongly interacting solitary waves is achieved by dynamical evolution of the conduit equation (5.5) given initial data consisting of a large, trailing solitary wave of amplitude a_{trail} , well separated from a smaller, leading solitary wave of amplitude a_{lead} .

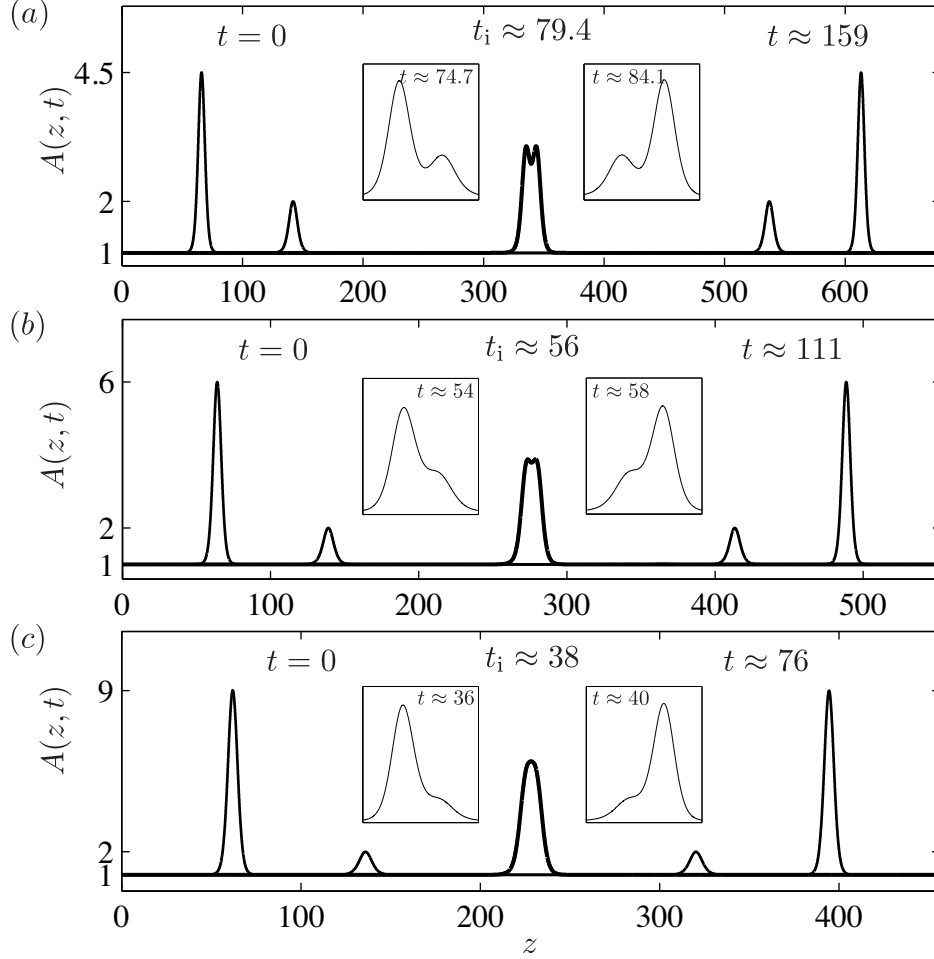


Figure 5.2: Example numerical solutions of the conduit equation eq. (5.5) exhibiting the three types of overtaking interactions. The initial and final states, as well as the solution at the time of peak interaction t_i , are plotted on the spatial axis while the left and right insets correspond to the solution just before and just after the peak interaction. The trailing amplitude is varied, while the leading amplitude is fixed, $a_{\text{lead}} = 1$. (a) Bimodal interaction, $a_{\text{trail}} = 3.5$. (b) Mixed interaction, $a_{\text{trail}} = 5$. (c) Unimodal interaction, $a_{\text{trail}} = 8$.

The geometry of the wave structure near the time of interaction, t_i , defined to be

$$t_i = \arg \min_t \left\{ \max_z [A(z, t)] \right\} , \quad (5.9)$$

is examined. The choice of t_i is due to the nature of the interaction, in which the larger solitary wave decreases in amplitude until $t = t_i$ before asymptotically approaching a_{trail} long after the interaction. This behavior is characteristic of KdV soliton interactions as well.

We allow the two solitary wave initial profiles to evolve long past the time of interaction ($t_{\text{final}} \approx 2t_i$). Once the numerical solution is obtained, the location and height of the two solitary wave maxima are obtained for each time step by interpolating the solution onto a finer grid and examining its derivative to find the local extrema. If only one maximum is found, the structure at that time is considered unimodal. We classify interactions as bimodal if two maxima are present throughout and as unimodal if the interaction possesses only one peak at $t = t_i$. Note that the distinguishing feature of the mixed interaction is the presence of a single maximum just before and after the peak interaction time, but the reemergence of two distinct maxima at $t = t_i$. Example numerical simulations of eq. (5.5) of each type of interaction for a fixed $\alpha_L = 1$ and varying a_{trail} are presented in Fig. 5.2.

The bifurcation diagram in Fig. 5.3 presents the key results of our classification analysis. For a range of leading and trailing amplitude solitary waves, the critical amplitudes marking phase transition are plotted. This was determined by fixing α_L and monotonically varying a_{trail} in increments of $\alpha_L/20$ until the interaction type had transitioned from one type to another for three consecutively larger values of a_{trail} . The critical value then was taken to be the value of a_{trail} midway between the amplitudes corresponding to the last interaction of one type and the first interaction of the new type. The x marks on the dashed vertical line along $\alpha_L = 1$ mark the location of the simulations presented in Fig. 5.2. We find that due to a continuous transition, the precise determination of type I-III requires high resolution simulations.

As pointed out earlier, the behavior of the conduit equation (5.5) is asymptotically equivalent

to KdV in the small amplitude regime, which is captured in the zoomed inset of the phase diagram as the conduit transitions limit on the KdV transitions for sufficiently small $a_{\text{trail}} \lesssim 0.5$. However, in this nonintegrable, strongly nonlinear equation where $2 < a_{\text{trail}} < 15$, the type of interaction depends not on the amplitude ratio, but on the values of both amplitudes. This is due to the existence of three distinct conduit amplitudes, the background and those of the trailing and leading solitary waves. Only one amplitude can be scaled to unity using symmetry of the equation, leaving two other free parameters (cf. [69]).

The complete, mathematical classification of KdV soliton interactions was enabled by an explicit representation of the solution. Here, we do not have this luxury. Like in the integrable setting, though, the structure of the interaction for every amplitude tested in our simulations (which covers most of the physically relevant range) always falls into one of the three types. Moreover, the mixed geometry is expected for a much wider range of amplitudes than in (7.8) as the two initial waves grow larger.

5.4.3 Radiation emitted due to interaction

It is also of physical interest to consider the magnitude of the dispersive tail resulting from interactions of conduit solitary waves, which are not exact solitons. Overtaking interactions of solitary waves in nonintegrable equations have been shown via numerical simulations to produce a small tail of linear dispersive waves following their interaction, e.g. [13, 79, 7], a feature which if sufficiently large, could be examined experimentally. To address this issue, we have run simulations of solitary wave interactions for a fixed $\alpha_L = 1$ and a_{trail} varying between 2 and 8, so that it spans all three interaction types and also corresponds to the experiments in the following section. The radiation was quantified in two ways using long time numerical evolution, $t_{\text{final}} \approx 3t_i$. The first is the change in the amplitudes of the solitary waves post-interaction and the second is the change in the profiles. Here we find the maximum change in amplitudes for both waves is consistently $\mathcal{O}(10^{-3})$. The change in the individual solitary wave profiles is determined by centering a window about each individual wave, for both the initial and final

times, and then determining the residual between the two profiles, here defined by the relative two-norm difference, i.e. two-norm of the residual divided by the initial two-norm. This metric reveals that the change in profiles from before to long after the interaction is not larger than $\mathcal{O}(10^{-2})$ across the simulations examined. These findings are consistent not only with numerical simulations of a closely related equation [7], but also with experimental findings from conduit solitary wave interactions [43]. Moreover, the amplitude differences and residuals are beyond the sensitivity of our experimental capabilities, which suggests that these conduit solitary waves are approximately solitons, at least in a physical sense, hence we term them “physical solitons.”

5.4.4 Experimental observation of the three types of interaction

In Fig. 5.3, we plot the results of twenty-seven solitary wave interaction classification experiments. The three distinct types predicted by numerical simulations of the conduit equation (5.5) are readily observable in the full physical system, and their dependence on a_{lead} and a_{trail} is in excellent agreement with the phase diagram. Example images of an unscaled interaction experiment and then scaled data used for classification are given in Fig. 5.4. While it is sometimes difficult to distinguish between the regimes in the unscaled data, scaling the data recovers the aspect ratio of the nondimensional coordinate system from the numerical simulations and allows for proper determination. Typical examples of the three interaction types are shown. Movies in both unscaled and scaled formats are available with the online version of the paper.

Regarding the agreement with numerical simulations, up to the 2% error in measuring conduit diameters, the data all lie in the appropriate regions of the phase diagram. While this agreement is compelling on its own, it is also possible to compare with the approximate model breakdown criteria identified in [68]. The use of miscible fluids meets the negligible surface tension criterion, and the contributions due to the outer wall are small because the nondimensional radius of the outer wall satisfies $R_{\text{wall}} \approx 76 \gg \epsilon^{-1/2} = 10.3$. The Reynolds number criterion $Re = 0.049 \ll \epsilon^{-1} = 106$ for neglecting inertial effects is also satisfied. Lastly, the breakdown of the multiple scales assumption occurs when the condition, $A \ll 1/8\epsilon \approx 13.3$,

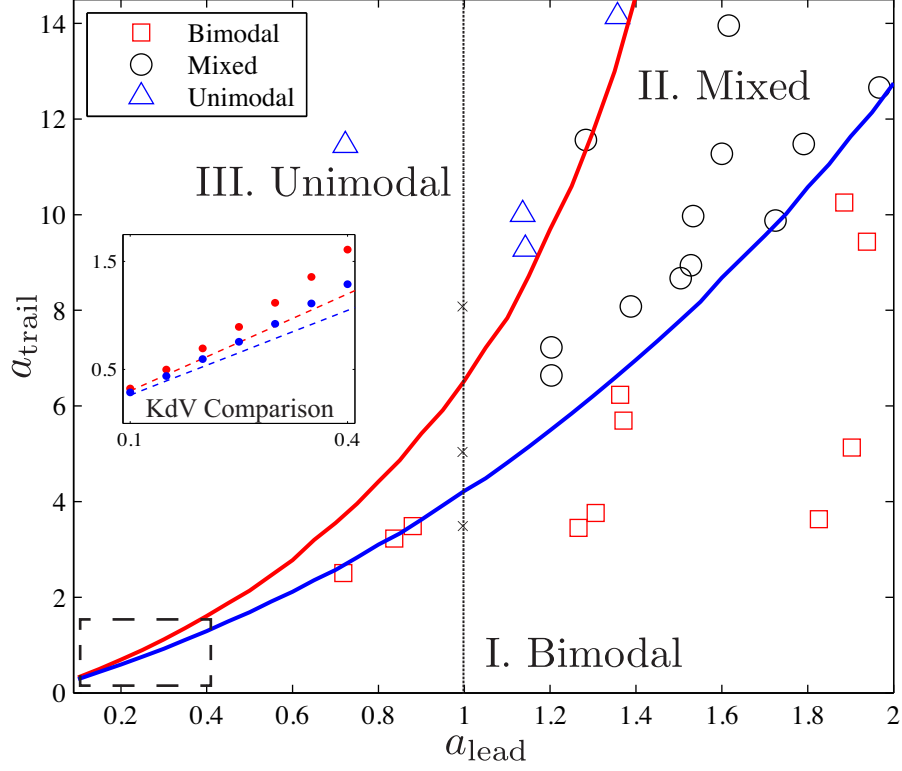


Figure 5.3: Phase diagram of the numerical and experimental classification of the overtaking interaction between two conduit solitary waves as a function of the leading and trailing wave amplitudes. The blue (darker) curve indicates the transition from bimodal interaction to the intermediate/mixed type. The red (lighter) curve marks the transition from the mixed type to unimodal. The inset represents the boxed portion in the weakly nonlinear regime showing convergence to the KdV predictions (dashed lines). Crosses along $a_{\text{lead}} = 1$ correspond to simulations in Fig. 5.2. The geometric shapes correspond to experimental classification.

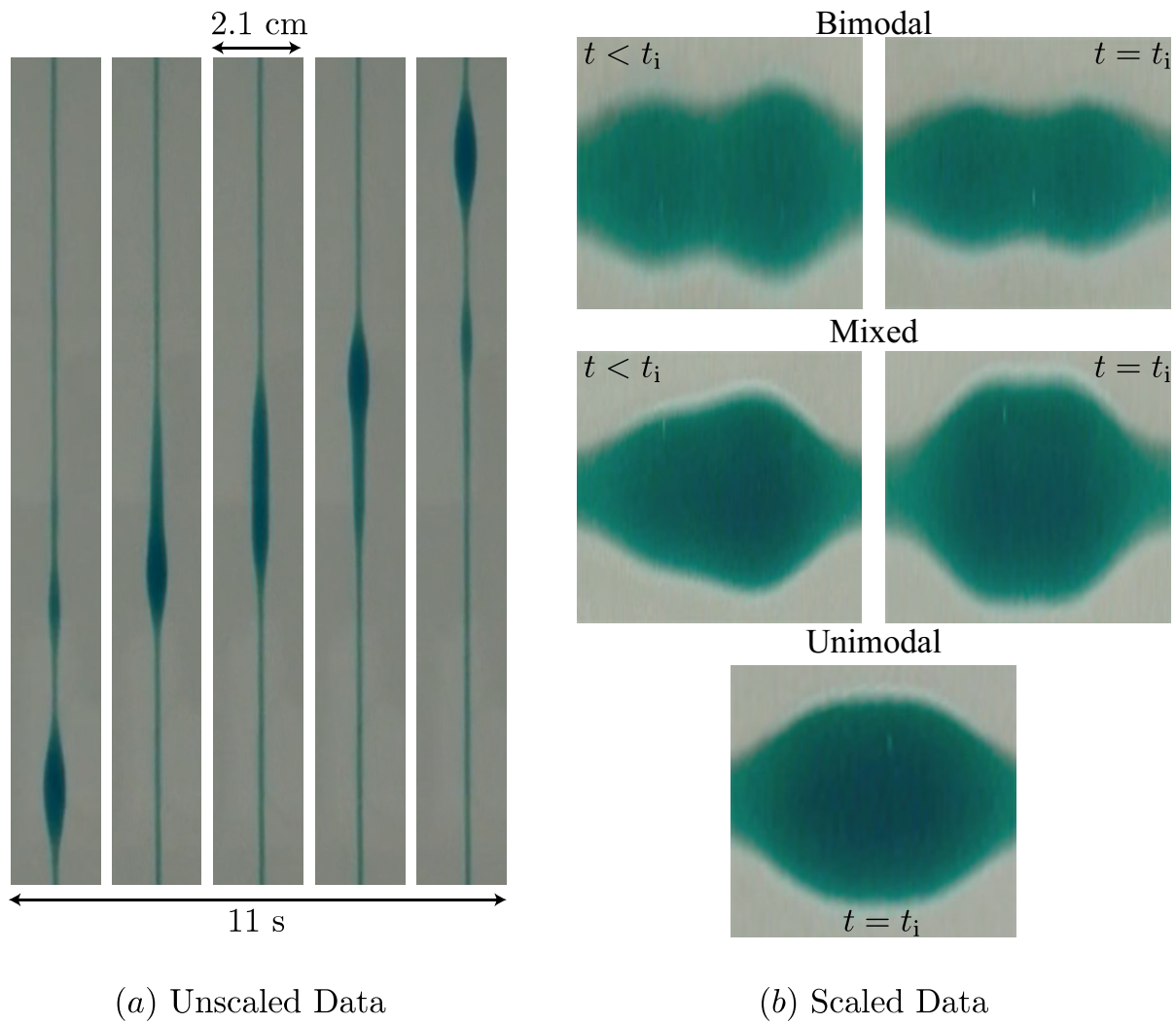


Figure 5.4: Data from interaction experiments. (a) Unscaled data showing the solitary wave profiles from a typical interaction. (b) Examples of the three interaction types for scaled data used in classifications. From top to bottom, $(a_{\text{lead}}, a_{\text{trail}})$ are $(1.27, 3.45)$, $(1.53, 9.97)$, and $(1.14, 10.01)$, respectively. See the online version of the paper for movies of these experiments.

is violated for large amplitude solitary waves [68]. We note that two of the trials lie beyond this point, though they still fall in the appropriate classification region. There exists an independent condition for model validity based on the introduction of inertial effects for sufficiently large amplitude solitary waves, measured by an effective solitary wave Reynolds number [43], but we find the multiple scales condition to be more restrictive in our case. Our results suggest remarkably robust concurrence between the reduced, approximate interfacial equation and the full two-fluid system.

5.5 Summary and conclusions

The qualitative characterization of large amplitude, pairwise solitary wave interactions in viscous fluid conduits has been shown to permit geometric classification according to the three Lax categories for KdV. Unlike the weakly nonlinear regime, however, the expected interaction type depends on the wave amplitudes, rather than only their ratio, and the mixed unimodal/bimodal interaction type is a more robust, readily observable feature than for surface water waves.

The long-time, large amplitude validity of the conduit equation (5.5) and its analytical tractability make this two viscous fluid setting an ideal one for the study of nonlinear dispersive waves. That nonlinear dispersive waves occur at all in a fully viscous setting is a nontrivial observation, but that the reduced equation captures the geometry of interacting solitary waves suggests the interfacial dynamics of viscous fluid conduits are, as predicted, approximately one-dimensional and dissipationless at the time scales under consideration. Moreover, the absence of dispersive radiation in the experiments implies that, while the conduit equation is not completely integrable, its solitary waves practically interact elastically. These results encourage future experimental studies on nonlinear coherent structures, such as rarefaction waves, slowly modulated wavetrains (dispersive shock waves) and their interactions.

Acknowledgements

We thank Karen Daniels, Hien Tran, and the NCSU Department of Mathematics and Center for Research in Scientific Computation for laboratory support. This work was funded by NSF Grant Nos. DGE-1252376, DMS-1008793, and CAREER DMS-1255422.

Chapter 6

Experiments on Dispersive Shock Waves in Viscous Fluid Conduits

The culmination of this dissertation in the context of the viscous fluid conduit setting is the experimental validation of the Whitham-El modulation theory predictions for DSW speeds and leading edge amplitude. Here we present details of the experimental method for studying the shock problem in the full fluid system. We note that the experimental results presented in this chapter are preliminary, and we have plans for ongoing investigations to collect new data. While we acknowledge several sources of experimental error, it should be noted that the nonlinear wave averaging applied to the asymptotic model yields excellent agreement despite the difficulties. To improve upon the results, more trials will be run, and the data collection process will be improved. The contents of this chapter will form the basis of a submission to a peer-reviewed journal.

6.1 Abstract

Shock waves in classical fluids arise when the smoothing effects of viscosity mediate gradient singularity formation, resulting in sharp, localized fronts across which energy is dissipated to

smaller scales. In many quantum hydrodynamical settings – e.g. superfluids, cold plasma, and nonlinear photonics, – the effects of viscosity are negligible and an alternate regularization mechanism exists in which nonlinear steepening is regularized conservatively by the spreading effects of dispersion. While such dispersively regularized shock waves have been identified experimentally and observationally in a number of physical systems, a comprehensive, quantitative characterization of their properties in a controlled laboratory setting is lacking from the literature due to their challenging nature both experimentally and theoretically. Here we present a model system for the careful study of strongly nonlinear, truly dissipationless, dispersive hydrodynamic structures: viscous fluid conduits. Though counterintuitive that the evolution of viscosity-dominated fluids could admit superfluid-like characteristics, we show that this system is both analytically tractable and ideal for high precision, quantitative experiments via a simple, highly repeatable tabletop set-up. This enables us to show agreement between mathematical theory and quantitative measurements of the speed and amplitude for the dispersive shock wave front across a range of disturbance amplitudes, as well as validate qualitative features of the DSW trailing edge. This represents the first such systematic, experimental inquiry into validating DSW theory for the initial step problem.

6.2 Introduction

While dissipative shock waves are characterized by a smooth, rapid transition, the dispersive regularization of nonlinear steepening takes on a strikingly different structure. In dissipationless, superfluid-like systems, a universal mechanism of shock regularization manifests as wave breaking is resolved by the formation of a rapidly oscillating, slowly varying envelope of amplitude-ordered, nonlinear waves connecting two distinct states. This modulated wave train, known as a dispersive shock wave (DSW), is characterized by a large amplitude soliton at one edge and a small amplitude packet of nearly linear waves at the opposite edge and represents a universal structure for shock formation in approximately conservative, nonlinear media. Broad interest in DSWs has been stimulated in recent years by their observation across a range of

classical and quantum mechanical systems, with examples from ion-acoustic plasma (collisionless shocks) [115], superfluids (quantum shocks) [23, 46, 77, 52], nonlinear optics [93, 119, 20], and geophysical fluids (undular bores) [89, 100], but a comprehensive, quantitative comparison between the mathematical theory of DSWs and experimental measurements for the most basic shock problem, the evolution of an initial step in one spatial dimension (1D), has proved elusive. In many of these systems, qualitative agreements between numerical simulations of the governing equation and the experimental observations has been demonstrated, but the only quantitative comparisons exist for weakly nonlinear, small amplitude idealized models of wave propagation [116] that have limited ranges of physical applicability. The most notable reason for the lack of experimental validation is the absence of a dissipationless, effectively 1D physical system whose experimental study lends the fidelity needed to create a discontinuity of arbitrary amplitude and whose physical properties admit an analytically tractable approximate model valid for long times and large spatial extents. In this manuscript, we present a fundamental fluid system, the vertical evolution of a buoyant, viscous fluid within a medium of dense, much more viscous fluid, which has precisely these qualities. We use this system to perform the first careful comparisons between strongly nonlinear DSW theory and experimental measurement for well-developed shock waves across a range of amplitudes for the most fundamental shock problem, the initial step.

The fluid setting of interest is realized by injecting from below an intrusive viscous fluid into a quiescent basin of dense, highly viscous exterior fluid of similar composition. If the rate of injection is steady, a vertically uniform, fluid filled pipe, or conduit, of the intrusive fluid is formed [124]. When the rate of injection is slowly varied, however, characteristic dispersive hydrodynamic wave patterns, i.e. solitons and DSWs, are formed along the free interface between the two fluids. The approximate model governing the dynamics of the perturbed system can be written in terms of a single, scalar quantity, the cross-sectional area of the intrusive conduit, A , as a function of the vertical coordinate, z , and time, t , in the nondimensional form

$$\frac{\partial A}{\partial t} + \frac{\partial}{\partial z} \left\{ A^2 \left[1 - \frac{\partial}{\partial z} \left(\frac{1}{A} \frac{\partial A}{\partial t} \right) \right] \right\} = 0 . \quad (6.1)$$

Initially proposed as a simplified model for the vertical ascent of magma along narrow, viscously deformable dikes in the upper mantle [75, 97], the conduit equation was first derived by assuming small variation in the pipe area from the uniform background state and physically intuiting an interfacial force balance between the nonlinear advective effects of the buoyancy of the intrusive fluid and the, ironically, nonlinear dispersive effects of the viscous resistance to motion of the exterior fluid [99, 83]. More recently in an effort to characterize wave features of the fluid system, the model equation was rederived systematically from the full set of coupled fluid equations using a perturbative, multiple scales procedure with the intrusive to exterior fluid viscosity ratio as the asymptotically small parameter, ϵ , and shown to be valid for long times, $T = o(\epsilon^{-3/2})$, and large amplitudes, $a = o(1/8\epsilon)$, provided modest physical assumptions on the basin geometry, background velocities, fluid compositions, and characteristic aspect ratio hold [68].

The model equation has been verified in the case of solitons, a robust experimental feature of the system created by producing a localized pulse in the injection rate, with (nondimensional) amplitudes as large as ~ 14 , by showing favorable comparison between the theoretical amplitude-speed relation and that of experimental solitons [99, 83]. Follow-on experiments established agreement between experimental wave profiles and demonstrated that their interactions are approximately elastic with their profiles asymptotically restored following collision [43] and exhibited agreement with numerically predicted collision geometries [71]. Here, we extend the existing nonlinear conduit wave studies to conduct carefully controlled experiments on conduit shock waves, created by a sustained increase in the background rate of injection. Although previously interpreted as periodic wave trains (e.g. [99]), the increased injection rate results in a large trailing, vertically uniform conduit connected to a smaller, leading conduit by a dynamically expanding, *modulated* periodic wave train with a large amplitude leading edge and diminishing amplitude tail. Utilizing the theoretical and numerical results for conduit DSWs [69], we conduct the first systematic comparison of experimental measurement of the key DSW features (leading amplitude and speeds) with nonlinear wave modulation theory for DSWs emanating from step-like data [125, 40, 24].

6.3 Theoretical Background

Here we present a summary of the theoretical predictions for key, experimentally measurable properties of conduit DSWs, as derived in [69] for a generalized form of the conduit equation (6.1). The idealized shock problem under consideration here is eq. (6.1) with step-initial data of the form

$$A(z, 0) = \begin{cases} A_- , & z < 0 , \\ 1 , & z \geq 0 , \end{cases} \quad (6.2)$$

where $A_- > 1$ to ensure wave breaking. The downstream conduit area can be normalized to unity without loss of generality due to the existence of a scaling symmetry of the conduit equation [69]. Note that the initial value problem considered here is slightly different than the one in [69] in that we take the amplitude of the trailing conduit to be variable, rather than the leading. This is because in the experiments, we fix a background conduit area and then variably increase the injection rate to create a step.

Due to the lack of complete integrability of the conduit equation, the appropriate framework for deriving analytical information for the properties of DSWs for the step initial value problem is the Whitham-El DSW modulation theory, which results in closed-form analytical expressions for the speeds of the trailing and leading edges, s_{\pm} , of the wave envelope and its leading wave amplitude, a_+ [125, 40, 24]. The results of Whitham-El theory for the conduit equation were compared with numerically simulated DSWs and shown to be in good agreement up to a critical step-height, $A_c = 6.4$. The theoretical speeds are given explicitly from

$$s_- = 8 + 3A_- - 3\sqrt{A_- (A_- + 8)} , \quad (6.3)$$

$$s_+ = \sqrt{1 + 8A_-} - 1 . \quad (6.4)$$

The amplitude of the leading edge is obtained by assuming the first oscillation in the wave train is approximately a soliton propagating on a background of unity. Then using the predicted speed,

the amplitude can be solved from the implicit amplitude-speed relation for conduit solitary waves

$$s_+ = \frac{2a_s^2 \ln a_s - a_s^2 + 1}{a_s^2 - 2a_s + 1} , \quad a_s = a_+ + 1 . \quad (6.5)$$

A physically interesting regime appears when $A_- > A_b = 8/3$, because the analytical theory predicts the DSW will expand downward, despite this being a unidirectional model for upward wave propagation. This results from the property that the trailing edge is approximately a coherent packet of linear waves, and thus the DSW edge propagates according to the linear wave group velocity evaluated at an appropriate wavenumber. The importance for the present study is that it is difficult to measure a group velocity, but backflow gives us a qualitative feature with which we can validate the predictions in the trailing edge. Additionally, backward propagation of waves could induce undesired boundary effects near the point of injection, so these need to be accounted for properly by the experimental set-up. The details of converting the initial value problem into a boundary value problem to prevent corruption of our modeling assumptions will be discussed below.

6.4 Experimental Procedures

In this section, we cover the details of the experimental set-up and data processing involved in measuring DSW properties, as well as the physical and mathematical considerations required for validating key modeling assumptions and prescribing appropriate perturbations via injection.

6.4.1 Laboratory Set-Up and Fluid Properties

The experimental apparatus, set-up, and execution closely follows [71], but a larger, square cylinder apparatus, with dimensions $5.08 \text{ cm} \times 5.08 \text{ cm} \times 182.88 \text{ cm}$, has been used here to allow for longer propagation distances. The device is filled to a level of approximately 150 cm with generic brand light corn syrup. The intrusive fluid is a dyed, diluted mixture of corn syrup and water, with an approximate ratio of 70:30 corn syrup to water. Viscosities are measured

using a rotational viscometer with 2% accuracy and densities with a graduated cylinder and balance, yielding an uncertainty of 1%. The measured fluid properties are reported in Table 6.1.

The experiments are initiated by the formation of a straight background conduit of constant area using an automated syringe pump set to a constant injection rate and an initiation procedure similar to previous experiments. We note that this process in the larger apparatus can take several hours, as the system must equilibrate and transient dynamics must fully propagate out of the system. The background injection rates used in the experiments here varied between 0.1 and 0.3 mL/min. Conduit DSWs are created by programming boundary data into a second syringe pump, which results in the formation of a step-like state in the system's interior, far from the nozzle in order to minimize boundary effects. The theoretical basis for relating the syringe injection rate to the conduit area and deriving the appropriate DSW boundary condition is described below.

High resolution images using digital SLR cameras, with the aid of a macro lens, are used to collect data on the speed and amplitude of the leading edge of the DSW, as well as on the size of the step. We are able to capture approximately 10 centimeters of vertical propagation distance, while maintaining high resolution of the conduit. Measurements are achieved by placing one camera near the bottom of the apparatus to measure the initial conduit area and the area after the step is created, and another camera roughly 120 cm up the apparatus to take images of the leading wave as it passes the view of the camera. In general, we are able to take four images of the DSW front as it passes the top camera. Nondimensional camera distances are converted to physical units by use of a 1 mm square grid on the back of the tube. Errors due to the projection of the conduit onto the back wall are accounted for by comparing the known width of the nozzle with its measurement found using the grid. This gives us an effective refraction scaling of approximately 1.036. Distance measurement errors were previously estimated to be not more than 2% [71]. We also collect data on the qualitative structure of the DSW interior and its behavior near the trailing edge. To achieve this, we take still-frame images of the full device using a third digital SLR camera equipped with a standard lens during each experiment every

Table 6.1: Characteristic fluid properties of the experimental system.

$\rho^{(i)}$ (g/mL)	$\rho^{(e)}$ (g/mL)	$\mu^{(i)}$ (P)	$\mu^{(e)}$ (P)	ϵ
1.24	1.38	0.77	67.69	1.14×10^{-2}

5 seconds. Because we vary the area of the background conduit, we must verify the modeling assumptions in [68] for each experiment, as the characteristic lengths and velocity depend on the background. In the following section, we describe the procedure for processing the images and obtaining actual DSW properties.

6.4.2 Image Processing and Measurement Extraction

Data collected for each DSW experiment is in the form of raw RGB images, which we must then process and extract speed, amplitude, and other qualitative data. We first recall that the theoretical model is derived by assuming the physical vertical coordinate is stretched relative to the radial direction by a factor of approximately $\epsilon^{-1/2}$. In analyzing images, it is beneficial to impose this theoretical aspect ratio on the physical images by either upsampling the radial direction by a factor of $\epsilon^{-1/2}$, taken to be approximately 10 in practice, or downsampling the radial direction using standard interpolation algorithms. When measuring amplitudes or obtaining qualitative propagation information, it is best to downsample the vertical direction to leave the radial unchanged, while measuring vertical propagation speeds better lends itself to upsampling the radial direction. In all cases, the images are rotated so that the conduit is vertical. Here we briefly summarize our methods for image processing, starting with the macro lens images and then the lower resolution, full conduit images.

From the high resolution images, we wish to extract dimensional (in cm) conduit widths (and thus areas) and speeds (in cm/s). We systematically process each raw image using standard tools in Photoshop software in the following manner. In the raw images, the conduit background is typically an off-white color with the grid along the background, and the conduit fluid takes a green tint. Our goal in processing is, while preserving the physical boundary between the fluid

and the grid, to heighten the contrast between the two colors. We convert the image to the Lab color spectrum, in which the middle ‘a’ channel represents, roughly, reds and greens. We then use the curves tool in Photoshop in the ‘a’ channel to increase the contrast between the conduit fluid (i.e. increase the color tone of the green fluid, making it greener) and the background grid (by decreasing the color tone, or increasing its redness). This creates a sharper contrast between the two objects, making it easier to delineate the boundary. To measure wave amplitudes, we downsample the vertical direction by a factor of ten to ease the identification of the peak of the wave. To measure the speed of the first waves in the wave train, we use a sequence of images taken from the top camera, upsampled in the radial direction. In each image, we identify the vertical position of the wave peak and record the time the image was taken, which the camera reports to hundredths of seconds.

The lower resolution images of the full conduit are used to obtain qualitative information about the quality of the trial and structure of the shock, and could be used in the future to measure leading wave speeds over longer propagation distances. We process the collected images by cropping out the extraneous information, using the curves feature to darken the conduit fluid relative to the background, and downsampling the vertical dimension to keep the file sizes manageable. We do not find the conversion to Lab color to be helpful in this case, so we use the standard RGB color spectrum. With the time sequence of images for each trial spaced every 5 seconds, we assemble the still-frames into a movie, from which we can readily obtain qualitative information.

To compare physical speed and amplitude measurements with theory, we normalize the leading conduit area to one and divide all other measurements by this amplitude. For the speeds, we normalize by the characteristic velocity U , reported in, e.g., [68]. U depends on the background conduit area, here taken to be the leading conduit, so we compute its area using the images of the conduit just ahead of the leading wave in order to minimize the effects of any conduit size variability in the vertical direction. More is said about this variability below.

6.4.3 Comments on the Experimental Data

The results presented here come from 11 DSW experimental trials. As stated in the preface to this chapter, the experimental data here is preliminary and steps will be taken in subsequent investigations to remedy the issues and collect more data. From these data, we not only studied DSWs, but also examined several key physical properties about the system which we explain below. We found that only 7 out of the 11 trials resulted in a reasonable approximation to a DSW, so we report on only those trials below but use all 11 in consideration of other system properties. Here we want to briefly comment on the issues we encountered.

The most significant problem in these experimental trials was the issue of longer equilibration times due to the larger apparatus and more complicated nozzle device. This created issues with maintaining a straight, steady conduit, which were not previously encountered when using a smaller apparatus. Additionally, the time we allowed between experiments was likely too short. In studies of solitary waves, the disturbance to the medium is highly localized in time and space and thus its effects are minimal once it reaches the top of the apparatus. DSWs, on the other hand, are large scale, large amplitude features, and it takes tens of minutes for the system to equilibrate following a DSW trial run, which was an issue at the beginning of the data collection. Other issues arose due to lighting, the main one being glare from overhead lights appearing in the images. In future experiments, we will light the conduit from the back using low heat, LED lights. Lastly, due to many of the issues described here, there were not enough quality experimental trials conducted.

Despite these issues, we still find the results of these experiments to be meaningful, and observe good agreement between theory and experiment for DSWs, as well as for the issues discussed below.

6.4.4 Considerations for the Bottom Boundary

A major difference in the theoretical conduit model and the full physical system is the presence of a bottom boundary in the experimental system, whereas the idealized construction considers

the dynamics on an infinite vertical line. This introduces a number of challenges, but here we discuss two primary ones and their resolution. One is that the fluid system, near the bottom boundary undergoes a transient period of equilibration, during which the pipe size set by the nozzle radius and the injection rate relaxes to the size set by the fluid system. This initial transient state is neglected by the model, but it is important for experimental control to be able to predict the size of the conduit resulting from a particular injection rate. The second consideration is in translating the theoretical results, derived by considering an initial value problem for the conduit equation on an infinite line, to a physical system of finite spatial extent which allows a boundary condition and not an initial condition. There is also the issue that our modeling assumptions account for only long wavelength perturbations of the conduit area, and not the fast transitions which result from a rapid, sustained increase in the injection rate, which is perhaps the obvious method for creating a step in the conduit area. The goal is to prescribe slowly varying boundary data, via the syringe pump, which results in gradient catastrophe at a fixed distance from the boundary. These two boundary problems will be considered in this section, and their theoretical resolution will be considered in the context of the experimental data.

Relating the Injection Rate and the Conduit Diameter

First, we relate the injection rate from the syringe pump to the area of the resulting conduit above the equilibration region. Note that the quantities in this discussion are in dimensional form. The equilibrium conduit diameter is the directly measurable experimental quantity, so we seek a relation between the injection rate, q_0 , and the conduit diameter D_0 . Because we are dealing with viscous fluids of low Reynolds number, it is assumed that the area of the conduit, A , if the injection rate is held constant, is a function of only the vertical variable z within the adjustment region. Then assuming the region has a characteristic vertical length δ , conservation of conduit fluid implies

$$\rho^{(i)} \frac{d}{dt} \int_0^\delta \int_{A(z)} d\tilde{V} = q_0 - Q_0 , \quad (6.6)$$

where q_0 is the rate of injection set by the pump and Q_0 is the volumetric flow rate in the conduit above. Implicitly, we are assuming the nozzle flow rate is equal to the injection rate at the syringe pump, which is reasonable for incompressible fluids, though we consider this further below. Hence, the injection rate is related to the equilibrium conduit by the relation

$$q_0 = Q_0 . \quad (6.7)$$

The dependence of Q_0 on the conduit diameter is the basis of the theoretical model and is given by

$$Q_0 = \left[\frac{\pi g (\rho^{(e)} - \rho^{(i)})}{2^7 \mu^{(i)}} \right] D_0^4 . \quad (6.8)$$

Substituting eq. (6.7) into eq. (6.8) yields the desired power law relating the injection rate to the conduit diameter, complete with an explicit prediction for the leading coefficient

$$D_0 = \alpha q_0^{1/4} , \quad \alpha = \left[\frac{2^7 \mu^{(i)}}{\pi g (\rho^{(e)} - \rho^{(i)})} \right]^{1/4} . \quad (6.9)$$

It is important to note that the power law relationship is valid only when the injection rate is constant, and additional considerations need to be taken for a variable rate.

The relation (6.9) was compared with data taken from 22 different conduit measurements from DSW experiments. Using the experimental parameters reported in Table 6.1 and measurements of conduit diameter in cm and injection rate in mL/min, the theoretical value of the coefficient is $\alpha \approx 0.248 \text{ min}\cdot\text{cm}$ with lower and upper bounds of 0.237 and 0.263, respectively, when accounting for the maximum uncertainties associated with measuring the fluid densities and viscosities. A comparison between the results of the experimental trials and the theoretical result is given in Fig. 6.1.

It is apparent from the figure that eq. (6.9) is systematically underestimating the diameter of the conduit resulting from a given injection rate, which could be due to a number of reasons. One is the uncertainties involved in measuring the fluid properties, though we have attempted

to account for this by giving error bars. Another is that one of our modeling assumptions could be violated, most likely that the injection rate is not identical to the flow from the nozzle. This could be due to small amounts of air in the lines connecting the syringe to the nozzle, friction in the line and/or nozzle apparatus due to the walls or possibly viscous residue left behind by the fluid. Lastly, there could be some uncertainty in the programmed injection rate and the actual rate of injection carried out by the pump. As a result, we also report the results of fitting the data to a power law of the general form $D_0 = Cq_0^{0.25}$ using nonlinear least squares, also plotted on Fig. 6.1. The resulting coefficient is $C \approx 0.27$, just higher than the upper bound of our theoretical prediction. The data was also fit to a general power law with undetermined coefficient and nonlinear power, but the power determined by the fitting was 0.24, so we took this to imply that the $1/4$ power predicted from theory is the correct relationship.

Boundary Data

The other particularly important boundary issue with which to contend in studying DSWs in the experimental conduit system is in properly prescribing slowly varying boundary data in order to study the step problem. Because our model neglects boundary effects and is valid only for slow vertical variations, we need to find boundary data which results in wave breaking far above the nozzle. Note that in this discussion we revert to dimensionless variables for ease of presentation. We also assume that the above, theoretically-derived power law gives a reasonable approximation for translating syringe pump data, even data which varies slowly in time, into conduit area data, though this could be a source of improvement in future experiments. In referring to boundary data, we mean the boundary above the adjustment region where the conduit equation applies, and assume that we produce the desired boundary by programming the injection rate according to eq. (6.9).

Since wave propagation along the conduit is unidirectional (though we identified above the possibility of backflow for sufficiently short waves), the theoretical initial value problem with localized variation posed on the whole real line and the experimentally relevant initial/boundary

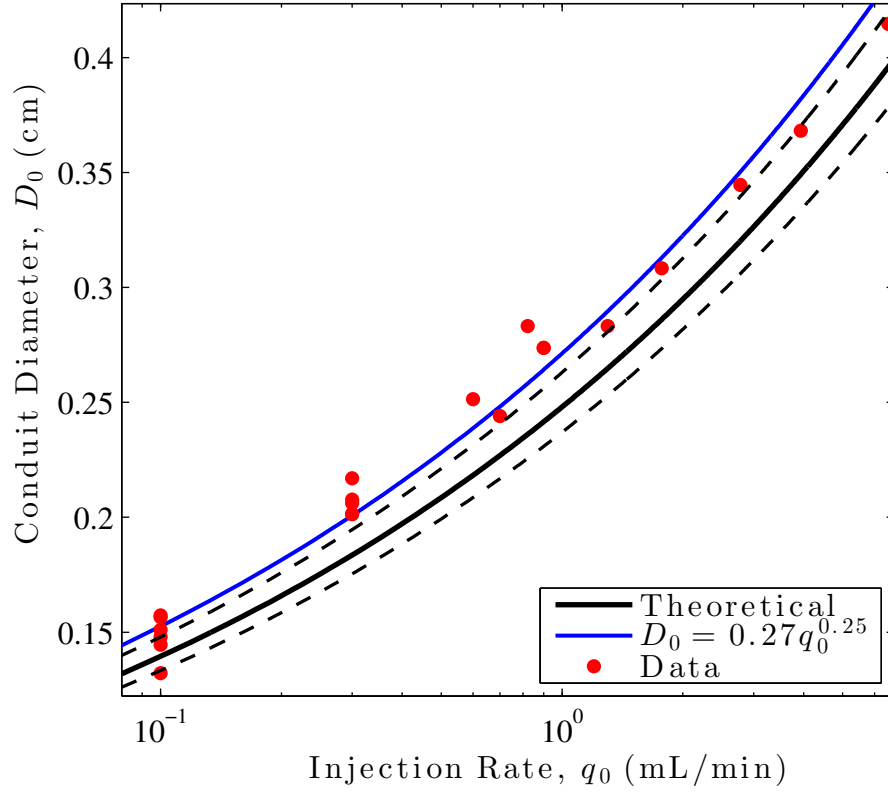


Figure 6.1: Comparison of observed conduit diameter plotted against the log of the injection rate. The blue line is the result of a nonlinear least squares fit to the experimental data, assuming a nonlinear power law with exponent 1/4. The lighter dashed lines above and below the solid black prediction curve from theory represent error bars due to the uncertainty in measuring the fluid properties.

value problem posed on the half-line can be related. We wish to study the results of boundary data which produces a large, trailing conduit of uniform area connected to a leading, smaller conduit of uniform area. However, the conduit equation is valid only for slowly varying conduits, so the immediate choice of simply increasing the pumping rate via a step violates the model. Moreover, we have observed in experimental trials that this rapid transition results in a leading wave which does not appear to be connected to the DSW. To resolve this issue, we have devised two approaches, one which we implemented in our DSW experiments and the other which could be implemented in the future.

The idea behind both methods is to use the conservative nature of the conduit equation (or more generally of dispersive hydrodynamic systems) to consider the step problem in negative time. Our goal is to have a profile which is approximately a step, centered at $z = z_0$, with z_0 well above the nozzle, which breaks at $t = t_b > 0$, i.e.

$$A(z, t_b) = \begin{cases} A_- , & z < z_0 , \\ 1 , & z \geq z_0 . \end{cases} \quad (6.10)$$

Recalling the general modulation theory approach for dispersive shocks [24, 69], outside of the DSW interior, the dynamics are well described by the zero dispersion limit of the conduit equation. Note that the hyperbolic dispersionless limit of the conduit equation has finite propagation speed. This is not, in general, true of the full equation, which is nonlocal and thus has “infinite” propagation speed, but here we leverage the finite propagation speed in the dispersionless limit as a long wavelength proxy for the full equation. By examining the characteristic (z, t) -plane, one observes that in reversed time, $\tau = t_b - t$, step-initial data of the form (6.10) leads to a rarefaction wave. Thus the idea is, given a desired point of breaking in the interior of the experimental apparatus z_0 , use eq. (6.10) as an initial condition and propagate backwards in time until $\tilde{A}(0, t_b(z_0)) = 1$. This gives a solution $A(z, t) = \tilde{A}(z, \tau)$. Then the evaluation of that

solution at $z = 0$ yields the appropriate boundary condition, namely

$$A(0, t) = \tilde{A}(0, \tau) , \quad \tau \in [0, t_b(z_0)] . \quad (6.11)$$

One can derive an analytical boundary condition by considering only the zero dispersion limit of the conduit equation, recalling that a rarefaction solution to a dispersive hydrodynamic equation is well-described by the long wavelength reduction. After the change of variables $\tau = t_b - t$, $\tilde{A}(z, \tau) = A(z, t_b - \tau)$, the dispersionless conduit equation becomes

$$\tilde{A}_\tau - 2\tilde{A}\tilde{A}_z = 0 . \quad (6.12)$$

Seeking a self-similar rarefaction solution of the form $\tilde{A}(z, \tau) = f(\xi)$, $\xi = (z - z_0)/\tau$, leads to the following solution

$$\tilde{A}(z, \tau) = \begin{cases} A_- , & \frac{z - z_0}{\tau} < -2A_- , \\ \frac{z_0 - z}{2\tau} , & -2A_- \leq \frac{z - z_0}{\tau} \leq -2 , \\ 1 , & \frac{z - z_0}{\tau} > -2 . \end{cases} \quad (6.13)$$

It still remains to choose, given a desired z_0 , the value of t_b so that $\tilde{A}(0, t_b(z_0)) = 1$ and $\tilde{A}(z, t_b(z_0)) > 1$ for all $z < 0$. This is achieved by determining the amount of time required for the trailing edge (in negative time) of the rarefaction wave to reach the origin, which yields a breaking time

$$t_b(z_0) = \frac{z_0}{2} . \quad (6.14)$$

Using this value for the breaking time and evaluating the rarefaction solution at $z = 0$ for $t \in [0, t_b(z_0)]$, we have the approximate boundary condition, as predicted by using only the dispersionless limit,

$$A(0, t) = \begin{cases} \frac{z_0}{z_0 - 2t} , & 0 < t < \frac{z_0(A_- - 1)}{2A_-} , \\ A_- , & t > \frac{z_0(A_- - 1)}{2A_-} . \end{cases} \quad (6.15)$$

The appeal of using only the dispersionless limit is that one arrives at an analytical, explicit representation for the boundary condition (6.15) and breaking time (6.14) as a function of only the breaking point z_0 . The issue is that, while the zero dispersion conduit equation well describes a rarefaction solution for the full conduit equation, there are known differences, such as the formation of small amplitude dispersive waves near the edges of the rarefaction. An alternative, and more precise, method for deriving the desired boundary condition is to use the full conduit PDE and run numerical simulations in negative time (simply change variables from $t \rightarrow -t$) starting from a smoothed initial step of the form (6.10). The boundary condition and breaking time are then derived numerically, following an identical procedure to the one above for the zero dispersion equation, but it results in a numerically defined solution, rather than an explicit one. There are, however, several considerations to take into account when implementing this procedure. One is that a sharp step cannot be simulated numerically, so some smoothing must be implemented. This leads to longer breaking times but smoother boundary data. The second is the issue of the formation of small amplitude oscillations due to the inclusion of the nonlinear dispersion term. We have observed that these waves tend to develop at the trailing edge of the rarefaction wave, so it is difficult to define when the trailing edge reaches the origin to define the breaking time. As an approximation, we take t_b to be the first time at which the solution $A(0, t) = 1$, thus we still neglect some effects of the dispersive oscillations. The most important issue with this method, however, is that it is more costly, in that a full, high resolution, numerical simulation of the conduit equation must be run for every choice of A_- and z_0 in order to derive a boundary condition to program into the syringe pump.

A comparison of the boundary conditions derived by the two methods for a particular choice of A_-, z_0 is given in Fig. 6.2. While the results of the zero dispersion method yield a good approximation to the full numerical method, the time to breaking tends to be underestimated and the ramp to A_- is steeper. However, we have found in practice that a “pure” DSW, i.e. a well-ordered, slowly modulated nonlinear wave train, can be produced by the zero dispersion boundary condition, so it has been used exclusively in the DSW trials reported here. After all,

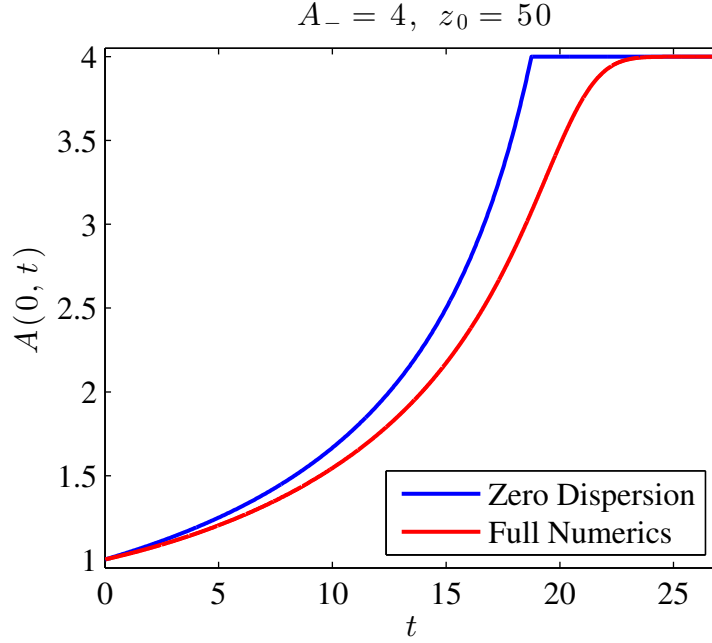


Figure 6.2: Comparison of the two methods (numerical simulations of the full equation and the zero dispersion limit) for deriving the boundary condition for a step size $A_- = 4$, with breaking occurring at $z_0 = 50$.

the DSW is the long time asymptotic resolution of data that asymptotes to $A(z, t) \rightarrow A_{\pm}$, $z \rightarrow \pm\infty$, $A_- > A_+$ (see, e.g., KdV [1]) so any variations from a pure step at breaking time will lead to effectively transient behavior.

6.4.5 Validation of Area Conservation

The most fundamental assumption made in deriving the conduit equation is that mass is not exchanged between the intrusive and the exterior fluid. Otherwise, the conduit area would not be conserved, and we would expect a physical diffusion to be present in the leading order model. One way to test this assumption experimentally is to measure the conduit area using the high resolution, macro lens images taken at the bottom of the conduit and compare with areas measured of the same conduit using images from the top of the apparatus.

This study was conducted using the DSW experimental data. The measurements of the

Table 6.2: Comparison of the relative difference in area of the conduit area, as measured by two high-resolution cameras separated by approximately one vertical meter.

Trial	Area Bottom (cm ²)	Area Top (cm ²)	Relative Difference
1	0.0192	0.0216	0.121
2	0.0194	0.0197	0.013
3	0.0172	0.0209	0.214
4	0.0370	0.0362	0.022
5	0.0339	0.0387	0.141
6	0.0334	0.0387	0.159
7	0.0319	0.0366	0.150
8	0.0319	0.0293	0.080
9	0.0179	0.0208	0.162
10	0.0137	0.0162	0.180
11	0.0164	0.0193	0.177

bottom of the conduit were taken using the images from the lower camera preceding the increase in injection rate. For the corresponding image from the top of the apparatus, the conduit area was measured just ahead of the leading edge of the DSW. The results are presented in Tab. 6.2. Although the technique was crude and required the assumption that the area of the leading conduit was unperturbed by the creation of a DSW behind it and despite the experimental difficulties identified above, perhaps the most important being the lack of sufficient equilibration time between trials, we found the average relative difference to be only 12.9%, with standard deviation 6.5%. We believe this offers some validation of the physical assumption of area conservation, though we will consider this more carefully in future experiments.

6.5 Results of DSW Experiments

The speed and amplitude results of the 7 quality DSW experimental trials on varying step heights are reported in Tab. 6.3, and the evolution of a typical DSW, as captured by the full conduit images, is presented in Fig. 6.4. The combination of the boundary condition (6.15) and conversion from pumping rate to conduit area was found to produce reliably a conduit profile which broke well into the interior of the apparatus. The presence of such a large number of

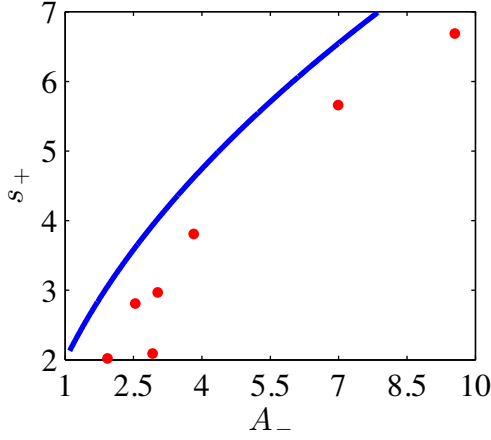
well-ordered dispersive oscillations (up to 50 in some experimental trials and approximately 20 in the bottom image of Fig. 6.4) represents a DSW that is asymptotically resolved and the best experimentally realized, physical manifestation of the idealized long-time, asymptotic state assumed by DSW theory to date.

The experimental data is compared with analytical predictions of Whitham-El modulation theory in Fig. 6.3. The DSW leading edge amplitude is well-predicted by the theory, particularly for smaller step sizes. At larger amplitudes, the theory over-predicts the solitary wave amplitude, a feature which was previously observed numerically in studies of the conduit equation [69]. The speeds s_+ are systematically overestimated by modulation theory. This was also observed in the previous numerical study, though to a lesser degree. The discrepancies in the speeds could be due to the measurement technique, which allowed a limited number of position measurements over a limited vertical extent. Capturing the propagation over a greater distance, even with slightly lower resolution, will likely improve these results. This is further supported by the higher accuracy results of the amplitudes a_+ , which were measured far more precisely but is found using only nondimensional amplitude ratios. The speed measurements, on the other hand, require nondimensionalization by the characteristic velocity U , which involves the fluid density difference and the interior fluid viscosity. We note further that despite the breakdown of the theoretical method for $A_- > A_c = 6.4$, it was still found to give reasonable approximation for the DSW properties in previous numerical studies, and appears to give favorable comparison with experimental data, though only two of our trials lie beyond this point. The validity of the model equation has also not been shown in the asymptotically large, i.e. $A \gtrsim \mathcal{O}(\epsilon^{-1})$ amplitude regime, which is certainly achieved in these experiments. More experiments need to be conducted to study the possible implications this could have in interpreting the results in the context of modulation theory.

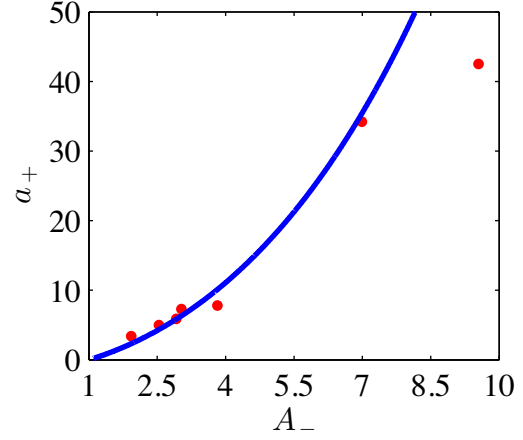
In addition to the speed and amplitude measurements, we also sought to identify the backflow regime. In general, small amplitude, short wavelength dispersive oscillations are beyond the sensitivity of these experiments, making the theoretical trailing edge of the DSW difficult to

Table 6.3: Nondimensional DSW speed and amplitude data for seven experimental trials.

Trial	A_-	s_+	a_+
1	2.92	2.09	4.9
6	1.93	2.02	2.4
7	2.54	2.81	4.0
8	3.82	3.81	6.8
9	3.03	2.97	6.3
10	9.55	6.69	41.5
11	6.99	5.66	33.2



(a) DSW Speeds



(b) DSW Amplitude

Figure 6.3: Comparison of DSW data collected on leading edge speed and amplitude versus theoretical predictions.

identify. Therefore, to identify backflow in experiment, we need to be well beyond the predicted threshold $A_b = 8/3$ so that the point of creation of small amplitude waves from the DSW interior can be seen to expand downward. A clear example of backflow from a qualitative experimental trial is presented in Fig. 6.5, in which small amplitude oscillations can be seen to propagate further down the conduit than initially. This encourages future qualitative studies on DSW properties, such as interactions with solitary waves, rarefaction waves, and other DSWs.

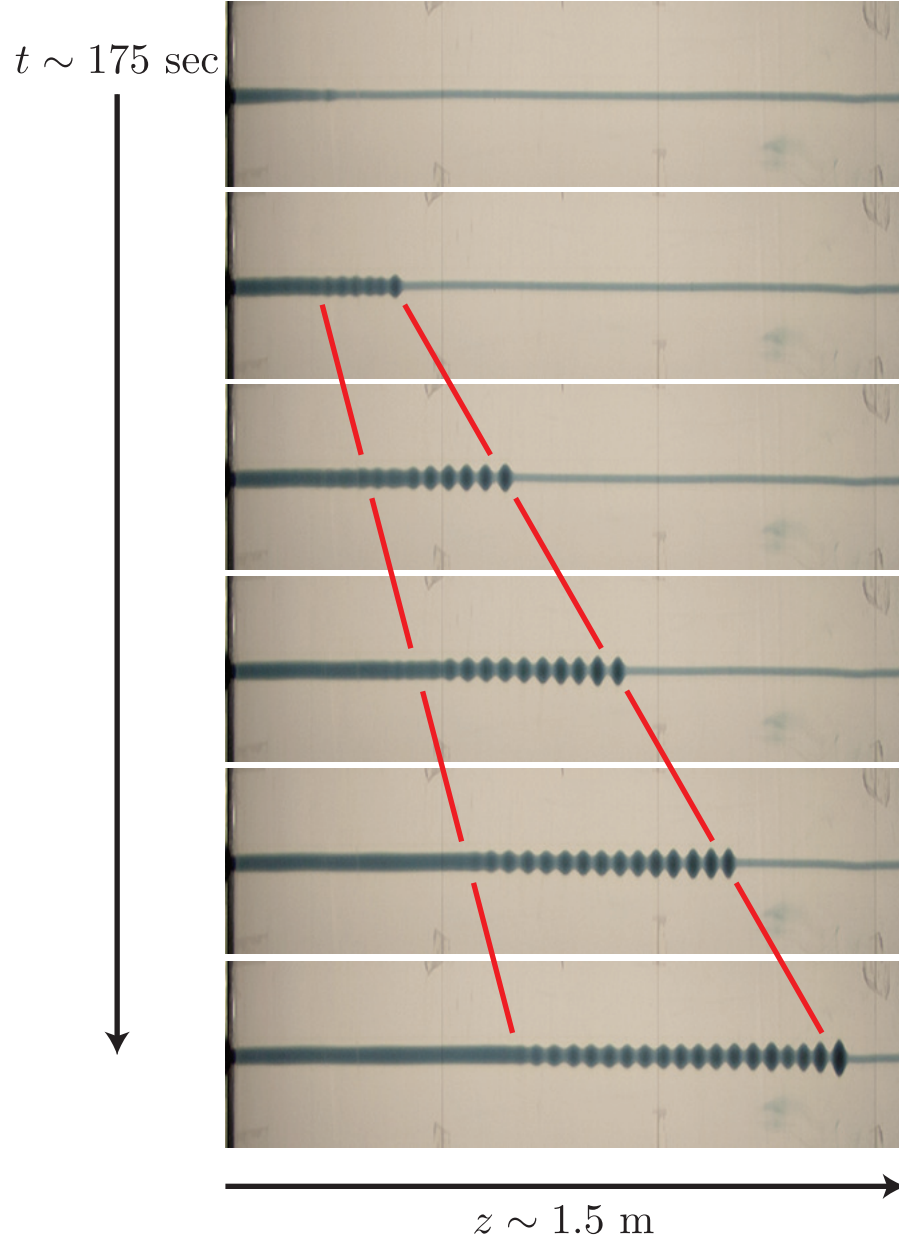


Figure 6.4: Example of the typical evolution of a conduit DSW with $A_- \approx 4.3$ and leading edge amplitude $a_+ \approx 18$. Note that the individual images were downsampled in the vertical direction by a factor of 10 as described. This experiment was qualitative, so the front propagation speed was not measured.

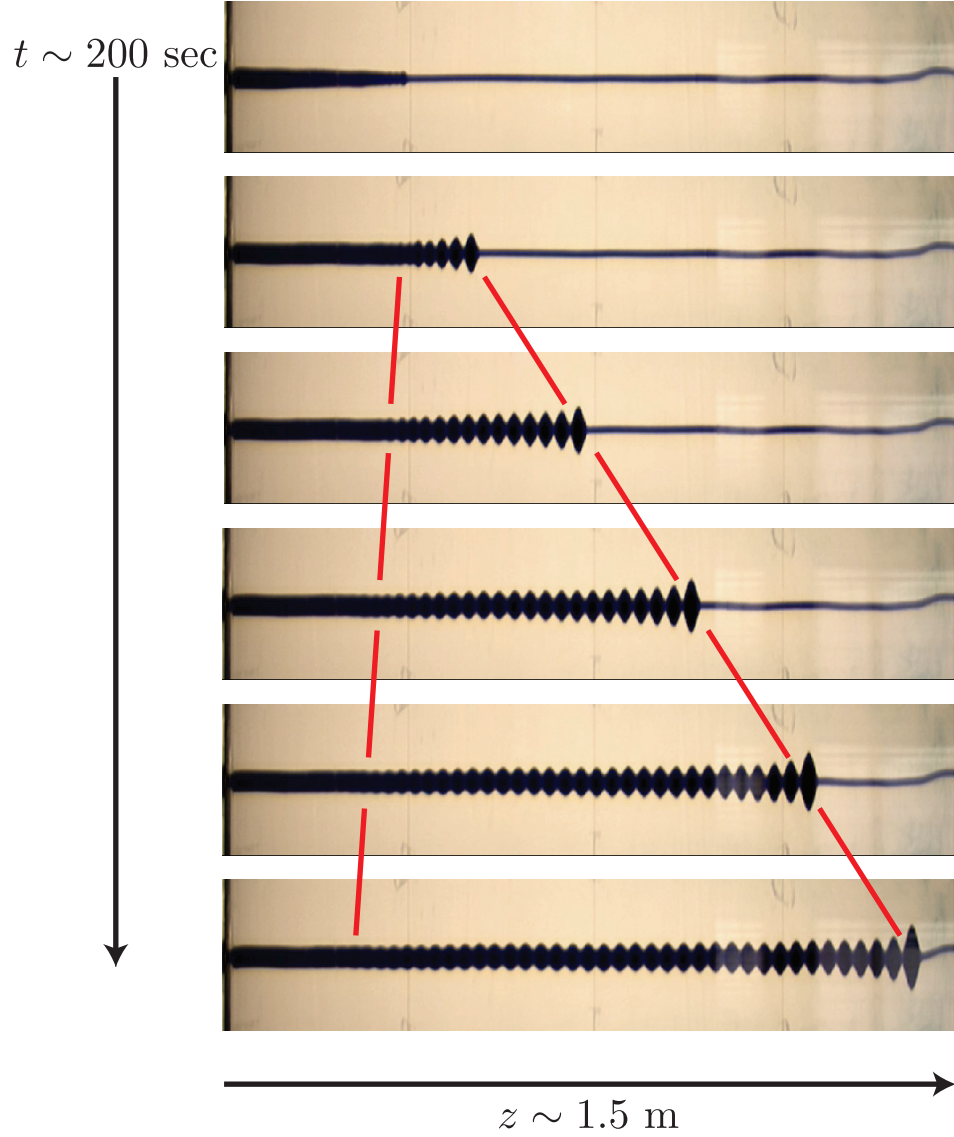


Figure 6.5: Example of backflow in a DSW with $A_- \approx 7.4$ and leading edge amplitude $a_+ \approx 37$. Note that the individual images were downsampled in the vertical direction by a factor of 10 as described. This experiment was qualitative, so the front propagation speed was not measured.

6.6 Discussion and Conclusions

The preliminary experimental data presented in this study will be expanded upon in future investigations. Several points of improvement have been identified here, which we now summarize. The most important improvement for future work is to provide more experimental DSW trials which well sample the step height parameter space, particularly the region $A_- \in [2.5, A_c]$. The lower bound 2.5 is chosen because measuring small amplitude conduit features magnifies measurement uncertainties.

Several significant, easily addressed, procedural improvements have also been identified. One is allowing longer equilibration times both before initiating experiments and following DSW trials. This will result in DSW propagation along a more uniform background. Another correction is the method of measuring propagation speeds for the leading edge wave. The limited propagation distances and short time window afforded by high resolution imaging via macro lens introduced unnecessary uncertainty into the experimental data. Capturing the leading edge wave over longer propagation distances and a greater number of images will lead to better results. The issue of lighting was also addressed. In the trials reported here, we used overhead lights, which created significant glare in the images. A better solution is to light the experimental apparatus from behind with LED lights which emit negligible amounts of heat and thus do not introduce new physical considerations. A last improvement which could reduce human error in measurements is to use an alternative method to the grid used here for converting camera distances to physical distances, say by submerging an object of known size in the exterior fluid long before experiments commence but then never changing the camera positions. Alternatively, the width of the apparatus could be used, provided corrections due to it not being submerged in the fluid could be properly taken into account. This has the distinct advantage that one could create a uniform background for the images and utilize algorithmic edge detection techniques to systematically extract the interface and its properties.

Although the experiments can be improved and expanded, the results of this study show that dispersive shock waves in viscous fluid conduits exhibit quantitative and qualitative agreement

with analytical predictions based on Whitham-El modulation theory. This is the first such system to be compared with the properties of a strongly nonlinear dispersive hydrodynamic model, and the most extensive comparison with DSW theory in any physical system to date. This agreement between theory and experiment, as well as the study on the spatial conservation of conduit area, further validates the conduit equation as the leading order description of the full system dynamics, lending support to the superfluid interpretation of wave propagation in viscous fluid conduits. Moreover, we have offered an extensive blueprint for conducting future investigations, most notably by demonstrating precisely how to create a carefully controlled step in the conduit area by programming boundary data into a syringe pump. This work is evidence that viscous fluid conduits provide an ideal platform for the study of one dimensional, nonlinear dispersive waves.

Chapter 7

Dispersive Shock Waves in a Bidirectional System

As discussed extensively, DSWs represent universal nonlinear structures which occur in any nonlinear, approximately conservative, superfluid-like system. While we have primarily been concerned with unidirectional conduit DSWs, the Whitham-El modulation theory also applies to bidirectional systems [24, 47]. In this chapter, we demonstrate the application of the nonintegrable DSW construction to a quantum mechanical setting known as unitary Fermi gas, a system for which it unclear what is the appropriate physical regularization mechanism for nonlinear wave breaking. We demonstrate how the differences in viscous and dispersive shock waves, in particular their speeds of propagation, can be used to identify the appropriate type of physical regularization, even when the theoretical oscillation wavelength for DSWs is too small to be imaged. We shed light on the limitations of quantitative DSW experiments in this setting by identifying the strict assumptions which must be satisfied to interpret the results with a 1D model. It is also identified that violating this assumption could lead to a transverse instability which bears strong resemblance with the dynamics predicted by a viscous regularization. The contents of this chapter are based on the following publication [70]:

Lowman, N. K. and Hoefer, M. A. 2013 “Fermionic shock waves: Distinguishing dissipative

versus dispersive regularizations,” *Physical Review A* **88** 013605.

7.1 Abstract

The collision of two clouds of Fermi gas at unitarity (UFG) has been recently observed to lead to shock waves whose regularization mechanism, dissipative or dispersive, is being debated. While classical, dissipative shocks, as in gas dynamics, develop a steep, localized shock front that translates at a well-defined speed, dispersively regularized shocks are distinguished by an expanding region of short wavelength oscillations with two speeds, those of the leading and trailing edges. For typical UFG experimental conditions, the theoretical oscillation length scale is smaller than the resolution of present imaging systems so it is unclear how to determine the shock type from its structure alone. Two experimental methods to determine the appropriate regularization mechanism are proposed: measurement of the shock speed and observation of a one-dimensional collision experiment with sufficiently tight radial confinement.

7.2 Introduction

Ultracold, dilute gases provide a universal medium for the study of nonlinear hydrodynamic flows in the presence of dissipation and dispersion [58]. Experimental attainment of the superfluid regime in a Bose-Einstein condensate (BEC) and a unitary Fermi gas (UFG) has led to the observation of nonlinear coherent structures of fundamental interest, including quantized vortices [74, 72, 129], solitons [15, 111, 127], and shock waves [23, 46, 52]. In the absence of regularization, the effects of nonlinearity can lead to self-steepening and gradient catastrophe. In many physical systems, this steepening is mediated by weak dissipation, often due to the effects of viscosity, which transfers kinetic energy to heat across a narrow transition region, a viscous shock wave (VSW). An alternative regularization mechanism occurs in dissipationless (conservative) media where self-steepening is balanced by dispersion, in which case gradient catastrophe is resolved into the formation of an expanding oscillatory region called a dispersive shock wave (DSW).

For BEC, a mean field description is well-established in which the hydrodynamic equations are regularized by dispersion (c.f. [55]). Generation of shock waves in recent UFG collision experiments has fueled interest in the formulation of an analogous theory for fermionic systems. While a direct, computational approach using density functional theory is available [14], two simplified models have been proposed and successfully fitted to the experimental data, one in which the hydrodynamic equations are regularized by dissipation [52] and the other by dispersion [5, 94]. Although effort has been made to develop theory incorporating dispersion in the weakly interacting regime [11, 90] and both dispersion and dissipation in the weakly nonlinear regime [58], large amplitude effects and the relative magnitude of dissipation and dispersion in the strongly interacting regime are still unknown. This raises a fundamental question – how does one determine the appropriate regularization for a UFG from experiment? An obvious distinction is the structure of the shock. A VSW takes the form of a traveling wave, while a DSW is characterized by an expanding collection of large amplitude oscillations. However, in the case of a UFG, the oscillation scale may be too fine to be imaged [52, 5]. In this article, we show that the type of regularization may alternatively be distinguished by measuring the shock speed; VSW and DSW speeds differ. We also highlight the parameter regime in which a three-dimensional (3D) experiment is amenable to one-dimensional (1D) simplification and argue that the collision experiments in [52] were fully 3D, like those observed in BEC [18]. We conclude with another regularization distinguishing experiment, the 1D collision problem where a prominent density bulge is predicted for the dissipative case alone.

7.3 Governing Equations

At zero temperature, the macroscopic, low energy dynamics of a Fermi superfluid can be described by the, as yet unregularized, equations of irrotational hydrodynamics [36]

$$\frac{\partial n}{\partial t} + \nabla \cdot (n\mathbf{v}) = 0 , \tag{7.1}$$

$$m \frac{\partial(n\mathbf{v})}{\partial t} + m \nabla \cdot (n\mathbf{v} \otimes \mathbf{v}) + \nabla P(n) = -n \nabla U(\mathbf{r}), \quad (7.2)$$

where $\mathbf{r} = (x, y, z)$, $U(\mathbf{r})$ is the trap potential, $\mathbf{v}(\mathbf{r}, t)$ is the velocity field, m is the particle mass, $n(\mathbf{r}, t)$ is the density, and the pressure law $P(n) = \xi \frac{\hbar^2}{5m} (3\pi^2 n^{5/2})^{2/3}$ is a scaled version of $\mu(n) = 5P(n)/(2n)$, the bulk chemical potential. The total number of particles $N = \int n d\mathbf{r}$ is conserved. The irrotational velocity field is proportional to the gradient of a velocity potential ϕ , $\mathbf{v} = \frac{\hbar}{2m} \nabla \phi$. The Bertsch parameter, ξ , is a dimensionless, universal constant for which we use $\xi \simeq 0.40$ [36], though more recent studies have suggested a slightly smaller value (e.g. [17, 31]). The particular value will not affect the results of our analysis, only the scalings. In what follows, we consider the case of a harmonic trap potential $U(\mathbf{r}) = \frac{1}{2} (\omega_\perp^2 r_\perp^2 + \omega_z^2 z^2)$, where $r_\perp^2 = x^2 + y^2$ and ω_\perp, ω_z are the transverse and longitudinal trap frequencies, respectively. It is convenient to introduce the harmonic oscillator lengths $a_{\perp,z} = (\hbar/m\omega_{\perp,z})^{1/2}$.

Conservation laws of the form (7.1), (7.2) are known to admit discontinuous shock solutions which, when interpreted in the vanishing viscosity limit, correspond to a generic dissipative regularization of gradient catastrophe [60]. The shock speed is determined by integrating (7.1), (7.2) across a sharp transition resulting in jump conditions. While the bulk viscosity of a UFG is negligible, its shear viscosity is not [16] suggesting that dissipation could be a viable regularization mechanism for the singular hydrodynamics.

In contrast, a dispersive regularization of the hydrodynamic equations, proposed in [95], uses an extended Thomas-Fermi functional approach. The first order correction to the hydrodynamic system is the addition of a von Weizsacker-type [118], dispersive correction term to the righthand side of (7.2) of the form $\lambda \frac{\hbar^2}{4m} \nabla \cdot (\rho \nabla \otimes \nabla \log \rho)$, where λ is a dimensionless parameter with accepted value $\lambda \simeq 0.25$ [5]. Note that studies in the weakly interacting regime have led to alternative dispersive models [11, 90]. While the particular form of the dispersion at the microscopic, oscillatory level is still unknown, the qualitative behaviors due to dispersion which distinguish such systems from their dissipative analogs hold for a broad class of forms (see e.g. [47]).

By introducing the complex wavefunction $\psi = \sqrt{n} \exp \left[i\phi/(2\sqrt{\lambda}) \right]$, the system (7.1), (7.2) with the gradient correction term can equivalently be written in the form of a generalized nonlinear Schrödinger (gNLS) equation, similar to the Gross-Pitaevskii equation from BEC mean field theory but with a different nonlinear exponent

$$i\hbar\lambda^{1/2}\frac{\partial\psi}{\partial t} = U(\mathbf{r})\psi - \lambda\frac{\hbar^2}{2m}\nabla^2\psi + \xi\mu_0|\psi|^{4/3}\psi, \quad (7.3)$$

where $\mu_0 = \frac{\hbar^2}{2m}(3\pi^2)^{2/3}$.

To formulate the 1D shock problem for a UFG, we consider the case of a cigar-shaped trap $\omega_\perp \gg \omega_z$ and derive an effective 1D equation from (7.3). We assume sufficiently tight radial confinement so that radial dynamics are negligible and integrate over the transverse coordinates following a standard procedure [76] (see Appendix for details). The anisotropy requirement for dimensionality reduction is $\frac{\omega_z}{\omega_\perp} \ll \frac{1}{N}$ [36]. This regime is realizable, for example by means of a 2D optical lattice [81, 12]. The 1D wavefunction $\Phi(z, t)$ then satisfies

$$i\hbar\lambda^{1/2}\frac{\partial\Phi}{\partial t} = \frac{1}{2}m\omega_z^2 z^2\Phi - \lambda\frac{\hbar^2}{2m}\frac{\partial^2\Phi}{\partial z^2} + \left[\frac{5m\omega_\perp^2(\xi\mu_0)^{3/2}}{4\pi} \right]^{2/5} |\Phi|^{4/5}\Phi, \quad (7.4)$$

where $\int |\Phi|^2 dz = N$. Note that tight transverse confinement leads to a nonlinear coefficient and power that differ from their 3D analog in (7.3). It is important to distinguish the various length and time scales in the problem so we nondimensionalize (see Appendix for details) by introducing $\Phi = \Phi_0 \tilde{\Phi}$, $z = L\tilde{z}$, and $t = T\tilde{t}$ with $L = L_0$, $\Phi_0 = \sqrt{N/L_0}$, $T \approx 1.56[L_0^6/(N\omega_\perp^5 a_\perp^6)]^{1/5}$. All stated approximate numerical values are given in full in the Appendix. L_0 is a characteristic length to be chosen. To obtain the hydrodynamic equations, the longitudinal wavefunction takes the form $\tilde{\Phi} = \sqrt{\rho} \exp \left(\frac{i}{\epsilon} \int \tilde{u} d\tilde{z} \right)$, and after dropping \sim , the system of 1D conservation equations for UFG is

$$\frac{\partial\rho}{\partial t} + \frac{\partial(\rho u)}{\partial z} = 0, \quad (7.5)$$

$$\frac{\partial(\rho u)}{\partial t} + \frac{\partial}{\partial z} \left(\frac{5}{7}\rho^{7/5} + \rho u^2 \right) = \frac{\epsilon^2}{4} \frac{\partial}{\partial z} \left[\rho \frac{\partial^2(\log \rho)}{\partial z^2} \right] - \kappa\rho z, \quad (7.6)$$

with

$$\epsilon \approx 0.78 \left(\frac{a_{\perp}^4}{N L_0^4} \right)^{1/5}, \quad \kappa \approx 2.45 \left(\frac{a_{\perp}^2 L_0^3}{N^{1/2} a_z^5} \right)^{4/5}, \quad (7.7)$$

and ρ, u are the dimensionless density and longitudinal velocity, respectively. These hydrodynamic equations admit the long wave speed of sound $c(\rho) = \rho^{1/5}$. Note that the transformation from (7.4) to (7.5), (7.6) is exact with no approximation. This form reveals the dispersive regularization of the hydrodynamic equations when $0 < \epsilon \ll 1$.

It is beneficial to briefly describe the relations between inherent length scales associated with different choices for L_0 . The longitudinal oscillation length, L_{osc} , associated with DSWs, is obtained by choosing L_0 in (7.7) so that $\epsilon = 1$. The longitudinal extent of the trapped UFG, L_{trap} , is determined by fixing L_0 in (7.7) so that $\kappa = 1$. Another important length scale is associated with the inter-particle spacing L_{int} that is estimated by standard arguments (see Appendix for details). The 1D anisotropy requirement leads to the following relations

$$L_{\text{int}} \sim \frac{a_{\perp}^{2/3} a_z^{1/3}}{N^{1/6}} \ll L_{\text{osc}} \sim \frac{a_{\perp}}{N^{1/4}} \ll L_{\text{trap}} \sim N^{1/6} \frac{a_z^{5/3}}{a_{\perp}^{2/3}}. \quad (7.8)$$

That DSW dynamics occur at length scales much larger than L_{int} is a requirement for the validity of the hydrodynamic model [36]. DSWs exhibit rapid oscillations with wavelength L_{osc} and a larger, envelope modulation length we denote L_{mod} . When $L_0 = L_{\text{mod}}$ such that $L_{\text{osc}} \ll L_{\text{mod}} \ll L_{\text{trap}}$, then $0 < \epsilon \ll 1$ and $0 < \kappa \ll \epsilon^2$ so that a dispersive regularization is appropriate and inhomogeneities due to the trap can be neglected. In what follows, we use parameters from experiment and set $L_0 = L_{\text{mod}} = 3\mu\text{m}$ corresponding to the experimental imaging resolution [52]. Then, $\epsilon \approx 0.05$ and $\kappa \approx 0.0003$, thus satisfying our smallness conditions. For the rest of this work we neglect the trap, setting $\kappa = 0$ in (7.6).

7.4 Effects of Regularization

We now discuss the dynamics of shock solutions for eqs. (7.5), (7.6) with $\epsilon = 0$ (dissipative regularization) and $0 < \epsilon \ll 1$ (dispersive regularization). We consider the conservation laws with general step initial data

$$\rho(z, 0) = \begin{cases} \rho_0, & z \leq 0 \\ 1, & z > 0 \end{cases}, \quad u(z, 0) = \begin{cases} u_0, & z \leq 0 \\ 0, & z > 0 \end{cases}. \quad (7.9)$$

For general ρ_0 and u_0 , single step initial data results in the generation of two waves. We focus on the case $\rho_0 > 1$ and u_0 specifically chosen from a locus of velocities corresponding to a single, right propagating shock wave.

7.4.1 Dissipation

In dissipatively regularized systems, shock waves are nonlinear traveling wave solutions which can be viewed as a balance between nonlinearity and dissipation. Deriving the shock profile for the hydrodynamic equations of UFG with a vanishing effective Newtonian viscosity is mathematically equivalent to constructing a weak solution for the system (7.5), (7.6) with $\epsilon = 0$. The magnitude of the dissipative correction sets the width of the localized transition region but does not affect the shock speed. In order to satisfy the jump conditions for a single right-propagating shock wave, it is required that the velocity of the left state depend on the density ρ_0 according to the Hugoniot locus relation [60] $u_0(\rho_0) = [5(\rho_0^{7/5} - 1)(\rho_0 - 1)/(7\rho_0)]^{1/2}$. The speed of the corresponding shock is then

$$V(\rho_0) = \{[5(\rho_0^{7/5} - 1)\rho_0]/[7(\rho_0 - 1)]\}^{1/2}. \quad (7.10)$$

The VSW speed is parameterized only by the left-state density ρ_0 and is independent of the magnitude of the viscous correction.

7.4.2 Dispersion

The dispersive regularization, $0 < \epsilon \ll 1$, of the initial jump (7.9) results in a DSW, two distinct constant states connected by an expanding, oscillatory region. This region is characterized by nearly linear, vanishing amplitude waves at the rightmost leading edge and a single (dark) solitary wave at the leftmost trailing edge (see Fig. 7.2). DSW closure conditions, analogous to the jump conditions for VSWs, provide relations between the left and right constant states and the edge speeds. To implement the DSW closure, we use Whitham-El DSW theory [24], an extension of the nonlinear wave modulation theory of Whitham [125] for dispersive shock-fitting [40] to nonintegrable systems such as the one considered here. For the theoretical details, we refer the reader to an extensive development of DSW theory for gNLS equations in [47].

DSW closure implies that the velocity u_0 must lie on the DSW locus $u_0(\rho_0) = 5(\rho_0^{1/5} - 1)$, which is distinct from the Hugoniot locus for VSWs. The speed v_L of the linear, leading edge satisfies

$$v_L = \frac{2\alpha_L^2 - 1}{\alpha_L}, \quad \frac{27(1 + \alpha_L)}{2(2 + \alpha_L)^3} = \rho_0^{-2/5}. \quad (7.11)$$

The speed v_S at the trailing, soliton edge is

$$v_S = [\alpha_S \rho_0^{1/5} + 5(\rho_0^{1/5} - 1)], \quad \frac{27(1 + \alpha_S)}{2(2 + \alpha_S)^3} = \rho_0^{2/5}. \quad (7.12)$$

While for classical shocks, eq. (7.10) gives an explicit speed in terms ρ_0 , eqs. (7.11), (7.12) give implicit relations. To compare them directly, we consider the small jump case $0 < \delta = (\rho_0 - 1) \ll 1$, in which the dispersively regularized conservation laws admit a weak DSW with speeds $v_L \sim 1 + 12\delta/5$, $v_S \sim 1 + 2\delta/5$. For the weak VSW from (7.10), $V \sim 1 + 3\delta/5$. This analysis demonstrates that regularization dependent shock speeds differ, even for small density perturbations. In Fig. 7.1, we plot the dispersive and viscous shock speeds for a range of density jumps. As noted earlier, not only the shock speed but also its structure changes drastically depending on the regularization mechanism, though under present imaging capabilities, the difference is not as clear. The left panel of Fig. 7.2 depicts the numerical solution to the

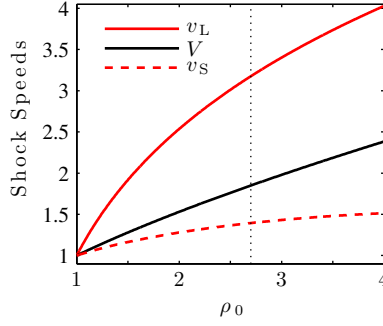


Figure 7.1: Nondimensional shock speeds by type of regularization. v_L and v_S correspond to the leading and trailing edge speeds of a UFG DSW, respectively. V is the dissipative shock speed. The vertical dotted line at $\rho_0 = 2.7$ is for comparison with the particular discontinuity simulated in figure 7.2.

gNLS equation corresponding to the hydrodynamic eqs. (7.5), (7.6) and shock solution for the dissipative hydrodynamics ($\epsilon = 0$). The signature slowly modulated, oscillatory envelope structure expected for a DSW is further revealed by the zoomed-in inset. The right panels of Fig. 7.2 depict the DSW and VSW solutions convolved with a Gaussian of width 1, the modulation length, mimicking the effects of imaging. Owing to the smoothing of the rapid DSW oscillations, the DSW is now more difficult to distinguish from the filtered VSW solution (dashed). However, DSW expansion is noticeable from the spreading of the steep density gradient. Conversely, the VSW maintains its shape and propagates with a different speed. This shows that determination of the speed of the shock front and its scaling according to (7.10) or (7.11),(7.12) is a viable experimental method for distinguishing between dispersive and dissipative shocks even when potential oscillations are sub-imaging resolution.

7.5 Regularization Determining Experiments

In deriving the shock solutions, we have assumed the validity of the one-dimensional reduction. In previous attempts to describe the UFG collision experimental observations, a regularization term has been added to a 1D or 3D hydrodynamic model [52, 5, 94]. From the experimental

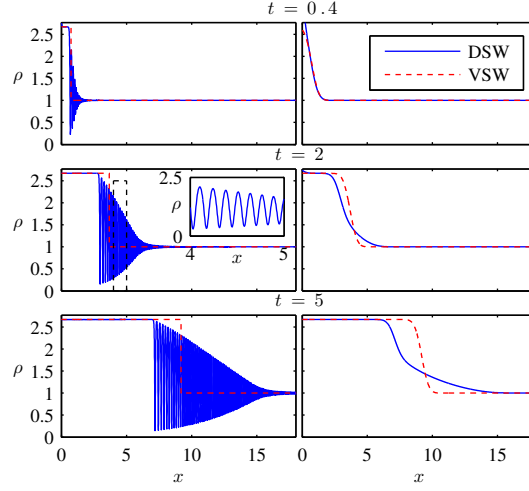


Figure 7.2: Numerical simulation of the gNLS equation (solid) (from eqs. (7.5), (7.6)) for a DSW with $\rho_0 = 2.7$ and corresponding VSW solution (dashed). The right panel depicts the filtered solutions.

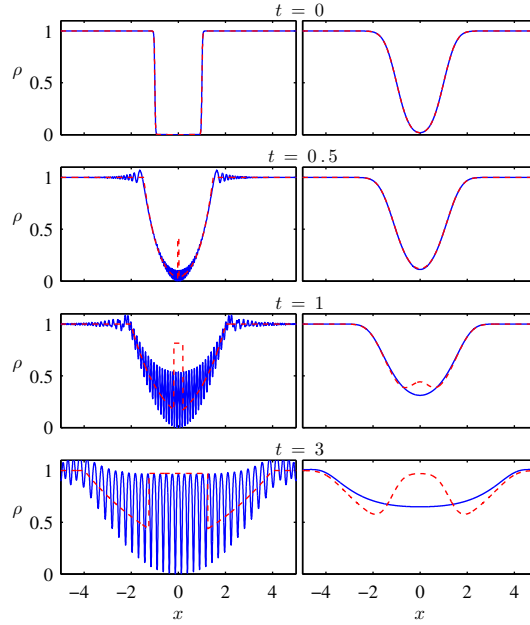


Figure 7.3: Numerical simulation of the gNLS equation (solid) and dissipative hydrodynamic equations (dashed) for the collision problem. The right panel depicts the filtered solutions.

parameters, it is verified that the anisotropy criterion for reduction to 1D is not met [52]. Further, from its similarity to observations in BEC [18], the appearance of a characteristic center “bulge” upon collision in the experiments of [52] suggests the presence of transverse instabilities and vortex formation, lending doubt to the accuracy of the azimuthally symmetric numerical simulations in [5]. The 1D regime, however, is not subject to these instabilities. Therefore, we consider the 1D collision problem with dissipative ($\epsilon = 0$) and dispersive ($0 < \epsilon \ll 1$) regularizations for the idealized initial condition

$$\rho(z, 0) = \begin{cases} 1, & |z| > L \\ 0, & |z| \leq L \end{cases}, \quad u(z, 0) = 0, \quad (7.13)$$

representing two initially separated, quiescent UFGs.

The results for $L = 1$ are depicted in Fig. 7.3. The left panel shows the numerical solution for gNLS and the solution for the corresponding dissipative problem, while the right panel shows the Gaussian filtered solutions. Initially, two rarefaction waves propagate inward, for which the two regularizations agree to leading order because the effects of dissipation and dispersion are negligible. Upon collision of the rarefaction waves, outward propagating shocks are created. In the case of the viscous problem, we derive the weak solution to the hydrodynamic equations (see Appendix for details). The dispersive shock solution is similar to that observed in BEC theoretical and experimental studies [49]. The key physical difference after filtering is the distinct center bulge created in the dissipative problem. The dispersive solution, on the other hand, forms a smooth, expanding well between the two constant states. Therefore, the one-dimensional collision problem provides a clear distinction between dissipative and dispersive regularizations.

7.6 Conclusions

The similarity between the bulge-producing dissipative collision problem and both the BEC [18] and UFG [52] experiments is striking. We know that BEC is regularized by dispersion,

yet a bulge is still produced. One possible interpretation is that the proliferation of quantized vortices and quantum turbulence in the fully 3D case yields an effective viscosity for the larger scale dynamics, even though the underlying model is dissipationless. Similarly, fully 3D experiments in a UFG may not provide a definitive determination of the underlying hydrodynamic regularization mechanism unless imaging resolution is significantly improved. Our work here provides unambiguous measures of dispersive/dissipative effects in a unitary Fermi gas from shock dynamics, enabling the determination of the dominant regularization mechanism.

Acknowledgements: We thank John Thomas, James Joseph, and Peter Engels for enlightening discussion. This work was supported by NSF Grant Nos. DGE-1252376 and DMS-1008973.

7.7 Appendix – 1D Reduction

The 3D wavefunction expression (3) was reduced to an effective 1D model by integrating over the transverse dynamics as described in [76]. In this appendix we present the details of this calculation, as well as the derivation of the characteristic length and time scales presented. We further derive the weak solution for the dissipative 1D collision problem. We assume that the anisotropy condition is satisfied.

Decompose the 3D complex wavefunction such that $\psi(\mathbf{r}, t) = \Psi(\mathbf{r}_\perp; n_1(z, t))\Phi(z, t)$, where $\mathbf{r} = (\mathbf{r}_\perp, z)$ and $n_1(z, t)$ is the local density function which satisfies the normalization condition

$$n_1(z, t) = N \int |\psi(\mathbf{r}, t)|^2 d\mathbf{r} . \quad (7.14)$$

Also assume the trap potential takes the special form $U(\mathbf{r}) = U_1(\mathbf{r}_\perp) + U_2(z)$ (above we consider the case of an ideal harmonic trap which certainly fits into this assumption). Normalize the transverse and longitudinal wave functions according to the constraints

$$\int |\Psi(\mathbf{r}_\perp; n_1)|^2 d\mathbf{r}_\perp = 1, \quad \int |\Phi(z, t)|^2 dz = N . \quad (7.15)$$

Hence, $n_1(z, t) = N |\Phi(z, t)|^2$. Substituting these anatzes into (3) yields

$$\left[i\hbar\lambda^{1/2}\frac{\partial\Phi}{\partial t} + \lambda\frac{\hbar^2}{2m}\frac{\partial^2\Phi}{\partial z^2} - U_2(z)\Phi \right] \Psi = \left[-\lambda\frac{\hbar^2}{2m}\Delta_r\Psi + U_1(\mathbf{r}_\perp)\Psi + \xi\mu_0 \left(|\Psi\Phi|^{4/3} \right) \Psi \right] \Phi . \quad (7.16)$$

Multiply the equation by the complex conjugate Ψ^* and integrate with respect to the transverse coordinates \mathbf{r}_\perp . Using the normalization condition on Ψ , gives

$$i\hbar\lambda^{1/2}\frac{\partial\Phi}{\partial t} + \lambda\frac{\hbar^2}{2m}\frac{\partial^2\Phi}{\partial z^2} - U_2(z)\Phi = \mu_\perp(n_1)\Phi, \quad (7.17)$$

where

$$\mu_\perp(n_1) = \int \Psi^* \left[-\lambda\frac{\hbar^2}{2m}\Delta_r + U_1(\mathbf{r}_\perp) + \xi\mu_0 \left(|\Psi\Phi|^{4/3} \right) \right] \Psi \, d\mathbf{r}_\perp . \quad (7.18)$$

This is now an effectively 1D equation, but it is left to determine μ_\perp and Ψ . If we substitute the expression for μ_\perp (7.18) into eq. (7.16) and enter the Thomas-Fermi regime (neglecting the radial Laplacian term), we get the following eigenvalue problem for Ψ :

$$U_1(\mathbf{r}_\perp)\Psi + \xi\mu_0 \left(|\Psi\Phi|^{4/3} \right) \Psi = \mu_\perp(n_1)\Psi . \quad (7.19)$$

Note that $|\Phi|^{4/3} = (n_1/N)^{2/3}$. Then solving for Ψ , we find

$$|\Psi|^{4/3} = \left(\frac{N}{n_1} \right)^{2/3} \frac{1}{\xi\mu_0} (\mu_\perp - U_1(\mathbf{r}_\perp)) . \quad (7.20)$$

Assuming that Ψ is real in the ground state, (7.20) can be solved explicitly to obtain

$$\Psi = \begin{cases} \left(\frac{N}{n_1} \right)^{1/2} [\xi\mu_0 (\mu_\perp - U_1(\mathbf{r}_\perp))]^{3/4}, & \mu_\perp > U_1(\mathbf{r}_\perp), \\ 0, & \text{otherwise} . \end{cases} \quad (7.21)$$

Next, an expression is needed for μ_\perp which comes from the normalization condition on the transverse wave function (7.15). Assume an ideal, harmonic trap potential so that $U_1(\mathbf{r}_\perp) =$

$\frac{1}{2}\omega_{\perp}^2 r_{\perp}^2$, where $r_{\perp}^2 = x^2 + y^2$. Note that Ψ vanishes for r_{\perp} such that $U_1(\mathbf{r}_{\perp}) \geq \mu_{\perp}$. This gives the upper bound of the integration in (7.14) to be

$$r_{\perp} < \left(\frac{2\mu_{\perp}}{m\omega_{\perp}} \right)^{1/2}. \quad (7.22)$$

Substituting eqs. (7.21) and (7.22) into eq. (7.15), one can solve for μ_{\perp} from

$$\int_0^{\left(\frac{2\mu_{\perp}}{m\omega_{\perp}}\right)^{1/2}} r_{\perp} \left(\mu_{\perp} - \frac{1}{2}\omega_{\perp}^2 r_{\perp}^2 \right)^{3/2} dr_{\perp} = \frac{(\xi\mu_0)^{3/2}}{2\pi} \left(\frac{n_1}{N} \right). \quad (7.23)$$

Eq. (7.23) can be integrated upon making a simple change of variables to obtain

$$\mu_{\perp} = \left(\frac{5m\omega_{\perp}^2 (\xi\mu_0)^{3/2}}{4\pi} \right)^{2/5} |\Phi|^{4/5}. \quad (7.24)$$

The trap potential in the longitudinal coordinate z is assumed to be $U_2(z) = \frac{1}{2}m\omega_z^2 z^2$. Hence, eq. (7.17) becomes

$$i\hbar\lambda^{1/2}\frac{\partial\Phi}{\partial t} + \lambda\frac{\hbar^2}{2m}\frac{\partial^2\Phi}{\partial z^2} - \frac{1}{2}m\omega_z^2 z^2\Phi - \left(\frac{5m\omega_{\perp}^2 (\xi\mu_0)^{3/2}}{4\pi} \right)^{2/5} |\Phi|^{4/5}\Phi = 0, \quad (7.25)$$

which is 1D and in dimensional form.

We now nondimensionalize the equation using $\Phi = \Phi_0\tilde{\Phi}$, $z = L\tilde{z}$, and $t = T\tilde{t}$ to the semiclassical scaling with normalized sound speed, which after dropping tildes becomes

$$i\epsilon\frac{\partial\Phi}{\partial t} + \frac{\epsilon^2}{2}\frac{\partial^2\Phi}{\partial z^2} - \frac{1}{2}\kappa z^2\Phi - \frac{5}{2}|\Phi|^{4/5}\Phi = 0. \quad (7.26)$$

Note that each term in (7.25) is dimensional. We multiply both sides by a dimensional parameter A and normalize (7.25) to the semiclassical scaling (7.26) while enforcing the normalization

condition (7.15). This yields the parameters and scalings

$$L = L_0, \quad \Phi_0 = \left(\frac{N}{L_0} \right)^{1/2}, \quad (7.27)$$

$$T = \left(\frac{10\sqrt{5}}{3\pi\xi^{3/2}N} \right)^{1/5} \left(\frac{1}{\omega_\perp} \right) \left(\frac{L_0}{a_\perp} \right)^{6/5} \quad (7.28)$$

$$\epsilon = \left(\frac{10\sqrt{5}\lambda^{5/2}}{3\pi\xi^{3/2}N} \right)^{1/5} \left(\frac{a_\perp}{L_0} \right)^{4/5}, \quad (7.29)$$

$$\kappa = \left(\frac{10\sqrt{5}}{3\pi\xi^{3/2}N} \right)^{2/5} \left(\frac{\omega_z}{\omega_\perp} \right)^2 \left(\frac{L_0}{a_\perp} \right)^{12/5}, \quad (7.30)$$

$$A = \left(\frac{10\sqrt{5}}{3\pi\xi^{3/2}N} \right)^{2/5} \left(\frac{1}{\hbar\omega_\perp} \right) \left(\frac{L_0}{a_\perp} \right)^{2/5}. \quad (7.31)$$

The inter-particle spacing L_{int} is estimated by determining the approximate volume occupied by N Fermions in the ground state of the harmonic trap. The standard Thomas-Fermi approximation is used whereby the kinetic energy terms are neglected in favor of a balance between the nonlinearity and the trap potential, $\mu(n) = \mu_0 - U(\mathbf{r})$ from eq. (2). μ_0 is the total chemical potential determined by the requirement that $\int n \, d\mathbf{r} = N$. The volume is

$$\begin{aligned} \text{Vol}\{\mathbf{r} \mid \mu_0 > U(\mathbf{r})\} &= \frac{2^{7/2}\xi^{3/4}\pi}{3^{1/2}} N^{1/2} a_\perp^2 a_z \\ &\approx 10.3 N^{1/2} a_\perp^2 a_z. \end{aligned} \quad (7.32)$$

Dividing the cube root of the volume by N gives

$$L_{\text{int}} = \left(\frac{2^{7/2}\xi^{3/4}\pi}{3^{1/2}} \right)^{1/3} \left(\frac{a_\perp^2 a_z}{N^{1/2}} \right)^{1/3} \approx 2.18 \left(\frac{a_\perp^2 a_z}{N^{1/2}} \right)^{1/3}. \quad (7.33)$$

The 1D collision problem with $\epsilon = 0$ and initial data given by (13) generates two rarefaction waves propagating inward from the initial discontinuities at $|z| = L$, which interact at time $t = t_i$. For comparison with numerical simulations, we set $L = 1$, though the results are easily

generalizable. On the right (the left can be constructed from symmetry), the rarefaction wave is given by

$$u(z, t) = \frac{5}{6} \left[\frac{z-1}{t} - 1 \right] , \quad (7.34)$$

$$\rho(z, t) = \left[\frac{1}{6} \left(5 + \frac{z-1}{t} \right) \right]^5 , \quad (7.35)$$

for $(z-1)/t \in [-5, 1]$. Hence, $t_i = 1/5$. Immediately upon interaction, an intermediate velocity state $u_m = 0$ is created along the center axis $z = 0$ and two outward propagating shocks are produced. These can be described by constructing an intermediate density ρ_m so that it lies along the appropriate density locus, i.e.

$$u^2 = \frac{5 \left(\rho_m^{7/5} - \rho^{7/5} \right) (\rho_m - \rho)}{7 \rho_m \rho} , \quad (7.36)$$

where u and ρ are evaluated at the right rarefaction waves just ahead of the shock front, which are the variable background into which the shock is propagating. The intermediate value ρ_m , which must be found by evaluating (7.36) implicitly, couples to the shock speed by invoking the jump conditions to give the ordinary differential equation

$$s'(t) = \left. \frac{\rho u}{\rho - \rho_m} \right|_{z=s(t)} . \quad (7.37)$$

The initial condition must be prescribed just after the interaction time so that a shock is created, say $t = t_i + \nu$, $0 < \nu \ll 1$. Then, inserting the Taylor series expansion, $s(1/5) = 0 \sim s(1/5 + \nu) - \nu s'(1/5 + \nu)$ into (7.36), (7.37) gives the approximate initial data

$$s(1/5 + \nu) \sim \nu^{17/7} \frac{5^{17/7}}{35^{5/7} - 1}, \quad 0 < \nu \ll 1 , \quad (7.38)$$

which we use as initial conditions to numerically solve the system (7.36), (7.37). For the simulations presented, we took $\nu = 5 \times 10^{-5}$ and found it to be sufficiently small to accurately resolve the shock dynamics.

Chapter 8

Conclusion

The key result of this work is the establishment of the viscous fluid conduit setting as an ideal platform for the comprehensive study of unidirectional nonlinear dispersive wave phenomena in one dimension. Starting from the full system of mass and momentum conservation equations describing the dynamics of two fluids separated by a free interface, we have shown that the leading order dynamics can be described in terms of only a scalar PDE for the cross-sectional area of the conduit formed by the interior fluid. That a dissipationless model equation can be derived at all for a highly viscous system is remarkable in itself, but we find that this model is valid for long times and large amplitudes provided only modest assumptions hold for the two fluids.

A combined numerical and analytical approach, using Whitham-El modulation theory, to the analysis of the conduit equation and its generalization yielded theoretical predictions for key physical properties of conduit DSWs and large amplitude solitary wave interactions. Moreover, the identification of new shock phenomena in the conduit system led us to identify four new admissibility criteria for the validity of the simple wave DSW closure method. It was also demonstrated for a quantum mechanical system that the theory of dispersive hydrodynamics can inform the design of new experiments to resolve questions of physically modeling a system.

The theoretical and numerical predictions for wave propagation along the conduit interface

were then compared with laboratory simulations of the full two-fluid system in the in-house NC State Dispersive Shock Wave Laboratory. Experiments on large amplitude solitary wave interactions yielded remarkable agreement with analysis of the conduit equation and also demonstrated a persistence of soliton interaction properties predicted by weakly nonlinear, integrable systems theory, even into the large amplitude regime. Initial investigations into shock wave experiments yield good agreement with analytical theory and merit further investigation.

The work in this thesis has also opened several new and interesting directions for future research, both pertaining to the conduit setting and to dispersive hydrodynamic systems, in general. The establishment of the DSW laboratory and the robustness of nonlinear wave phenomena in the conduit system offer possibilities to validate several longstanding nonlinear wave theories and make interesting new observations. Some of these are soliton-rarefaction, DSW-DSW, DSW-soliton, and DSW-rarefaction interactions, the amplitude distribution and number of solitons emanating from localized initial data, and the statistical properties pertaining to the passage into the soliton turbulence limit. Physically, one can also examine the effects of the introduction of new physical perturbations, such as a physical dissipation via a non-Newtonian exterior fluid, the stability of wave structures in the presence on an inhomogeneous medium, or the breaking of the conduit's azimuthal symmetry. Unrelated to conduits, this study has also opened new directions for DSW modulation theory, namely we have identified the need for an extension of the theoretical methods beyond the simple wave regime, and it also remains to be explored whether DSW implosion in the modulation equations can be realized experimentally and, theoretically in the shock interior, rather than from its edges. These open problems demonstrate the richness of the underlying mathematics and fluid mechanics considered in this thesis.

REFERENCES

- [1] M. J. ABLOWITZ AND D. E. BALDWIN, *Interactions and asymptotics of dispersive shock waves Korteweg–de Vries equation*, Phys. Lett. A, 377 (2013), p. 555.
- [2] M. J. ABLOWITZ, D. E. BALDWIN, AND M. A. HOEFER, *Soliton generation and multiple phases in dispersive shock and rarefaction wave interaction*, Phys. Rev. E, 80 (2009), p. 016603.
- [3] M. J. ABLOWITZ AND T. S. HAUT, *Asymptotic expansions for solitary gravity-capillary waves in two and three dimensions*, J. Phys. A, 43 (2010), p. 434005.
- [4] A. AMO, S. PIGEON, D. SANVITTO, V. G. SALA, R. HIVET, I. CARUSOTTO, F. PISANELLO, G. LEMNAGER, R. HOUDR, E. GIACOBINO, C. CIUTI, AND A. BRAMATI, *Polariton superfluids reveal quantum hydrodynamic solitons*, Science, 332 (2011), p. 1167.
- [5] F. ANCILOTTO, L. SALASNICH, AND F. TOIGO, *Shock waves in strongly interacting fermi gas from time-dependent density functional calculations*, Phys. Rev. A, 85 (2012), p. 063612.
- [6] V. BARCILON AND O. M. LOVERA, *Solitary waves in magma dynamics*, J. Fluid Mech., 204 (1989), p. 121.
- [7] V. BARCILON AND F. M. RICHTER, *Nonlinear waves in compacting media*, J. Fluid Mech., 164 (1986), p. 429.
- [8] C. BARSÌ, W. WAN, C. SUN, AND J. W. FLEISCHER, *Dispersive shock waves with nonlocal nonlinearity*, Opt. Lett., 32 (2007), p. 2930.
- [9] G. K. BATCHELOR, *An Introduction to Fluid Dynamics*, Cambridge University Press, 1967.
- [10] T. B. BENJAMIN, *Internal waves of permanent form in fluids of great depth*, J. Fluid Mech., 29 (1967), p. 559.
- [11] E. BETTELHEIM AND L. GLAZMAN, *Quantum ripples over a semiclassical shock*, Phys. Rev. Lett., 109 (2012), p. 260602.
- [12] I. BLOCH, J. DALIBARD, AND W. ZWERGER, *Many-body physics with ultracold gases*, Rev. Mod. Phys., 80 (2008), p. 885.
- [13] J. L. BONA, W. G. PRITCHARD, AND L. R. SCOTT, *Solitarywave interaction*, Phys. Fluids, 23 (1980), p. 438.
- [14] A. BULGAC, Y.-L. LUO, AND K. ROCHE, *Quantum shock waves and domain walls in the real-time dynamics of a superfluid unitary fermi gas*, Phys. Rev. Lett., 108 (2012), p. 150401.

- [15] S. BURGER, K. BONGS, S. DETTMER, W. ERTMER, K. SENGSTOCK, A. SANPERA, G. V. SHLYAPNIKOV, AND M. LEWENSTEIN, *Dark solitons in bose-einstein condensates*, Phys. Rev. Lett., 83 (1999), p. 053017.
- [16] C. CAO, E. ELLIOTT, H. WU, AND J. E. THOMAS, *Searching for perfect fluids: quantum viscosity in a universal fermi gas*, New J. Phys., 13 (2011), p. 075007.
- [17] J. CARLSON, S. GANDOLFI, K. E. SCHMIDT, AND S. ZHANG, *Auxiliary-field quantum monte carlo method for strongly paired fermions*, Phys. Rev. A, 84 (2011), p. 061602.
- [18] J. CHANG, P. ENGELS, AND M. HOEFER, *Formation of dispersive shock waves by merging and splitting bose-einstein condensates*, Phys. Rev. Lett., 101 (2008), p. 170404.
- [19] H. CHANSON, *Tidal Bores, Aegir, Eagre, Mascaret, Pororoca: Theory and Observations*, World Scientific, Singapore, 2011.
- [20] C. CONTI, A. FRATALOCCHI, M. PECCANTI, G. RUOCCO, AND S. TRILLO, *Observation of a gradient catastrophe generating solitons*, Phys. Rev. Lett., 102 (2009), p. 083902.
- [21] W. CRAIG, P. GUYENNE, J. HAMMACK, D. HENDERSON, AND C. SULEM, *Solitary water wave interactions*, Physics of Fluids, 18 (2006), p. 057106.
- [22] C. M. DAFERMOS, *Hyperbolic conservation laws in continuum physics*, Springer, Heidelberg, 2000.
- [23] Z. DUTTON, M. BUDDE, C. SLOWE, AND L. HAU, *Observation of quantum shock waves created with ultra- compressed slow light pulses in a bose-einstein condensate*, Science, 293 (2001), p. 663.
- [24] G. A. EL, *Resolution of a shock in hyperbolic systems modified by weak dispersion*, Chaos, 15 (2005), p. 037103.
- [25] G. A. EL, R. H. J. GRIMSHAW, AND N. F. SMYTH, *Unsteady undular bores in fully nonlinear shallow-water theory*, Phys. Fluids, 18 (2006), p. 027104.
- [26] ———, *Transcritical shallow-water flow past topography: finite-amplitude theory*, J. Fluid Mech., 640 (2009), p. 187.
- [27] G. A. EL AND A. M. KAMCHATNOV, *Kinetic equation for a dense soliton gas*, Phys. Rev. Lett., 95 (2005), p. 204101.
- [28] T. ELPERIN, N. KLEEORIN, AND A. KRYLOV, *Nondissipative shock waves in two-phase flows*, Physica D, 74 (1994), p. 372.
- [29] J. G. ESLER AND J. D. PEARCE, *Dispersive dam-break and lock-exchange flows in a two-layer fluid*, J. Fluid Mech., 667 (2011), p. 555.
- [30] H. FLASCHKA, M. G. FOREST, AND D. W. MCLAUGHLIN, *Multiphase averaging and the inverse spectral solution of the kortewegde vries equation*, Comm. Pur. Appl. Math., 33 (1980), p. 739.

- [31] M. M. FORBES, S. GANDOLFI, AND A. GEZERLIS, *Resonantly interacting fermions in a box*, Phys. Rev. Lett., 106 (2011), p. 235303.
- [32] M. G. FOREST AND J. E. LEE, *Geometry and modulation theory for the periodic nonlinear Schrödinger equation in Oscillation theory, computation and methods of compensated compactness*, Springer, New York, 1986.
- [33] A. C. FOWLER, *A mathematical model of magma transport in the asthenosphere*, Geophys. Asto. Fluid., 33 (1985), p. 63.
- [34] N. GHOFRAHI, L. S. AMATO, V. FOLLI, S. TRILLO, E. DELRE, AND C. CONTI, *Measurement of scaling laws for shock waves in thermal nonlocal media*, Optics Letters, 37 (2012), p. 2325.
- [35] N. GHOFRAHI, C. CONTI, G. RUOCCO, AND S. TRILLO, *Shocks in nonlocal media*, Phys. Rev. Lett., 99 (2007), p. 043903.
- [36] S. GIORGINI AND S. STRINGARI, *Theory of ultracold atomic fermi gases*, Rev. Mod. Phys., 80 (2008), p. 1215.
- [37] T. GRAVA AND F.-R. TIAN, *The generation, propagation, and extinction of multiphases in the KdV zero-dispersion limit*, Comm. Pur. Appl. Math., 55 (2002), p. 1569.
- [38] A. E. GREEN AND P. M. NAGHDI, *A derivation of equations for wave propagation in water of variable depth*, J. Fluid Mech., 78 (1976), p. 237.
- [39] R. H. J. GRIMSHAW, K. R. HELFRICH, AND J. A. WHITEHEAD, *Conduit solitary waves in a visco-elastic medium*, Geophys. Asto. Fluid., 65 (1992), p. 127.
- [40] A. V. GUREVICH AND L. P. PITAEVSKII, *Nonstationary structure of a collisionless shock wave*, Sov. Phys. JETP, 33 (1974), p. 291.
- [41] S. E. HARRIS, *Conservation laws for a nonlinear wave equation*, Nonlinearity, 9 (1996), p. 187.
- [42] —, *Painlevé analysis and similarity reductions for the magma equation*, SIGMA, 2 (2006), p. 68.
- [43] K. R. HELFRICH AND J. A. WHITEHEAD, *Solitary waves on conduits of buoyant fluid in a more viscous fluid*, Geophys. Asto. Fluid., 51 (1990), p. 35.
- [44] R. HIROTA, *Exact solution of the korteweg-de vries equation for multiple collisions of solitons*, Phys. Rev. Lett., 27 (1971), p. 1192.
- [45] M. HOEFER AND M. ABLOWITZ, *Dispersive shock waves*, Scholarpedia, 4 (2009), p. 5562.
- [46] M. HOEFER, M. ABLOWITZ, I. CODDINGTON, E. CORNELL, P. ENGELS, AND V. SCHWEIKHARD, *Dispersive and classical shock waves in bose-einstein condensates and gas dynamics*, Phys. Rev. A, 74 (2006), p. 023623.

- [47] M. A. HOEFER, *Shock waves in dispersive Eulerian fluids*, J. Nonlinear Sci., published online (2014).
- [48] M. A. HOEFER AND M. J. ABLOWITZ, *Interactions of dispersive shock waves*, Physica D, 236 (2007), p. 44.
- [49] M. A. HOEFER, P. ENGELS, AND J. J. CHANG, *Matterwave interference in BoseEinstein condensates: A dispersive hydrodynamic perspective*, Physica D, 238 (2009), p. 1311.
- [50] S. JIA, W. WAN, AND J. W. FLEISCHER, *Dispersive shock waves in nonlinear arrays*, Phys. Rev. Lett., 99 (2007), pp. 223901–4.
- [51] M. C. JORGE, A. A. MINZONI, AND N. F. SMYTH, *Modulation solutions for the Benjamin-Ono equation*, Physica D, 132 (1999), p. 1.
- [52] J. JOSEPH, J. THOMAS, M. KULKARNI, AND A. ABANOV, *Observation of shock waves in a strongly interacting fermi gas*, Phys. Rev. Lett., 106 (2011), p. 150401.
- [53] A. M. KAMCHATNOV, Y.-H. KUO, T.-C. LIN, T.-L. HORNG, S.-C. GOU, R. CLIFT, G. A. EL, AND R. H. J. GRIMSHAW, *Undular bore theory for the gardner equation*, Phys. Rev. E, 86 (2012), p. 036605.
- [54] R. F. KATZ, M. KNEPLEY, B. SMITH, M. SPIEGELMAN, AND E. COON, *Numerical simulation of geodynamic processes with the portable extensible toolkit for scientific computation*, Phys. Earth Planet In., 163 (2007), p. 52.
- [55] P. G. KEVREKIDIS, D. J. FRANTZESKAKIS, AND R. CARRETERO-GONZALEZ, *Emergent Nonlinear Phenomena in Bose-Einstein Condensates*, Springer, 2008.
- [56] Y. KODAMA, V. U. PIERCE, AND F.-R. TIAN, *On the whitham equations for the defocusing complex modified KdV equation*, SIAM J. Math. Anal., 40 (2009), p. 1750.
- [57] D. J. KORTEWEG AND G. DE VRIES, *On the change of form of long waves advancing in a rectangular canal, and on a new type of long stationary waves*, Philos. Mag. Ser. 5, 39 (1895), p. 422.
- [58] M. KULKARNI AND A. ABANOV, *Hydrodynamics of cold atomic gases in the limit of weak nonlinearity, dispersion, and dissipation*, Phys. Rev. A, 86 (2012), p. 033614.
- [59] P. D. LAX, *Integrals of nonlinear equations of evolution and solitary waves*, Comm. Pur. Appl. Math., 21 (1968), p. 467.
- [60] —, *Hyperbolic Systems of Conservation Laws and the Mathematical Theory of Shock Waves*, SIAM, 1973.
- [61] P. D. LAX AND C. D. LEVERMORE, *The small dispersion limit of the korteweg-de vries equation. i*, Comm. Pur. Appl. Math., 36 (1983), p. 253.
- [62] —, *The small dispersion limit of the korteweg-de vries equation. II*, Comm. Pur. Appl. Math., 36 (1983), p. 571.

- [63] ———, *The small dispersion limit of the korteweg-de vries equation. III*, Comm. Pur. Appl. Math., 36 (1983), p. 809.
- [64] R. LEVEQUE, *Finite Volume Methods for Hyperbolic Problems*, Cambridge University Press, Cambridge, UK, 2002.
- [65] W. LI, *Amplification of solitary waves along a vertical wall*, Ph.D., Oregon State University, 2012. Graduation date: 2013.
- [66] M. J. LIDTHILL, *Contributions to the theory of waves in non-linear dispersive systems*, IMA J. Appl. Math., 1 (1965), p. 269.
- [67] Y. LIU, H. TU, AND S. A. BOPPART, *Wave-breaking-extended fiber supercontinuum generation for high compression ratio transform-limited pulse compression*, Optics Letters, 37 (2012), p. 2172.
- [68] N. K. LOWMAN AND M. A. HOEFER, *Dispersive hydrodynamics in viscous fluid conduits*, Phys. Rev. E, 88 (2013), p. 023016.
- [69] ———, *Dispersive shock waves in viscously deformable media*, J. Fluid Mech., 718 (2013), p. 524.
- [70] ———, *Fermionic shock waves: Distinguishing dissipative versus dispersive regularizations*, Phys. Rev. A, 88 (2013), p. 013605.
- [71] N. K. LOWMAN, M. A. HOEFER, AND G. A. EL, *Interactions of large amplitude solitary waves in viscous fluid conduits*, arXiv:1312.0647 [nlin.PS], (2013).
- [72] K. W. MADISON, F. CHEVY, W. WOHLLEBEN, AND J. DALIBARD, *Vortex formation in a stirred bose-einstein condensate*, Phys. Rev. Lett., 84 (2000), p. 806.
- [73] T. R. MARCHANT AND N. F. SMYTH, *Approximate solutions for magmon propagation from a reservoir*, IMA J. Appl. Math., 70 (2005), p. 796.
- [74] M. R. MATTHEWS, B. P. ANDERSON, P. C. HALJAN, D. S. HALL, C. E. WIEMAN, AND E. A. CORNELL, *Vortices in a bose-einstein condensate*, Phys. Rev. Lett., 83 (1999), p. 2498.
- [75] D. MCKENZIE, *The generation and compaction of partially molten rock*, J. Petrol., 25 (1984), p. 713.
- [76] C. MENOTTI AND S. STRINGARI, *Collective oscillations of a one-dimensional trapped bose-einstein gas*, Phys. Rev. A, 66 (2002), p. 043610.
- [77] R. MEPPPELINK, S. KOLLER, J. VOGELS, P. VAN DER STRATEN, E. VAN OOIJEN, N. HECKENBERG, H. RUBINSZTEIN-DUNLOP, S. HAINE, AND M. DAVIS, *Observation of shock waves in a large bose-einstein condensate*, Phys. Rev. A, 80 (2009), p. 043606.
- [78] J. W. MILES, *Obliquely interacting solitary waves*, J. Fluid Mech., 79 (1977), p. 157.

- [79] R. M. MIRIE AND C. H. SU, *Collisions between two solitary waves. part 2. a numerical study*, J. Fluid Mech., 115 (1982), p. 475.
- [80] Y. MO, *Experimental observations of soliton wave trains in electron beams*, Phys. Rev. Lett., 110 (2013).
- [81] H. MORITZ, T. STFERLE, K. GNTER, M. KHL, AND T. ESSLINGER, *Confinement induced molecules in a 1D fermi gas*, Phys. Rev. Lett., 94 (2005), p. 210401.
- [82] M. NAKAYAMA AND D. P. MASON, *Rarefactive solitary waves in two-phase fluid flow of compacting media*, Wave Motion, 15 (1992), p. 357.
- [83] P. OLSON AND U. CHRISTENSEN, *Solitary wave propagation in a fluid conduit within a viscous matrix*, J. Geophys. Res., 91 (1986), p. 6367.
- [84] H. ONO, *Algebraic solitary waves in stratified fluids*, J. Phys. Soc. Jpn., 39 (1975), p. 1082.
- [85] L. A. OSTROVSKY AND A. I. POTAPOV, *Modulated Waves: Theory and Applications*, Johns Hopkins University Press, 2002.
- [86] L. E. PAYNE AND W. H. PELL, *The stokes flow problem for a class of axially symmetric bodies*, J. Fluid Mech., 7 (1960), p. 529.
- [87] E. N. PELINOVSKY, E. G. SHURGALINA, A. V. SERGEEVA, T. G. TALIPOVA, G. A. EL, AND R. H. J. GRIMSHAW, *Two-soliton interaction as an elementary act of soliton turbulence in integrable systems*, Phys. Lett. A, 377 (2013), p. 272.
- [88] V. U. PIERCE AND F.-R. TIAN, *Self-similar solutions of the non-strictly hyperbolic whitham equations*, Dyn. PDE, 4 (2007), p. 263.
- [89] A. PORTER AND N. F. SMYTH, *Modelling the morning glory of the gulf of carpentaria*, J. Fluid Mech., 454 (2002), p. 1.
- [90] I. V. PROTOPOPOV, D. B. GUTMAN, P. SCHMITTECKERT, AND A. D. MIRLIN, *Dynamics of waves in one-dimensional electron systems: Density oscillations driven by population inversion*, Phys. Rev. B, 87 (2013), p. 045112.
- [91] F. M. RICHTER AND D. MCKENZIE, *Dynamical models for melt segregation from a deformable matrix*, J. Geol., 92 (1984), p. 729.
- [92] E. ROLLEY, C. GUTHMANN, AND M. S. PETTERSEN, *The hydraulic jump and ripples in liquid helium*, Physica B: Condensed Matter, 394 (2007), p. 46.
- [93] J. E. ROTHENBERG AND D. GRISCHKOWSKY, *Observation of the formation of an optical intensity shock and wave breaking in the nonlinear propagation of pulses in optical fibers*, Phys. Rev. Lett., 62 (1989), p. 531.
- [94] L. SALASNICH, *Supersonic and subsonic shock waves in the unitary fermi gas*, Europhys. Lett., 96 (2011), p. 40007.

- [95] L. SALASNICH AND F. TOIGO, *Extended thomas-fermi density functional for the unitary fermi gas*, Phys. Rev. A, 78 (2008), p. 053626.
- [96] A. E. SCHEIDEGGER, *The physics of flow through porous media*, University of Toronto Press, Toronto, 1974.
- [97] D. R. SCOTT AND D. J. STEVENSON, *Magma solitons*, Geophys. Res. Lett., 11 (1984), p. 1161.
- [98] —, *Magma ascent by porous flow*, Geophys. Res. Lett., 91 (1986), p. 9283.
- [99] D. R. SCOTT, D. J. STEVENSON, AND J. A. WHITEHEAD, *Observations of solitary waves in a viscously deformable pipe*, Nature, 319 (1986), p. 759.
- [100] A. SCOTTI, R. C. BEARDSLEY, AND B. BUTMAN, *Generation and propagation of nonlinear internal waves in massachusetts bay*, J. Geophys. Res., 112 (2007).
- [101] F. SERRE, *Contribution á l'étude des écoulements permanents et variables dans les canaux*, Houille Blanche, 8 (1953), p. 374.
- [102] G. SIMPSON AND M. SPIEGELMAN, *Solitary wave benchmarks in magma dynamics*, J. Sci. Comput., 49 (2011), p. 268.
- [103] G. SIMPSON, M. SPIEGELMAN, AND M. I. WEINSTEIN, *Degenerate dispersive equations arising in the study of magma dynamics*, Nonlinearity, 20 (2007), p. 21.
- [104] —, *A multiscale model of partial melts 1: Effective equations*, J. Geophys. Res.-Solid, 115 (2010), p. B04410.
- [105] G. SIMPSON AND M. I. WEINSTEIN, *Asymptotic stability of ascending solitary magma waves*, SIAM J. Math. Anal., 40 (2008), p. 1337.
- [106] T. P. SIMULA, P. ENGELS, I. CODDINGTON, V. SCHWEIKHARD, E. A. CORNELL, AND R. J. BALLAGH, *Observations on sound propagation in rapidly rotating bose-einstein condensates*, Phys. Rev. Lett., 94 (2005), p. 080404.
- [107] N. F. SMYTH AND P. E. HOLLOWAY, *Hydraulic jump and undular bore formation on a shelf break*, J. Phys. Oceanogr., 18 (1988), p. 947.
- [108] M. SPIEGELMAN, *Flow in deformable porous media I. Simple analysis*, J. Fluid Mech., 247 (1993), p. 17.
- [109] —, *Flow in deformable porous media II. Numerical analysis*, J. Fluid Mech., 247 (1993), p. 39.
- [110] M. SPIEGELMAN, P. B. KELEMEN, AND E. AHARONOV, *Causes and consequences of flow organization during melt transport: The reaction infiltration instability in compatible media*, J. Geophys. Res., 106 (2001), p. 2061.

- [111] K. E. STRECKER, G. B. PARTRIDGE, A. G. TRUSCOTT, AND R. G. HULET, *Formation and propagation of matter-wave soliton trains*, Nature, 417 (2002), p. 150.
- [112] C. H. SU AND C. S. GARDNER, *Korteweg de Vries equation and generalizations. III. derivation of the Korteweg de Vries equation and Burgers equation*, J. Math. Phys., 10 (1969), p. 536.
- [113] D. TAKAHASHI, J. R. SACHS, AND J. SATSUMA, *Properties of the magma and modified magma equations*, J. Phys. Soc. Jpn., 59 (1990), p. 1941.
- [114] M. TANAKA, *The stability of solitary waves*, Phys. Fluids, 29 (1986), p. 650.
- [115] R. J. TAYLOR, D. R. BAKER, AND H. IKEZI, *Observation of collisionless electrostatic shocks*, Phys. Rev. Lett., 24 (1970), p. 206.
- [116] M. Q. TRAN, K. APPERT, C. HOLLENSTEIN, R. W. MEANS, AND J. VACLAVIK, *Shocklike solutions of the Korteweg-de Vries equation*, Plasma Physics, 19 (1977), p. 381.
- [117] S. VENAKIDES, *The zero dispersion limit of the Korteweg-de Vries equation for initial potentials with non-trivial reflection coefficient*, Commun. Pur. Appl. Anal., 38 (1985), p. 125.
- [118] C. F. VON WEIZSACKER, *Zue theorie der kernmassen*, Z. Phys., 96 (1935), p. 431.
- [119] W. WAN, S. JIA, AND J. W. FLEISCHER, *Dispersive superfluid-like shock waves in nonlinear optics*, Nat. Phys., 3 (2007), p. 46.
- [120] P. D. WEIDMAN AND T. MAXWORTHY, *Experiments on strong interactions between solitary waves*, Journal of Fluid Mechanics, 85 (1978), p. 417.
- [121] J. A. WHITEHEAD, *Instabilities of fluid conduits in a flowing earth are plates lubricated by the asthenosphere?*, Geophys. J. Roy. Astr. S, 70 (1982), p. 415.
- [122] J. A. WHITEHEAD AND K. R. HELFRICH, *The korteweg-deVries equation from laboratory conduit and magma migration equations*, Geophys. Res. Lett., 13 (1986), p. 545.
- [123] ———, *Magma waves and diapiric dynamics*, in Magma Transport and Storage, M. P. Ryan, ed., John Wiley & Sons, Chichester, 1990, pp. 53–76.
- [124] J. A. WHITEHEAD AND D. S. LUTHER, *Dynamics of laboratory diapir and plume models*, J. Geophys. Res., 80 (1975), p. 705.
- [125] G. B. WHITHAM, *Non-linear dispersive waves*, Proc. Roy. Soc. Ser. A, 283 (1965), p. 238.
- [126] ———, *Linear and nonlinear waves*, John Wiley & Sons, New York, 1974. Pure and Applied Mathematics.
- [127] T. YEFSAH, A. T. SOMMER, M. J. H. KU, L. W. CHEUK, W. JI, W. S. BAKR, AND M. W. ZWIERLEIN, *Heavy solitons in a fermionic superfluid*, Nature, 499 (2013), p. 426.

- [128] N. J. ZABUSKY AND M. D. KRUSKAL, *Interaction of “Solitons” in a collisionless plasma and the recurrence of initial states*, Phys. Rev. Lett., 15 (1965), p. 240.
- [129] M. W. ZWIERLEIN, J. R. ABO-SHAER, A. SCHIROTZEK, C. H. SCHUNCK, AND W. KETTERLE, *Vortices and superfluidity in a strongly interacting fermi gas*, Nature, 435 (2005), p. 1047.